Technical Physics Letters, Vol. 29, No. 7, 2003, pp. 529–532. Translated from Pis'ma v Zhurnal Tekhnicheskoĭ Fiziki, Vol. 29, No. 13, 2003, pp. 1–9.

Field Evaporation of Carbidized Tungsten

M. V. Loginov and V. N. Shrednik

Ioffe Physicotechnical Institute, Russian Academy of Sciences, St. Petersburg, 194021 Russia

Received January 27, 2003

Abstract—The field evaporation of carbidized tungsten (ribbed crystals) was studied by the atom probe method at various temperatures of the sample in the regions of cryogenic, room, and elevated (1300–1600 K) temperatures. For a high pulsed (not less than 40%) component in the evaporating field, the room-temperature field evaporation mass spectra correctly reflect the surface composition of the evaporated sample. The mass spectra reveal a large number of molecular and polymerized (cluster) ions. Data from field ion desorption microscopy indicate that high-temperature field evaporation of a ribbed crystal proceeds via ion emission from walking and merging thermal-field microroughnesses. *© 2003 MAIK "Nauka/Interperiodica".*

The deposition of carbon onto a tungsten point [1] and various stages of the interaction of hydrocarbons with such a point [2] are accompanied by the formation of a characteristic crystal structure at the point tip (Fig. 1). This structure, while retaining the symmetry and orientation of the tungsten substrate, is characterized (in contrast to a rounded shape typical of a pure tungsten point) by a pronounced faceting, featuring sharp ribs between developed crystal faces. This crystalline form is sometimes referred to as a ribbed crystal and we will use this term for brevity.

Investigation of the field evaporation of a ribbed crystal is of interest for two reasons. First, the ion fluxes observed in the course of room-temperature field evaporation exhibit nontrivial composition, containing molecular ions rather than atomic ions of tungsten and carbon [3]. In most cases, these ions do not correspond to the well-known tungsten carbides WC and W_2C [4]. Second, it is also of interest to trace variation of the chemical composition of a carbidized tungsten layer, from the uppermost surface layer to the pure tungsten bulk. Both these aspects have been preliminarily considered in [3].

This study was aimed at a thorough analysis of the ion flux composition during the field evaporation of a ribbed crystal, along with precise determination of the surface composition. The field evaporation was performed (as in [3]) in a time-of-flight atom probe system [5, 6]. From the standpoint of unambiguous surface analysis, it was important to ensure that field evaporation did not take place at a base applied voltage V_b and that all ions reaching a detector were formed only under the action of a sum of the base and pulsed ($V_b + V_p$) voltage components.

The first natural measure aimed at ensuring a zero evaporation at V_b was deep cooling of the sample. For this purpose, a rod with feedthroughs holding the sample point in the vacuum chamber was filled with liquid nitrogen. The tip temperature T could be 10–20 K above liquid nitrogen temperature, but it was sufficiently low to provide that the field evaporation at V_b could be ignored.

Ribbed crystals were grown *in situ*, by heating a tungsten tip in vacuum containing residual hydrocarbons from an oil diffusion pump of the TsVL-100 type.

Figure 2 shows typical field evaporation mass spectra measured at room and cryogenic temperatures. In both cases, the ribbed crystals were grown using the same standard procedure: heating at T = 1740 K for 2 min at an applied positive potential of 2 kV (preventing the tip point from rounding). This treatment was preceded by other experiments on the field evaporation from a tungsten point tip. The standard thermal treatment led to leveling of the carbon concentration on the

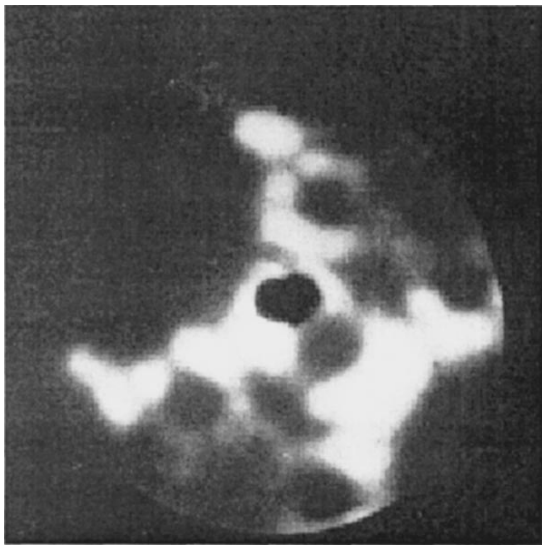

Fig. 1. A typical field electron image of a ribbed crystal oriented in the [011] direction (a dark circle on the left is the probing hole).

1063-7850/03/2907-0529$24.00

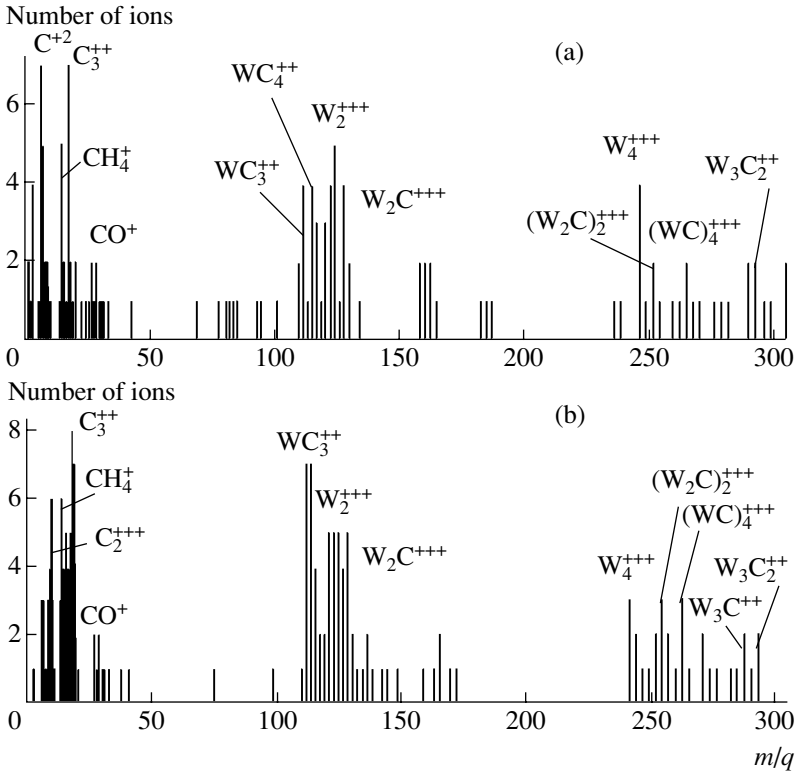

Fig. 2. Typical field evaporation mass spectrum of a ribbed crystal measured at an applied voltage of $V_b + V_p = 8$ kV + 5.6 kV (a) at room temperature ($n/N = 104/1246$) and (b) with the sample holder cooled by liquid nitrogen ($n/N = 111/2179$).

side surface and ensured the formation of a ribbed crystal presented in Fig. 1. The field evaporation (performed at the same values of $V_b + V_p = 8$ kV + 5.6 kV with almost the same number of informative pulses, $n = 104$ and 111) gives rise to a "negative" electron emission pattern [3, 7], which evidenced the removal of more than a monoatomic layer from the sample surface. The ion accumulation curves (integral curves) for both spectra in Fig. 2 included about 2–2.5 waves, which corresponded to evaporation of the same number of monolayers or about 200 ions.[1] The spectrum presented in Fig. 2b was measured immediately after that in Fig. 2a (naturally, after restoring the ribbed crystal by means of the standard thermal-field treatment), without readjustment of the probing hole (adjusted to the region of a crystal step at the edge of a {100} face). The spectra in Fig. 2 are constructed in the same scale on both axes.

A comparison of the mass spectra presented in Figs. 2a and 2b reveals no significant distinctions. The spectra display virtually the same set of ions, with peak heights varying within statistical error limits. Similar experiments, with the pairs of mass spectra recorded at room temperature and a cryogenic temperature for the same parameters V_b, V_p, and n were multiply repeated and the comparison always confirmed the similarity of the pattern observed. In all such experiments, the fraction of the pulsed voltage component $\omega = V_p/(V_b + V_p)$ amounted to 0.4–0.41. From this we may conclude that determination of the surface composition of a sample at room temperature is correct, as well as the result of measurements at a cryogenic temperature. The evaporated layer composition determined from the spectra in Figs. 2a and 2b by direct count of the number of carbon (with subtraction of those entering into the composition of residual gas phase, CO and CH_4) and tungsten atoms corresponded to the formulas $CW_{1.6}$ and $CW_{1.5}$, respectively. In other cases, when the spectra were measured at room temperature for $\omega \geq 0.4$, it was possible to reliably determine the surface composition of a ribbed crystal. It was found that this composition corresponded to WC_x with x varying from 2.3 in the initial stages of ribbed crystal formation (a carbon-rich sample not subjected to field or thermal evaporation) to $x = 1.3$–1.8 (in most cases of medium carbon content) and to $x = 0$ (upon complete removal of a carbidized layer, whereby a tungsten core was reached as manifested by the typical W^{+3}, W^{+4}, and W^{+2} ions).

An analysis of the spectra presented in Fig. 2 (and many others) revealed a large variety of molecular and cluster ions detected in the evaporated flux. The spectra contain significant peaks corresponding to almost all

[1] This number of accumulated ions (200 for $n \approx 100$) indicates that (although the informative pulses accounted for only 5–8.3% of the total number of pulses N), each working pulse carried on the average two ions (real number could vary from one to four).

ions of the formula $(W_mC_k)_f^{+s}$ (where $m = 1, 2, 3$; $k = 1, 2, 3, 4$; $f = 1, 2$; and $s = 2, 3$). In addition to the tungsten–carbon ions, the spectra also display carbon and tungsten species of the types C^{+2}, C_2^{+3}, C_3^{+2}, W_2^{+3}, and W_4^{+3}. Such a variety of ion species and the presence of polymerized (cluster) ions is surprising only at first glance. In fact, the presence of carbon cluster ions is typical of the field evaporation of graphite [8], although such ions are formed in extremely high fields. The carbon-saturated layer of a ribbed crystal contains excess carbon as compared to the amount that can be adsorbed on a tungsten crystal lattice. The material formed in the surface layers of such a ribbed crystal probably occurs in a nonequilibrium state and contains weak interatomic bonds besides strong ones. This can facilitate the formation of ion cluster ions such as $(WC)_4^{+3}$, $(W_2C)_2^{+3}$, and $W_3C_2^{+2}$ in the course of field evaporation. The lattice of a stoichiometric equilibrium CeB_6 crystal [9] also readily emitted cluster ions because of the presence of weak internal interatomic bonds. Ions such as W_4^{+3} can form upon breakage of the nonequilibrium carbon–tungsten formations. The energy of ionization required for the formation of such W_4^{+3} ions is smaller than that required for W^{+3} ions. The breakage of a greater number of bonds can be also explained by the presence of weak bonds.

The presence of purely carbon ions (C_3^{+2}, C_2^{+3}, etc.) requires special consideration because the ions of some residual gases also fall within the same range of masses (more precisely, of the mass to charge ratios, m/q). The origin of ions observed in this range was elucidated by analysis of the curves of the accumulation of ions of certain selected types. In the case of ions originating from a crystal lattice, the curves exhibit coarse steps [10], while ions representing particles adsorbed from the gas phase (uniformly arriving in the ionization region) are smooth and consist of small steps [11]. A coarse-step appearance confirmed the lattice origin of the observed cluster and atomic carbon ions.

We failed to observe purely atomic evaporation of W and C (usually taking place during the field evaporation of carbides [12] and many metal alloys [5]) neither at room temperature nor at a cryogenic temperature. Apparently atomic evaporation is more likely in the case of a chemically equilibrium crystal (such as WC) at low temperatures and strong electric fields.

As for the large variety of the molecular and cluster ions that have evaporated from ribbed crystals, the fields can be much lower as compared to those required for the evaporation of pure carbon or tungsten. We have calibrated the field by means of the current–voltage characteristics [13] using the published data on the electron work function of a carbidized tungsten [7]:

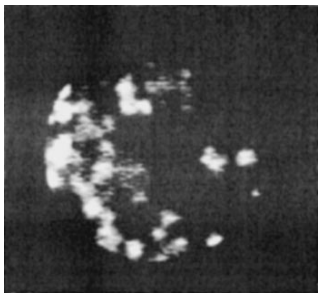

Fig. 3. Field ion desorption image of a thermal-field microroughnesses on the surface of a ribbed crystal heated to about 1300 K.

4.27 and 4.34 eV for the initial and final surface in the course of the field evaporation. These estimates showed that the electric field strength necessary for the evaporation of various ions of the W_mC_k type, as well as the W_2^{+3} and W_4^{+3} species, falls within the interval from 9×10^7 to 1.9×10^8 V/cm (depending on a particular spectrum and ion collection time). As the carbidized surface layer is removed and the carbon content in the WC_x formula decreases from $x = 1$ to zero, the applied voltage (and the field) necessary for the field evaporation increases. The evaporation of W^{+3} and W^{+4} ions from pure tungsten corresponded to the well-known value of 5×10^8 V/cm [5].

At a sample temperature of 1300–1600 K, measurements in the regime of field ion desorption microscopy showed intense field evaporation. The sample surface exhibited the formation of microroughnesses visualized by their own ions (Fig. 3). These microroughnesses walked over the surface, formed rings around plane crystal faces, and then collapsed at the centers of these faces. This behavior was analogous to that observed for the high-temperature field evaporation of some pure metals such as iridium [14]. However, the collapse of rings formed by microroughnesses was not observed on pure tungsten (although it is not excluded that this phenomenon may take place at significantly higher temperatures).

We failed to obtain a high-temperature field evaporation mass spectrum. At elevated temperatures, intense field evaporation took place already at V_b and the atom probe detected a typical noise spectrum of separate lines (sometimes of double, triple or greater intensity). However, it was possible to measure such a noise spectrum at a given V_b at $V_p = 0$ and then compare this to the noise spectrum measured for the same V_b and a possible maximum of $V_p \neq 0$ (in our case, $V_p = 6.2$ kV). In the region of light ions with m/q from 0 to 300 (the total uniform spectrum extended up to $m/q = 2000$), the latter spectrum exhibited a greater number of lines with large amplitudes, significantly exceeding a statistically reasonable amount observed in the former case. However, it would be incorrect to attempt to assign these lines to

certain m/q values of expected ions. We can only state that there was a certain contribution due to application of the pulsed voltage component. Nevertheless, it was interesting to measure the ion accumulation curves in the course of evaporation at V_b. These curves displayed several (up to five or six) regions separated by almost horizontal plateaus. The regions of buildup corresponded to the moments of time when a walking microroughness passed under the probing hole. Using the total number of ions evaporated at V_b, it was possible to estimate the ion current in the regime of high-temperature field evaporation from walking microroughnesses. In this regime, the total ion current collected from the sample point amounted up to 10^{-14}–10^{-13} A.

Acknowledgments. This study was supported by the Russian Foundation of Basic Research (project no. 01-02-17803) and by the Ministry of Science and Technology of the Russian Federation (project no. 10-012-1-1-1152).

REFERENCES

1. R. J. Klein, J. Chem. Phys. **22**, 1406 (1954).
2. A. P. Komar and Yu. N. Talanin, Izv. Akad. Nauk SSSR, Ser. Fiz. **22**, 580 (1958).
3. M. V. Loginov and V. N. Shrednik, Pis'ma Zh. Tekh. Fiz. **24** (11), 45 (1998) [Tech. Phys. Lett. **24**, 432 (1998)].
4. R. B. Kotel'nikov, S. N. Bashlykov, Z. K. Galiakbarov, and A. I. Kashtanov, *Superrefractory Elements and Their Compounds: A Handbook* (Metallurgiya, Moscow, 1969), pp. 260–263.
5. M. K. Miller and G. D. W. Smith, *Atom Probe Microanalysis: Principles and Applications to Material Problems* (Materials Research Society, Pittsburgh, 1990; Mir, Moscow, 1993).
6. M. V. Loginov, O. G. Savel'ev, and V. N. Shrednik, Zh. Tekh. Fiz. **64** (8), 123 (1994) [Tech. Phys. **39**, 811 (1994)].
7. O. L. Golubev, B. M. Shaĭkhin, and V. N. Shrednik, Pis'ma Zh. Tekh. Fiz. **1**, 714 (1975) [Sov. Tech. Phys. Lett. **1**, 313 (1975)].
8. N. M. Blashenkov and G. Ya. Lavrent'ev, Pis'ma Zh. Tekh. Fiz. **22** (7), 1 (1996) [Tech. Phys. Lett. **22**, 293 (1996)].
9. V. N. Gurin, M. M. Korsukova, M. V. Loginov, and V. N. Shrednik, Pis'ma Zh. Tekh. Fiz. **27** (10), 74 (2001) [Tech. Phys. Lett. **27**, 427 (2001)].
10. M. V. Loginov and V. N. Shrednik, Zh. Tekh. Fiz. **67** (8), 102 (1997) [Tech. Phys. **42**, 1075 (1997)].
11. M. V. Loginov, O. G. Savel'ev, and V. N. Shrednik, Pis'ma Zh. Tekh. Fiz. **19** (24), 71 (1993) [Tech. Phys. Lett. **19**, 802 (1993)].
12. W. Sha, L. Chang, G. D. W. Smith, *et al.*, Surf. Sci. **266**, 416 (1992).
13. V. N. Shrednik, *Filamentless Cathodes* (Sov. Radio, Moscow, 1974), pp. 165–169.
14. V. G. Butenko, O. L. Golubev, E. L. Kontorovich, and V. N. Shrednik, Pis'ma Zh. Tekh. Fiz. **18** (8), 80 (1992) [Sov. Tech. Phys. Lett. **18**, 275 (1992)].

Translated by P. Pozdeev

Technical Physics Letters, Vol. 29, No. 7, 2003, pp. 533–536. Translated from Pis'ma v Zhurnal Tekhnicheskoĭ Fiziki, Vol. 29, No. 13, 2003, pp. 10–18.

Mechanisms Complicating the Dependence of the Transient Process Duration on the Initial Conditions in Two-Dimensional Maps

A. A. Koronovskiĭ* and A. E. Khramova

Saratov State University, Saratov, Russia
State Scientific Center "College," Saratov, Russia
** e-mail: alkor@cas.ssu.runnet.ru*

Received January 21, 2003

Abstract—Mechanisms leading to complication of the dependence of a transient process duration on the initial conditions upon a change in control parameters of a two-dimensional dynamical system with discrete time (Eno map) are considered. It is shown that the character of this dependence for a stable cycle is determined by multiplicators. A change in the control parameters in the same dynamical regime produces a bifurcation leading to reclosure of the stable and unstable manifolds. This results in a qualitative complication of the dependence of the transient process duration on the initial conditions in the system. © *2003 MAIK "Nauka/Interperiodica".*

In recent decades, nonlinear dynamical systems have received much attention. Irrespective of the system type (discrete or continuous time, lumped or distributed parameters), the effort is concentrated on studying established regimes and on determining how one dynamical regime is changed by another in response to variations of the control parameters [1, 2]. At the same time, the transient processes are considered as secondary and not studied in much detail. However, transient processes carry important information about the system and sometimes it is more expedient to consider behavior of a system in the transient stage [3–5] rather than on attaining the attractor.

The range of problems closely related to the description of transient processes is rather wide, including elucidation of the structure of attraction basins of the existing attractors and their boundaries in cases of multistability [6, 7], study of transient chaos [8, 9] as a process accompanying crises of chaotic attractors [10, 11], and determination of the lifetime of an imaging point in a small region of the phase space of a system with controlled chaos [12–14]. Thus, transients play an important role in the behavior of dynamical systems and are worthy of detailed investigation. Such processes are usually studied in dynamical systems with discrete time: while being relatively simple, such system can feature all the main nonlinear phenomena characteristic of both distributed and current dynamical systems.

Previously [16], we have studied transient processes in a two-dimensional system with discrete time (Eno map [17]) of the type

$$\begin{aligned} x_{n+1} &= \lambda x_n(1 - x_n) + by_n, \\ y_{n+1} &= x_n, \end{aligned} \tag{1}$$

in the simplest dynamic regime representing a stable cycle of period 1. Dependence of the transient process duration on the initial conditions, $T_\varepsilon(x_0, y_0)$, was determined for a given initial point (x_0, y_0) and preset accuracy ε using the same method as in [15, 16, 18, 19].

The results obtained in [16] revealed a mechanism leading to complication of the dependence of the transient process duration on the initial conditions, $T_\varepsilon(x_0, y_0)$, in the Eno map for a cycle of period 1. It was found that the character of this dependence is determined by multiplicators $\mu_{1,2}$ of a stable immobile point (x_0, y_0) and by the stable and unstable manifolds of the stable and unstable points. In particular, it was demonstrated that, in a given dynamic regime, the minima of the transient process duration coincide with points of the stable manifold corresponding to a multiplicator with minimum absolute value. Initially, for small values of λ and $b > 0$, the multiplicators obey the relation $|\mu_1| < |\mu_2|$ and the minima of $T_\varepsilon(x_0, y_0)$ correspond to a manifold characterized by the negative multiplicator μ_1. For $\lambda = \lambda_{eq}$, whereby $|\mu_1| = |\mu_2|$, both manifolds become significant. When $\lambda > \lambda_{eq}$, $|\mu_2|$ becomes smaller than $|\mu_1|$ and the manifolds change their roles: minimum values of the transient process duration correspond to a manifold characterized by the positive multiplicator μ_2. This results in complication of the behavior of $T_\varepsilon(x_0, y_0)$.

This study is aimed at tracing a change in the dependence of the transient process duration on the initial conditions in the Eno map (1) for a more complicated periodic dynamic regime. A bifurcation analysis of the map (1) shows that, when the control parameter falls in

1063-7850/03/2907-0533$24.00

the interval $3(1-b) < \lambda < 1-b+\sqrt{6-8b+6b^2}$, the (x, y) plane contains two unstable points, (0, 0) and (x^0, y^0) (where $x^0 = y^0 = (\lambda + b - 1)/\lambda$), and a stable cycle of period 2 with the elements (x^1, y^1) and (x^2, y^2),

$$x^1 = \frac{1+\lambda-b+\sqrt{\lambda^2+2\lambda(b-1)-3(b-1)^2}}{2\lambda}, \qquad y^1 = -\frac{-1-\lambda+b+\sqrt{\lambda^2+2\lambda(b-1)-3(b-1)^2}}{2\lambda},$$
$$x^2 = -\frac{-1-\lambda+b+\sqrt{\lambda^2+2\lambda(b-1)-3(b-1)^2}}{2\lambda}, \qquad y^2 = \frac{1+\lambda-b+\sqrt{\lambda^2+2\lambda(b-1)-3(b-1)^2}}{2\lambda}, \tag{2}$$

and the multiplicators

$$\mu_1^{2c} = \frac{4-\lambda^2+2\lambda(1-b)-6b+4b^2-\sqrt{-4b^2+(-4+\lambda^2+2\lambda(b-1)+6b-4b^2)^2}}{2},$$
$$\mu_2^{2c} = \frac{4-\lambda^2+2\lambda(1-b)-6b+4b^2+\sqrt{-4b^2+(-4+\lambda^2+2\lambda(b-1)+6b-4b^2)^2}}{2}. \tag{3}$$

Figure 1 shows the plots of multipliers μ_1^{2c} and μ_2^{2c} versus control parameter λ for a fixed value of $b = 0.1$. The region of complex values of the multiplicators (for $2.91246 < \lambda < 3.0095$) corresponds to a gap in Fig. 1. At $\lambda = 2.91246$ and $\lambda = 3.0095$, which corresponds to the boundaries of the gap, the multiplicators μ_1^{2c} and μ_2^{2c} are equal. In the region of $\lambda < 2.91246$, multiplicator μ_1^{2c} is initially positive and close to zero and then slowly increases to approach 0.1. At the same time, multiplicator μ_2^{2c} decreases from 1 to 0.1. Thus, in the entire interval of $2.7 < \lambda < 2.91246$, the absolute value of μ_1^{2c} is smaller than that of μ_2^{2c}. On the other side of the gap, at $\lambda = 3.0095$, both multiplicators are equal to –0.1. In the region of $\lambda > 3.0095$, the absolute value of μ_2^{2c} is smaller than that of μ_1^{2c}. As λ increases from 3.0095 to 3.1935, multiplicator μ_1^{2c} decreases from –0.1 to –1. In the interval $2.91246 < \lambda < 3.0095$, the quantities μ_1^{2c} and μ_2^{2c} are complex conjugate and obey the condition $|\mu_1^{2c}| = |\mu_2^{2c}|$.

A comparison of the projection of the $T_\varepsilon(x_0, y_0)$ surface onto the plane of initial conditions (x_0, y_0) (Figs. 2a and 2b) to the arrangement of stable manifolds of a stable cycle (2) of period 2 (Fig. 3a and 3b) reveals a pattern analogous to that described in [16]. According to this, the minima of the transient process duration coincide with a manifold corresponding to the multiplier possessing a minimum absolute value (light bands in

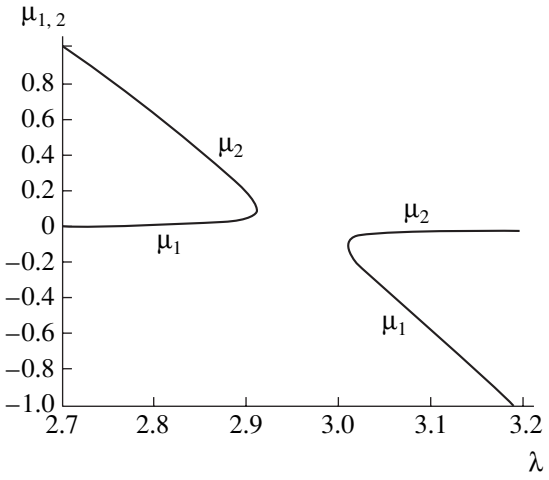

Fig. 1. The plot of multipliers μ_1^{2c} and μ_2^{2c} versus control parameter λ for a fixed value of $b = 0.1$. The gap corresponds to the region of complex conjugate multiplicators.

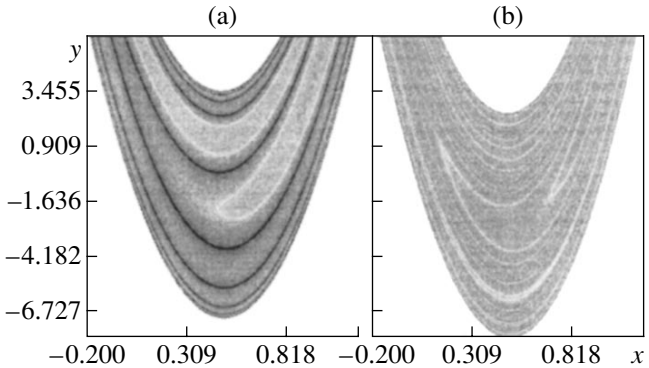

Fig. 2. Projections of the surface $T_\varepsilon(x_0, y_0)$, representing the transient process duration as a function of the initial conditions, on the plane of possible states (x, y) for the Eno map with (a) $\lambda = 2.75$, $b = 0.1$ and (b) $\lambda = 3.16$ and $b = 0.1$. Variations in the transient process duration are reflected by the gray color gradations: from white (corresponding to $T = 0$) to black (corresponding to $T = 200$ units of the discrete time). A light-gray shade outside the basin of attraction of the cycle of period 2 corresponds to the initial conditions with an attractor at infinity.

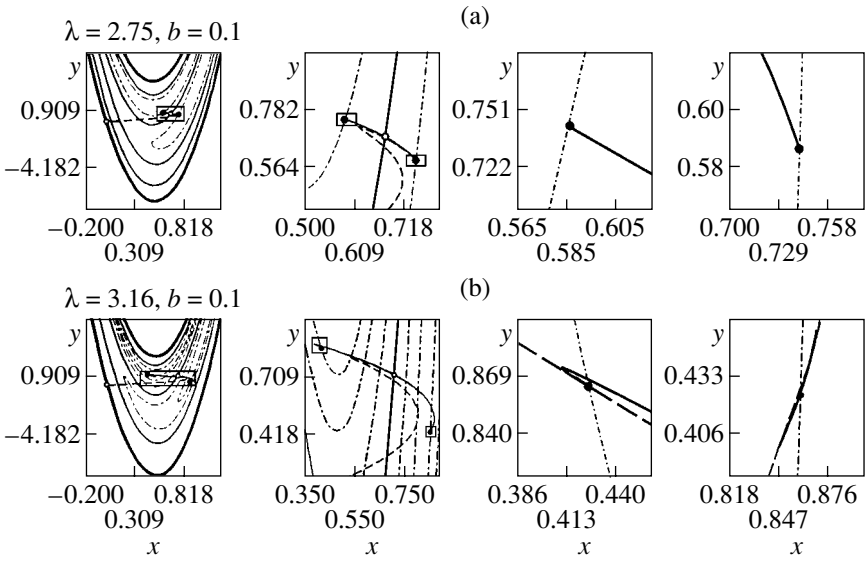

Fig. 3. (a) Schematic diagrams showing manifolds, the unstable immobile points (0, 0) and (x^0, y^0), and the elements of the cycle of period 2 for the fixed value of the control parameter ($b = 0.1$) and the parameter $\lambda = 2.75$. For these parameters, the cycle of period 2 is characterized by the multiplicators $\mu_1^{2c} = 0.0123$ and $\mu_1^{2c} = 0.815$. In the first panel, a thick solid curve shows the stable manifolds for the unstable point (0, 0); dashed curves show the unstable manifold of the same point. One thin solid curve represents the stable manifold of the unstable immobile point (x^0, y^0). Another thin solid curve, passing through the unstable immobile point (x^0, y^0) and the elements of the cycle of period 2 (black circles) represents the unstable manifold of this point. Dash–dot curves show the stable manifold of the cycle of period 2 characterized by the maximum absolute value of μ_2^{2c}. Panels on the right show increasing fragments of the manifolds in the vicinity of immobile points and the elements of the cycle of period 2. (b) Schematic diagrams showing manifolds, the unstable immobile points (0, 0) and (x^0, y^0), and the elements of the cycle of period 2 for the fixed value of the control parameter ($b = 0.1$) and the parameter $\lambda = 3.16$. For these parameters, the cycle of period 2 is characterized by the multiplicators $\mu_1^{2c} = -0.846$ and $\mu_2^{2c} = -0.012$. Here, dash–dot curves show the stable manifold of the cycle of period 2 characterized by the maximum absolute value of μ_1^{2c}. Panels on the right show increasing fragments of the manifolds in the vicinity of immobile points and the elements of the cycle of period 2. In the two last fragments, the dashed line indicates the second stable manifold of the cycle of period 2 corresponding to the multiplicator μ_2^{2c}.

Figs. 2a and 2b). Dark regions, corresponding to the maximum durations of the transient process, coincide with a stable manifold of the unstable cycle of period 1. At the same time, it is seen that the character of the $T_\varepsilon(x_0, y_0)$ projection is significantly complicated at $\lambda > 3.0095$, as manifested by the appearance of an infinite number of minima accumulated on approaching the stable manifold of the unstable cycle of period 1.

In order to explain this phenomenon, let us consider (as in [16]) the behavior of manifolds of the unstable points and the stable cycle of period 2. The stable manifold of the unstable point (0, 0) forms the boundary of the attraction basin. The unstable manifold of this unstable point asymptotically tends to the unstable immobile point (x^0, y^0) along the unstable manifold of the unstable immobile point (x^0, y^0) and does not significantly influence the character of $T_\varepsilon(x_0, y_0)$.

Since the unstable manifold of the point (0, 0) intersects the stable manifold an infinite number of times in the vicinity of the point (x^0, y^0), the stable manifold of the point (x^0, y^0) also intersects the unstable manifold an infinite number of times in the vicinity of the point (0, 0) (see [16]). As was noted above, the stable manifold of the point (x^0, y^0) on the projection of the $T_\varepsilon(x_0, y_0)$ surface onto the (x_0, y_0) plain corresponds to the maxima of the transient process duration (dark bands in Fig. 2a).

The unstable manifold of the unstable point (x^0, y^0) tends to each element of the stable cycle (2) of period 2 in the direction of the stable manifold of this cycle, which is characterized by a greater absolute value of the multiplier and, hence, by slower convergence to the attractor (Figs. 3a and 3b). For the control parameter in the interval $2.7 < \lambda < 2.91246$, the behavior of the unstable manifold of the unstable point (x^0, y^0) in the vicinity of each element of the stable cycle of period 2 is determined by multiplicator μ_2^{2c}, whereas in the region of $3.0095 < \lambda < 3.1935$, the behavior is determined by multiplicator μ_1^{2c}. In the interval $2.91246 <$

$\lambda < 3.0095$, the multiplicators of the cycle of period 2, μ_1^{2c} and μ_2^{2c}, are complex conjugate and, hence, a stable cycle of period 2 has no stable and unstable manifolds. In this case, the dependence of the transient process duration on the initial conditions exhibits two clearly pronounced minima coinciding with elements of the stable cycle of period 2. The maximum values of the transient process durations still correspond to the initial conditions belonging to the stable manifold of the unstable point (x^0, y^0).

As can be seen from Fig. 1, the multiplicators μ_1^{2c} and μ_2^{2c} are positive for $2.7 < \lambda < 2.91246$ and both are negative for $3.0095 < \lambda < 3.1935$. Thus, in the latter interval, the unstable manifold of the point (x^0, y^0) intersects an infinite number of times the stable manifolds of a stable cycle of period 2 characterized by negative multiplicators and "wounds" on the immobile point. As a result, the stable manifold of the cycle of period 2 characterized by multiplier μ_1^{2c} with a maximum absolute value also intersects an infinite number of times the unstable manifold of the unstable point (x^0, y^0). This leads to the appearance of an infinite number of minima in the projection of the $T_\varepsilon(x_0, y_0)$ surface (Fig. 3b). An analogous mechanism accounts for complication of the character of $T_\varepsilon(x_0, y_0)$ within the same dynamic regime for cycles of period 4, 8, etc.

Thus, the transient processes of minimum duration in dynamic systems with discrete time correspond to the initial conditions (x^0, y^0) belonging to that stable manifold of the stable cycle which is characterized by a multiplicator with the maximum absolute value (the multiplier must be a real quantity). At the moment when a change in the control parameter (in the same dynamic regime) makes the multiplier with the maximum absolute value negative, the structure of the $T_\varepsilon(x_0, y_0)$ surface exhibits rearrangement and the dependence of the transient process duration on the initial condition becomes complicated. Such a complication, related to a change in the roles of the multiplicators, can be either due to the fact that multiplicators become complex (for cycles of period 2, 4, etc.) on the Eno map, or due to a situation when the absolute value of one multiplier increases and that of the other decreases, while both multiplicators remain real (as in the case of a stable immobile point, see [16]).

Acknowledgments. This study was supported by the Russian Foundation for Basic Research, project no. 01-02-17392.

REFERENCES

1. A. Venkatesan and M. Lakshmanan, Phys. Rev. E **58**, 3008 (1998).
2. M. C. Depassier and J. Mura, Phys. Rev. E **64**, 056217 (2001).
3. É. V. Kal'yanov, Pis'ma Zh. Tekh. Fiz. **26** (15), 26 (2000) [Tech. Phys. Lett. **26**, 656 (2000)].
4. B. P. Bezruchko, T. V. Dikanev, and D. A. Smirnov, Phys. Rev. E **64**, 036210 (2001).
5. A. A. Koronovskiĭ, D. I. Trubetskov, A. E. Khramov, and A. E. Khramova, Dokl. Akad. Nauk **383**, 322 (2002) [Dokl. Phys. **47**, 181 (2002)].
6. A. N. Pisarchik, Phys. Rev. E **64**, 046203 (2001).
7. A. P. S. De Morua and C. Grebogi, Phys. Rev. Lett. **86**, 2778 (2001).
8. M. Dhamala *et al.*, Phys. Rev. E **64**, 056207 (2001).
9. L. Zhu *et al.*, Phys. Rev. Lett. **86**, 4017 (2001).
10. K. G. Szabo *et al.*, Phys. Rev. E **61**, 5019 (2000).
11. H. B. Stewart *et al.*, Phys. Rev. Lett. **75**, 2478 (1995).
12. R. Meucci *et al.*, Phys. Rev. E **52**, 4676 (1995).
13. P. J. Aston and P. K. Marriot, Phys. Rev. E **57**, 1181 (1998).
14. V. Paar and H. Buljan, Phys. Rev. E **62**, 4869 (2000).
15. A. V. Astakhov *et al.*, Radiotekh. Élektron. (Moscow) **38**, 291 (1993).
16. A. A. Koronovskiĭ and A. E. Khramov, Pis'ma Zh. Tekh. Fiz. **28** (15), 61 (2002) [Tech. Phys. Lett. **28**, 648 (2002)].
17. M. Henon, in *Strange Attractors*, Ed. by Ya. G. Sinai and L. P. Shil'nikov (Mir, Moscow, 1981), p. 152.
18. A. A. Koronovskiĭ, A. E. Khramov, and A. V. Starodubtsev, Izv. Vyssh. Uchebn. Zaved., Prikl. Nelineĭnaya Din. **10** (5), 25 (2002).
19. A. A. Koronovskiĭ, D. I. Trubetskov, A. E. Khramov, and A. E. Khramova, Izv. Vyssh. Uchebn. Zaved., Radiofiz. **45**, 880 (2002).

Translated by P. Pozdeev

Technical Physics Letters, Vol. 29, No. 7, 2003, pp. 537–539. Translated from Pis'ma v Zhurnal Tekhnicheskoĭ Fiziki, Vol. 29, No. 13, 2003, pp. 19–25.

A Criterion for Convection of Elementary Excitations in Crystalline Solids

K. K. Kazbekov, Zh. Kh. Murlieva, and D. K. Palchaev

Dagestan State University, Makhachkala, Dagestan, Russia

e-mail: dairpalchaev@mail.dgu.ru

Received January 21, 2003

Abstract—A universal method is suggested that provides empirical estimates of the kinetic coefficients in the equations of quasiparticle transfer in crystalline structures. The method is based on a criterion for the onset of Landau convection and on an analysis of experimental data on the electric and thermal resistance and the thermal expansion coefficient for crystals with different types of interatomic bonds. *© 2003 MAIK "Nauka/Interperiodica".*

Kinetic coefficients in transfer equations are complex functions of temperature. These functions are determined by the contributions of various elementary excitations to the conductivity and by different mechanisms of scattering of these excitations. As the temperature varies from $T = 0$ K to the melting point, the kinetic coefficients change by many orders of magnitude due to the scattering of quasiparticles on phonons.

An important achievement in the theory of transfer processes in condensed media was the development of an approach (see, e.g. [1]) to determining the kinetic coefficients without solving the corresponding transfer equation. The formal expressions for these coefficients are essentially the exact solutions of the kinetic equations, a peculiarity of which is that the coefficients are related to the correlation function of physical fluxes in the equilibrium state [2, 3]. Explicitly, the kinetic coefficients are expressed, in the first approximation with respect to deviations of the density operator from the equilibrium state, using the Kubo formula [2–4]. However, transformation of the formal expressions in order to obtain a particular physical interpretation encounters considerable difficulties [2, 4]. For this reason, the only really possible way of calculating the kinetic coefficients in some cases (primarily, for crystalline systems) is offered by the variation method based on the solution of the kinetic equation [5]. A solution of the linearized kinetic equation can be obtained proceeding from a phenomenological transfer equation.

In usual nonequilibrium thermodynamics, the flux density $\mathbf{j}$ is proportional to the gradient of an external field potential Y,

$$\mathbf{j} = -\sigma \operatorname{grad} Y, \tag{1}$$

where σ is the corresponding kinetic coefficient. In the case of a crystalline structure, a physical flux can be considered as the thermal diffusion of quasiparticles representing elementary quantum excitations in the medium. At any finite temperature, the system of such quasiparticles is an almost ideal gas of excitations in which spontaneous convection is hindered by the interaction between quasiparticles [6].

In the case of a sufficiently dense gas of quasiparticles (i.e., when the medium can be considered as a continuum), a criterion for the onset of convection can be expressed using the Landau condition [7],

$$dS/dx = 0, \tag{2}$$

where S is the entropy of the subsystem of particles under consideration, varying depending on the linear parameter x. In the general case, S is a function of the external field potential, the temperature, and the pressure. At a given temperature T, the entropy is $S = S(Y, P)$ and condition (2) can be rewritten as [7]

$$\frac{dS}{dx} = \left(\frac{\partial S}{\partial T}\right)_P \left(\frac{\partial T}{\partial Y}\right)_P \frac{dY}{dx} + \frac{g}{V}\left(\frac{\partial V}{\partial T}\right)_P = 0. \tag{3}$$

In the case of crystals, the subsystem volume can change only as a result of variation of the atomic volume. Therefore, the term $1/V(\partial V/\partial T)_P$ in Eq. (3) represents the thermal expansion coefficient (TEC) of the crystal. A dynamic interaction between the gas particles in Eq. (3) is described by the force parameter g (see [7]) possessing a dimensionality of acceleration. Using the well-known thermodynamic relations, Eq. (3) can be written in the following form:

$$-\frac{dY}{dx} = \frac{g}{c_P t_Y}\beta T, \tag{4}$$

where c_P is the heat capacity of the system and $t_Y \equiv (\partial T/\partial Y)_P$ is the temperature matching factor describing variations of the crystal temperature under the action of the external field.

Using the convection onset condition in the form of (4) and transfer equation (1), we obtain a phenome-

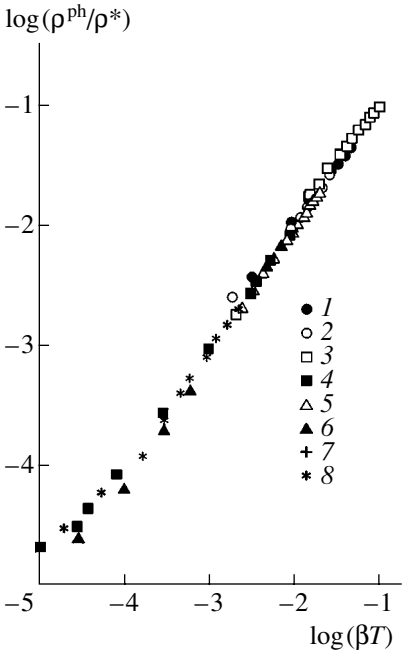

Fig. 1. A correlation between the electric resistance and the isobaric thermal deformation for copper (by data summarized in [8]).

nological expression for the corresponding averaged values of the kinetic coefficients σ_i,

$$\sigma_i^{-1} \equiv R_i = \left(\frac{g}{jc_P t_Y}\right)_i \beta T. \quad (5)$$

In particular, for $\beta T \longrightarrow 1$, condition (2) gives the following characteristic resistance of the *i*th subsystem:

$$R_i^* = \left(\frac{g}{jc_P t_Y}\right)_i^*. \quad (6)$$

Formula (5) leads to an important conclusion according to which

$$\frac{R_i}{R_i^*} = \beta T; \quad (7)$$

that is, the reduced resistances of subsystems in a crystal are given by a universal function directly related to the crystal lattice. This conclusion can be corroborated by two examples: the electric resistance of a metal and thermal resistance of a dielectric. The transfer processes involving fermions (electrons in metals) or bosons (phonons in nonmetallic crystals) obey the model of convective charge and heat transfer with a nonzero gradient of the electric potential and the temperature field, respectively. In experimental justification of relation (7), especially important data are provided by measurements of the temperature dependence of the kinetic coefficients and TEC of the same object measured in one experiment.

The electric resistance and TEC of metals from various groups of the Periodic Table (Cu, Zn, Al, Pb) in the temperature interval from 100 to 500 K were measured on the same samples under identical conditions. This temperature interval contains the regions above and below the Debye temperature, in which the electric resistance is proportional to T^n, where n varies from ~3 to 1, and is usually described by the Bloch–Grüneisen interpolation formula [4].

The measurements were performed in a setup representing a quartz dilatometer with a photoelectric detector of displacements. The samples were provided with electric contacts. The junctions of chromel–alumel thermocouples fastened at two points of the sample also served as potential probes. The relative errors of determination of the electric resistance and TEC did not exceed 0.5 and 0.3%, respectively.

An analysis of the experimental data showed that the electric resistance and the isobaric thermal deformation for all metals obey linear relations with the correlation coefficients r close to unity. The corresponding expressions are as follows:

for copper (r = 0.9990):

$$\rho = -0.0412 \times 10^{-8} + 1.184 \times 10^{-6} \beta T; \quad (8)$$

for zinc (r = 0.9995):

$$\rho = 0.0396 \times 10^{-8} + 2.23 \times 10^{-6} \beta T; \quad (9)$$

for aluminum (r = 0.9995):

$$\rho = 0.123 \times 10^{-8} + 1.27 \times 10^{-6} \beta T; \quad (10)$$

and for lead (r = 0.9990):

$$\rho = 0.439 \times 10^{-8} + 8.14 \times 10^{-6} \beta T. \quad (11)$$

In these relations, the first terms correspond to the scattering of electrons on static defects and the second terms (ρ^{ph}) reflect the scattering on phonons. The linear coefficients in expressions (8)–(11) are essentially the characteristic electric resistances ρ^*, representing the limits to which the phonon resistances tends for $\beta T \longrightarrow 1$. Analogous relations are observed at low and high temperatures. For illustration, Fig. 1 shows a correlation between ρ^{ph}/ρ^* and βT for copper plotted using the data of various researchers summarized in [8]. Data on the thermal expansion were taken from [9]. From among about two hundred temperature dependences of the electric resistance presented in [8], we selected those for the widest and most different temperature intervals, ranging from ~20 K up to the melting temperature of copper (1375 K). The correlation coefficients for all results were not lower than 0.999. At temperatures below ~20 K, the correlation is not as good, probably because of competition between the electron–phonon and electron–electron collisions [10]. A linear relation between the electric resistance and the isobaric thermal deformation was also observed for transition metals [11] at temperatures both above and below the Curie point.

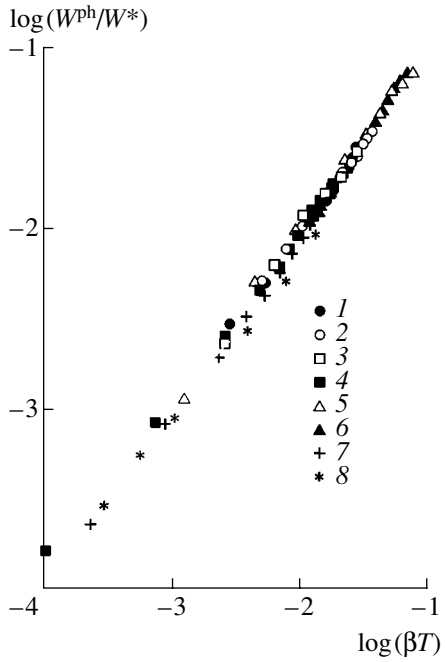

Fig. 2. A correlation between the thermal resistance and the isobaric thermal deformation for various crystalline solids (data from [9, 12–16]): (*1*) KCl (0.997; 60–300 K); (*2*) NaCl (0.999; 80–300 K); (*3*) SiO_2 (0.996; 100–600 K); (*4*) SiC (0.998; 200–1200 K); (*5*) MgO (0.995; 120–1600 K); (*6*) BeO (0.998; 573–1673 K); (*7*) Si (0.999; 120–1100 K); (*8*) diamond (0.998; 150–1000 K).

An analysis of the experimental data on the thermal resistance W and TEC, including reference data [9, 12–15] and our experimental results for silicon [16], leads to analogous relations between the phonon resistance W^{ph} and βT for nonmetallic single crystals. Figure 2 shows a correlation between W^{ph}/W^* and βT in a broad temperature range for various substances with different types of interatomic bonds (figures in parentheses give the values of correlation coefficients and indicate the temperature intervals in which reliable data on W and β were available).

Thus, we may ascertain that the generalized model of the Landau convective transfer adequately describes the charge transfer by electrons and the heat transfer by phonons in crystalline solids.

REFERENCES

1. R. Kubo, *Lectures in Theoretical Physics: Proceedings of the Boulder Summer School*, Ed. by W. E. Brittin and L. G. Dunham (Interscience, New York, 1959), p. 120.
2. V. M. Mogilevskiĭ and A. F. Chudnovskiĭ, *Thermal Conductivity of Semiconductors* (Nauka, Moscow, 1972).
3. D. J. Thouless, *The Quantum Mechanics of Many-Body Systems*, 2nd ed. (Academic Press, New York, 1972; Mir, Moscow, 1975).
4. J. M. Ziman, *The Physics of Metals* (Cambridge University Press, Cambridge, 1969; Mir, Moscow, 1972), Vol. 1.
5. J. M. Ziman, *Electrons and Phonons* (Clarendon Press, Oxford, 1960; Inostrannaya Literatura, Moscow, 1962).
6. J. M. Ziman, *Elements of Advanced Quantum Theory* (Cambridge Univ. Press, Cambridge, 1969; Mir, Moscow, 1971).
7. L. D. Landau and E. M. Lifshitz, *Course of Theoretical Physics*, Vol. 6: *Fluid Mechanics* (Nauka, Moscow, 1986; Pergamon, New York, 1987).
8. R. A. Matula, J. Phys. Chem. Ref. Data **8**, 1147 (1979).
9. S. I. Novikova, *Thermal Expansion of Solids* (Nauka, Moscow, 1974).
10. V. F. Gantmakher and I. B. Levinson, *Scattering of Current Carriers in Metals and Semiconductors* (Nauka, Moscow, 1984).
11. Zh. Kh. Murlieva, D. K. Palchaev, and E. D. Borzov, Pis'ma Zh. Tekh. Fiz. **28** (18), 48 (2002) [Tech. Phys. Lett. **28**, 773 (2002)].
12. *Thermal Conduction in Solids*, Ed. by A. S. Okhotin (Énergoizdat, Moscow, 1984).
13. I. G. Kozhevnikov and L. A. Novitskiĭ, *Thermophysical Properties of Materials at Low Temperatures* (Mashinostroenie, Moscow, 1982).
14. *Acoustical Crystals*, Ed. by M. P. Shaskol'skaya (Nauka, Moscow, 1982).
15. R. E. Krzhizhanovskiĭ and Z. Yu. Shtern, *Thermophysical Properties of Nonmetallic Materials* (Énergiya, Leningrad, 1973).
16. D. K. Palchaev, A. B. Batdalov, Zh. Kh. Murlieva, *et al.*, Fiz. Tverd. Tela (St. Petersburg) **43**, 442 (2001) [Phys. Solid State **43**, 458 (2001)].

Translated by P. Pozdeev

Technical Physics Letters, Vol. 29, No. 7, 2003, pp. 540–541. Translated from Pis'ma v Zhurnal Tekhnicheskoĭ Fiziki, Vol. 29, No. 13, 2003, pp. 26–30.

The Effect of Neutron Irradiation on the Exciton Absorption in Gallium Arsenide

Z. V. Jibuti, N. D. Dolidze, B. E. Tsekvava, and G. L. Eristavi

Tbilisi State University, Tbilisi, Georgia

e-mail: nugo@geo.net.ge

Received January 15, 2003

Abstract—We have studied the effect of neutron irradiation on the exciton absorption in *n*-GaAs crystals. It is shown that the observed decrease in the absorption coefficient, broadening of the exciton peak, and its shift toward higher energies are caused by the electric and strain (compression) fields generated by the radiation-induced defects. © *2003 MAIK "Nauka/Interperiodica".*

We have studied the exciton absorption spectra of *n*-GaAs ($n = 10^{14}$ cm^{-3}) samples irradiated by fast neutrons at $T \le 60$°C to a total dose in the range of $\Phi = 10^{15}$–10^{18} cm^{-2}. The samples had the form of plane-parallel plates with thicknesses reduced by mechanical grinding and chemical etching to 4–5 μm. The procedure used for the sample preparation [1, 2] ensured the absence of residual stresses in the crystal structure. In the course of measurements, the samples occurred in a "free" state, whereby no mechanical stresses were induced by holding elements [1, 2]. The optical absorption spectra were measured at $T = 77$ K before and after neutron irradiation and in various states of subsequent isochronous thermal annealing. The samples were annealed in vacuum at various temperatures for 30 min.

Figures 1 and 2 show the optical absorption spectra measured before and after irradiation and in the course of isochronous annealing at various temperatures for the samples exposed to a total neutron dose of $\Phi = 10^{16}$ and 10^{17} cm^{-2}, respectively. As can be seen, the spectrum of unirradiated GaAs exhibits a clearly pronounced exciton structure. The neutron bombardment leads to a decrease in the intensity of absorption in the exciton region, whereby the absorption peak broadens and shifts toward higher energies. In the course of subsequent annealing, the coefficient of absorption in the exciton region increases and the peak maximum shifts toward the initial position.

In the samples irradiated to a total dose of $\Phi \le 10^{16}$ cm^{-2}, the annealing at $T = 600$°C results in the complete restoration of the initial exciton absorption peak (Fig. 1). At the same time, the treatment at this temperature was insufficient for the complete annealing of a material irradiated to higher neutron doses (Fig. 2).

The irradiation-induced broadening and decrease in intensity (up to complete vanishing) of the exciton peak can be explained by the presence of either the free charge carriers (screening the Coulomb interaction of the electron–hole pairs) or the local fluctuating electric fields (breaking the exciton states) in the samples. The latter fields can be generated either by localized charges of ionized impurity centers [3, 4] or by charged radiation defects [5–7]. Taking into account that the initial samples were not strongly doped and that neutron irradiation produces defects leading to compensation [7], it can naturally be suggested that a change in the exciton structure of the absorption edge is caused by the electric fields generated by fluctuating accumulations of charged radiation defects and disordered regions. The strength of the exciton-breaking field $E \approx 3$ kV/cm [4–6]. As can be seen from our experimental data, such fields are generated by the radiation defects in GaAs samples irradiated even to $\Phi = 10^{16}$ cm^{-2}.

The irradiation-induced shift of the exciton peak can be related to changes either in the bandgap width (ΔE_g)

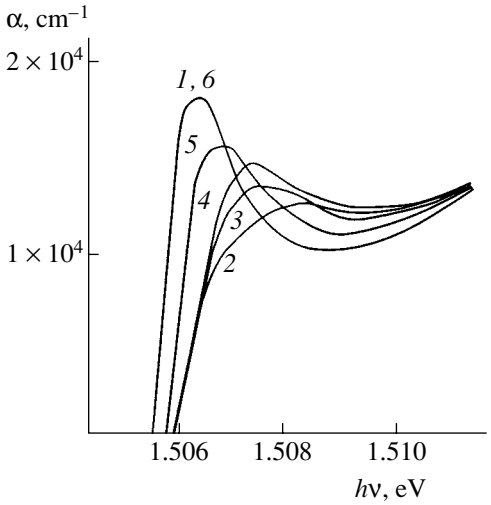

Fig. 1. Exciton absorption coefficient of *n*-GaAs (*1*) before and (*2*) after irradiation with fast neutrons to a total dose of $\Phi = 10^{16}$ cm^{-2} and upon subsequent isochronous thermal annealing to $T = 200$ (*3*), 300 (*4*), 500 (*5*), and 600°C (*6*).

1063-7850/03/2907-0540$24.00

or in the exciton binding energy (ΔE_{ex}). As is known, the exciton absorption peak in GaAs corresponds to the allowed "heavy" Wannier–Mott exciton [8]. The exciton binding energy is $E_{ex} = \mu e^4/2\hbar^2\varepsilon^2$, where ε is the permittivity of the crystal, $\mu = m_e m_h/(m_e + m_h)$, and m_e and m_h are the effective masses of electrons and holes, respectively. For GaAs, $\varepsilon = 13.1$, $m_e = 0.066m_0$ (in the central valley of the conduction band), and $m_h = 0.52m_0$ (for heavy holes), where m_0 is the mass of the free electron. As can be seen, a change in E_{ex} can be related to changes in both ε and μ values and by the Stark shift of the exciton level in the fluctuating electric field of the radiation-induced defects.

As for the Stark shift, the situation can be qualitatively analyzed as follows. The exciton ground level in GaAs corresponds to the S-state of the relative motion of the electron and hole. Therefore, the system must feature the quadratic Stark effect, whereby the exciton level shifts toward lower energies. Since the experiment reveals a shift of the absorption peak toward higher energies, we may conclude that the Stark effect is insignificant.

A more significant effect must be due to residual strain fields of internal stresses arising in GaAs in the course of neutron irradiation. As is known [9], the central lowest valley of the conduction band ($k = \langle 000\rangle$) and the side valley (on the axis $k = \langle 100\rangle$) with 0.34 eV higher energy are characterized by different pressure coefficients: $(dE_g/dP)_{\langle 000\rangle} = 11.3 \times 10^{-11}$ eV/Pa versus $(dE_g/dP)_{\langle 100\rangle} = -8.7 \times 10^{-11}$ eV/Pa. As the pressure increases, the two valleys approach one another and the lowest valley changes its type. Since the effective electron mass in the side valley is $m_{e\langle 100\rangle} = 1.2m_0 \gg m_{e\langle 000\rangle} = 0.066m_0$ [10], this change in the type of the lowest valley will modify the exciton energy via a change in μ.

Using the values of parameters given above, we can readily estimate the critical value of the stress σ_c leading to a change in the valley type and the corresponding changes in the exciton energy (ΔE_{ex}) and the bandgap width (ΔE_{gc}): $\sigma_c = 1.7 \times 10^9$ Pa, $\Delta E_{ex} = 20$ meV, and $\Delta E_{gc} = 0.192$ eV. Taking into account that the experimental shift of the exciton peak amounts to ~1 meV, we may conclude that the residual strain fields are significantly below the critical value. For relatively small lattice deformations, we can neglect the change in the exciton binding energy related to the ε and μ variations and consider the exciton level as shifting with the absorption band edge.

Thus, it is the strain-induced change in the bandgap width that is responsible for the exciton peak shift. According to the experimental data, a maximum displacement of the exciton absorption peak amounts to $\Delta E = 1$ meV. This corresponds to a maximum level of internal stresses $\sigma_{max} \approx 10^7$ Pa. Note that σ_{max} is in fact significantly lower than σ_c. The experimentally observed shift of the exciton peak toward shorter wavelengths suggests that the neutron irradiation of GaAs gives rise to compressive stresses [2].

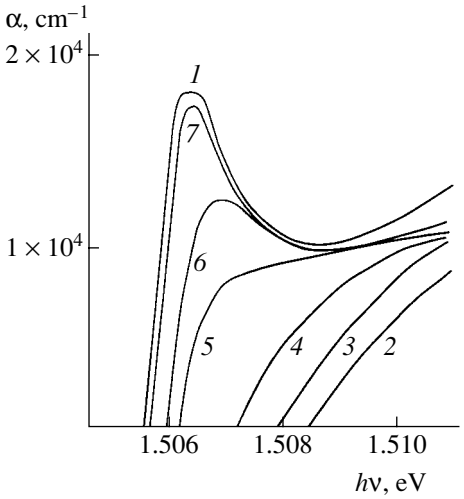

Fig. 2. Exciton absorption coefficient of *n*-GaAs (*1*) before and (*2*) after irradiation with fast neutrons to a total dose of $\Phi = 10^{17}$ cm^{-2} and upon subsequent isochronous thermal annealing to $T = 250$ (*3*), 350 (*4*), 450 (*5*), 500 (*6*), and 600°C (*7*).

Since no shift of the exciton absorption peak is observed in electron-irradiated GaAs samples [5, 6], it can naturally be assumed that the appearance of significant strain fields in the case of neutron irradiation is related to the formation of disordered regions. The strain fields are manifested even at $\Phi \le 10^{16}$ cm^{-2}, when the disordered regions do not overlap [11].

REFERENCES

1. M. D. Sturge, Phys. Rev. **127**, 768 (1962).
2. M. A. Abdulaev, V. T. Agekyan, and R. P. Seĭsyan, Fiz. Tekh. Poluprovodn. (Leningrad) **7**, 2217 (1973) [Sov. Phys. Semicond. **7**, 1476 (1973)].
3. V. I. Safarov, A. N. Titkov, and I. S. Shlimak, Fiz. Tverd. Tela (Leningrad) **12**, 3485 (1970) [Sov. Phys. Solid State **12**, 2831 (1970)].
4. V. L. Alperovich, V. M. Zaletin, A. F. Kravchenko, *et al.*, Phys. Status Solidi B **77**, 465 (1976).
5. Z. V. Jibuti, D. N. Rekhviashvili, and G. L. Eristavi, Soobshch. Akad. Nauk Gruz. SSR **125**, 297 (1987).
6. N. Dolidze, Z. Jibuti, G. Eristavi, *et al.*, Bull. Georgian Acad. Sci. **166** (3), 259 (2002).
7. D. V. Lang, Inst. Phys. Conf. Ser. **31** (1), 70 (1977).
8. *Excitons*, Ed. by E. I. Rashba and M. D. Smurge (North-Holland, Amsterdam, 1982; Nauka, Moscow, 1985).
9. J. I. Pankove, *Optical Processes in Semiconductors* (Prentice-Hall, New Jersey, 1971; Mir, Moscow, 1973).
10. O. Madelung, *Physics of III–V Compounds* (Wiley, New York, 1964; Mir, Moscow, 1967).
11. V. P. Kladko and S. V. Plyatsko, Fiz. Tekh. Poluprovodn. (St. Petersburg) **32**, 261 (1998) [Semiconductors **32**, 235 (1998)].

Translated by P. Pozdeev

Technical Physics Letters, Vol. 29, No. 7, 2003, pp. 542–543. Translated from Pis'ma v Zhurnal Tekhnicheskoĭ Fiziki, Vol. 29, No. 13, 2003, pp. 31–35.

The Influence of Finite End Screens on the Spectrum of Oscillations in Cylindrical Quasioptical Dielectric Resonators

A. A. Barannik, Yu. V. Prokopenko*, Yu. F. Filippov, and N. T. Cherpak**

Usikov Institute of Radiophysics and Electronics, National Academy of Sciences of Ukraine, Kharkov, Ukraine

*e-mail: * prokopen@ire.kharkov.ua; ** cherpak@ire.kharkov.ua*

Received December 16, 2002

Abstract—We have studied the influence of finite dimensions of the end screens on the spectrum of whispering gallery modes in a teflon cylindrical quasioptical resonator. The dependence of the resonance oscillation frequency on the radius of conducting end screens is determined for the first time. Variation of the screen radius leads to transformation of the axial index of HE modes. *© 2003 MAIK "Nauka/Interperiodica".*

The microwave characteristics of materials are frequently determined using cylindrical quasioptical dielectric resonators featuring oscillations of the whispering gallery mode type. Such resonators are simply coupled to both active and passive elements of hybrid schemes in the millimeter and submillimeter wavelength range. However, the spectral characteristics of oscillations in these systems have been calculated only assuming the presence of infinite ideally conducting end planes [1]. Resonators with superconducting films at the ends can be used for the measurement of small surface resistances of superconductors in the millimeter wavelength range [2, 3]. For practice, it would be important to study the effect of finite end screens on the resonance oscillations.

We have experimentally and theoretically studied the pattern of oscillations in a cylindrical resonator with a diameter of $2r_0$ = 78.15 mm and a height of L = 6.84 mm, with 5-mm-thick aluminum disk screens on the ends (Fig. 1). The resonator was made of teflon with ε = 2.04. In the course of our experiments, the disk screen diameter D was varied from 0 to 120 mm. The resonance frequencies were theoretically calculated for two limiting cases: $D = 0$ and $D = \infty$.

A strict theory for the open dielectric resonator ($D = 0$) has not been developed so far. With allowance for the boundary conditions on the side surface of an isotropic cylindrical resonator, the resonance frequencies obey the following characteristic equation [1]:

$$\frac{J_n'(qr_0)}{qr_0 J_n(qr_0)} - \frac{H_n^{(1)'}(q_0r_0)}{q_0r_0H_n^{(1)}(q_0r_0)} = \frac{kk_z n}{q^2q_0^2r_0^2}(1-\varepsilon),$$

where the prime denotes differentiation with respect to the argument; $J_n(qr_0)$ and $H_n^{(1)}(q_0r_0)$ are the cylindrical Bessel and Hankel functions of the first kind; $q = \sqrt{\varepsilon k^2 - k_z^2}$, $q_0 = \sqrt{k^2 - k_z^2}$, k_z is the axial component of the wave vector; and $k = \omega_p/c$, ω_p is the resonance frequency of the pth oscillation (p stands for the triple index nsm, where n, s, and m are the azimuthal, radial, and axial indices, respectively).

The resonance frequencies of the open resonator were previously calculated by methods of a magnetic wall, variation, and partial regions using appropriate approximations of the electromagnetic field distribution outside the resonator and taking into account peculiarities of the field distribution near dielectric edges [4]. We have used an experimental identification of the resonance frequencies with azimuthal and radial indices [5]. The radial and axial components of the wave vector were determined by solving the above transcendental equation. The effective resonator height was defined as $L_{eff} = m\pi/k_z$.

For a resonator with nonideally conducting walls and unbounded end surfaces ($D = \infty$), the resonance fre-

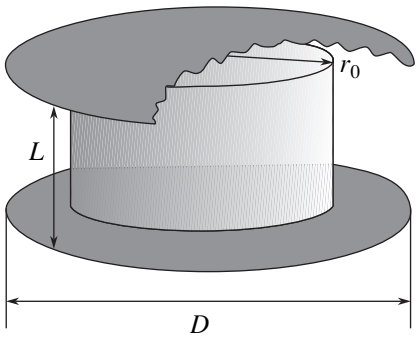

Fig. 1. Schematic diagram of a cylindrical quasioptical dielectric resonator with conducting end screens.

quencies ε are determined by solutions of the characteristic equation

$$\det\left\|(\omega-\omega_p)\delta_{pp'}+i\zeta\frac{I_{pp'}}{W_p}\right\| = 0,$$

describing a shift of the pth oscillation under the action of the nonideally conducting end surfaces [6]. In this equation, $\delta_{pp'}$ is the Kronecker delta, ζ is the surface impedance of the end surface, the term

$$I^2_{pp'}\zeta = \frac{c^2\zeta}{16\pi^2}\int_S[\mathbf{e}_z\times[\mathbf{e}_z\times\mathbf{H}_{p'}]]\mathbf{H}_p dS$$

takes into account losses in the end walls and describes intermode interaction in the resonator (the integration is performed over the end surface S (whose normal coincides with the $\mathbf{e}_z$ unit vector), and the term

$$W_p = \frac{1}{8\pi}\int_V(|\mathbf{H}_p|^2+\varepsilon|\mathbf{E}_p|^2)dV$$

determines the energy of the electromagnetic field generated by the pth oscillation with the electric and magnetic field vectors $\mathbf{E}_p$ and $\mathbf{H}_p$, respectively, in the volume (V) of a resonator with ideally conducting surfaces.

Figure 2 shows the influence of the reduced radius $\gamma = D/2r_0$ on the eigenmode frequencies f in the interval of 36–40 GHz. In this interval, the resonator with $\gamma > 1$ features the following independent modes: EH_{3511}, EH_{3611}, HE_{3810}, and HE_{3910}; the same system with $\gamma < 0.9$ features the EH_{3511}, EH_{3611}, HE_{3811}, and HE_{3911} modes. For $\gamma < 0.77$ and $\gamma > 1.1$, the frequencies of these modes are virtually independent of the end screen diameter. The frequencies of HE_{3810} and HE_{3910} are almost constant for $\gamma > 0.97$.

When the reduced radius is comparable with the resonator radius ($\gamma \approx 1$), the screen can be considered as an axial and radial inhomogeneity. As the screen radius decreases, the influence of this inhomogeneity results in the appearance of partial oscillations with various radial and axial indices. The axially homogeneous modes correspond to a very low Q and have not been detected in experiment (only HE_{3811} and HE_{3911} modes are observed). The axially inhomogeneous mode Q value for the given screen size significantly exceeds that of the axially homogeneous modes.

As the reduced radius decreases ($\gamma \le 0.97$), the frequencies of axially homogeneous modes increase and asymptotically approach the frequencies of the HE_{3811} and HE_{3911} modes in the open resonator. The observed frequency difference between HE modes for the open and screened resonators reaches hundreds and thousands of megahertz. The inhomogeneity greatly influences the EH_{3511} and EH_{3611} modes. The corresponding resonance frequencies decrease with the reduced

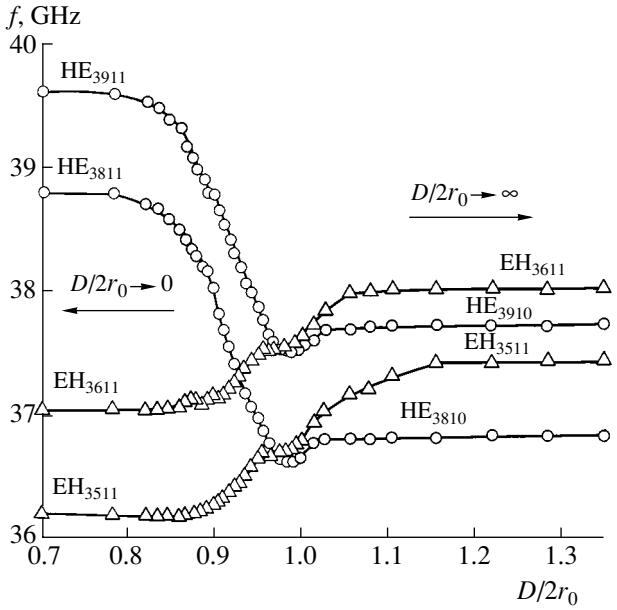

Fig. 2. Plots of the resonance frequencies versus reduced radius for eigenmodes in the 36–40 GHz interval.

radius γ and asymptotically tend to the corresponding resonance values for the open resonator. The frequency shift for the EH modes is twice as small as that for the HE modes.

Thus, the high accuracy of calculation of the spectral characteristics of the resonator under consideration is achieved when the ratio γ of diameters of the end conducting screen and the dielectric cylinder is greater than 1.1. Cylindrical quasioptical dielectric resonators with conducting end screens can be used for determining small surface impedances ζ. Using such devices, it is possible to study the microwave characteristics of high-temperature superconductor films of finite dimensions in the millimeter and, probably, submillimeter wavelength range.

REFERENCES

1. V. N. Egorov and I. N. Mal'tseva, Élektron. Tekh., Ser. Élektron. SVCh, No. 1, 3 (1981).
2. J. Mazierska and C. Wilker, IEEE Trans. Microwave Theory Tech. **11**, 4140 (2001).
3. N. T. Cherpak, A. A. Barannik, Yu. F. Filippov, *et al.*, in *Book of Abstracts of the International Conference "Applied Superconductivity," Houston, 2002*, p. 171.
4. K. N. Tsibizov, E. A. Borisov, and Yu. M. Bezborodov, Zarubezhn. Radioélektron., No. 1, 21 (1981).
5. Yu. F. Filippov and S. N. Khar'kovskiĭ, Izv. Vyssh. Uchebn. Zaved., Radiofiz. **33**, 1304 (1990).
6. Yu. V. Prokopenko and Yu. F. Filippov, Zh. Tekh. Fiz. **72** (6), 79 (2002) [Tech. Phys. **47**, 731 (2002)].

Translated by P. Pozdeev

Technical Physics Letters, Vol. 29, No. 7, 2003, pp. 544–546. Translated from Pis'ma v Zhurnal Tekhnicheskoĭ Fiziki, Vol. 29, No. 13, 2003, pp. 36–42.

The Curie Principle and Diffusion Limited Aggregation

L. M. Martyushev and L. G. Gorbich

Institute of Industrial Ecology, Ural Division, Russian Academy of Sciences, Yekaterinburg, Russia

e-mail: mlm@ecko.uran.ru

Received January 31, 2003

Abstract—The results of modeling snowflake growth by method of diffusion limited aggregation are considered from the standpoint of the Curie principle. Exceptions to this principle are found, related to the essentially nonequilibrium character of the process studied. © *2003 MAIK "Nauka/Interperiodica".*

In the past two decades, much attention has been paid to computer simulation of irreversible processes using diffusion limited aggregation (DLA) models (see, e.g., reviews [1–3]). Numerous modifications of the classical Witten–Sunder algorithm have been developed so as to take into account the surface tension, anisotropy, and other factors. In addition to the large applied value for electrochemistry, colloid chemistry, surface crystallization physics, etc., these models are of considerable basic interest. The main theoretical considerations and numerical simulations have been devoted to the fractal character of clusters, the scaling effects in growth processes, and the dependence of these properties and the symmetry of nonequilibrium structures on the symmetry of the medium (lattice) used in the calculations.

This brief communication touches upon one point not given proper attention previously. We will consider the results of DLA simulation from the standpoint of the Curie principle [4–6].

In application to the problems under consideration, the Curie principle can be formulated as follows: the symmetry of a parent medium is imposed onto the symmetry of a body formed in this medium. As a result, the shape of the body retains only those elements of the intrinsic symmetry which coincide with the imposed symmetry elements. In other words, the symmetry group of this body is a common symmetry subgroup of all interactions manifested in this body. This principle is considered one of the most important and general laws in physics [4–6].

Figure 1 shows the results of our two-dimensional snowflake growth simulation using a standard two-parametric variant of the DLA model. The particles start from a randomly selected point on a circle circumscribed about the lattice and move along random broken lines with equal segment length L. In order to decrease the stochastic action of separate particles (a homogeneous diffusion field is sufficient for simulation purposes), a certain critical averaging threshold H (the number of particles falling within a given boundary cell) is introduced such that, upon attaining this limit, the cell is considered as belonging to the crystal. As a result, the aggregate growth proceeds only via the cells most frequently visited by the "diffusing" particles. At the initial time, the crystal contains a single cell at the center of the lattice (coinciding with the center of the initial circle).

Our simulations were performed on a hexagonal lattice, which provides for the modeling of structures possessing a symmetry of the $L_6 6P$ type. Selecting this symmetry is not of principal importance for the problem under consideration and is explained by a relatively small number of data for the DLA simulation on such lattices (the experiments have mostly been performed on $L_4 4P$ lattices) and by the importance of such calculations from the standpoint of snowflake formation in the Earth's atmosphere. As can be seen from Fig. 1, parameter L is responsible for the structure porosity (the greater L, the higher the crystal structure density),

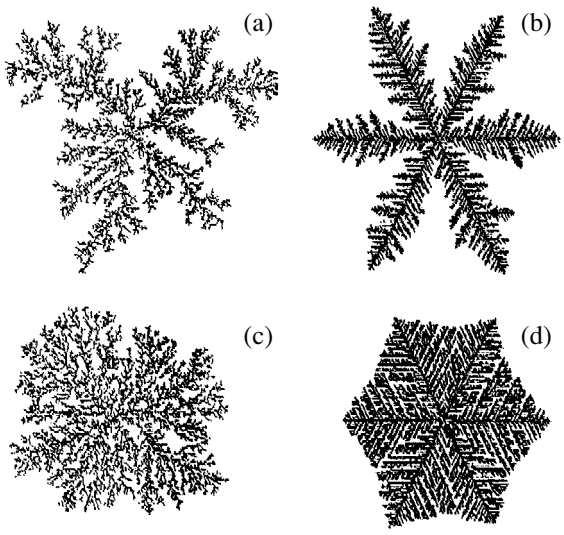

Fig. 1. Snowflake structures simulated using a DLA model on a 301 × 347 lattice (each cluster contains 10000 particles) for various L and H values: (a) L = 10, H = 1; (b) L = 10, H = 50; (c) L = 500, H = 1; (d) L = 500, H = 50.

1063-7850/03/2907-0544$24.00

while parameter H determines the symmetry of the growing structure (increasing H implies increasing influence of the lattice on which the simulation is performed).

Let us analyze the results from the standpoint of the Curie principle. The diffusion field possesses $L_\infty\infty P$ symmetry (see, e.g., Fig. 2), while the model lattice (responsible for the symmetry of the growing crystal structure) possesses $L_6 6P$ symmetry. Therefore, the growing structure must possess either $L_6 6P$ symmetry or (if the model parameters are selected so that the lattice symmetry is suppressed) by the symmetry of the diffusion field. These conclusions are confirmed by the results presented in Fig. 1. Note that the symmetry of clusters presented in Figs. 1a and 1c can be considered only in a statistical sense (this is especially true for the classical Witten–Sunder aggregate depicted in Fig. 1a).

Variation of the parameters of the model under consideration revealed an interesting behavior in the region of small L and $H \approx 50$. The structures corresponding to this region of parameters (Fig. 3) are obviously asymmetric (at least, they do not possess $L_6 6P$ or $L_\infty\infty P$ symmetry). According to the above considerations, this means that these structures do not obey the Curie principle. Let us consider this situation in more detail.

First, note that analogous discrepancies have been previously encountered in other modifications of the DLA model, but these results were not given proper attention [7]. This fact, together with numerous checks and additional calculations performed in the present study, exclude the possibility of programming errors in the course of simulation. Second, one might suggest that the modeling procedure, should it be further continued, will provide for attaining the cluster symmetry according to the Curie principle. However, this hypothesis has to be checked separately and, even if it were true, the situation is not principally changed: we are modeling a certain physical process that can in fact stop at any stage (Fig. 3) rather than proceed infinitely.

The asymmetry can be even more clearly pronounced in the following modification of the model: let parameter H be set to zero for all cells when some particle is added to the cluster (so that all boundary cells of the growing cluster become equal after each addition). One can readily find a real physical aggregation process corresponding to this model. The result of such a process is presented in Fig. 4 (the direction of aggregation may change in each subsequent experiment and is generally arbitrary). Apparently, the asymmetry of this cluster will even increase with time.

The most serious objection is that the Curie principle, like any other phenomenological law, is macroscopic and does not apply to the "microscopic" level of DLA simulation. Indeed, consider a medium featuring a manifold of randomly oriented structures of the type depicted in Figs. 3 and 4. Then, the overall statistical symmetry of the system will coincide with that of the diffusion field. However, despite a certain doubt con-

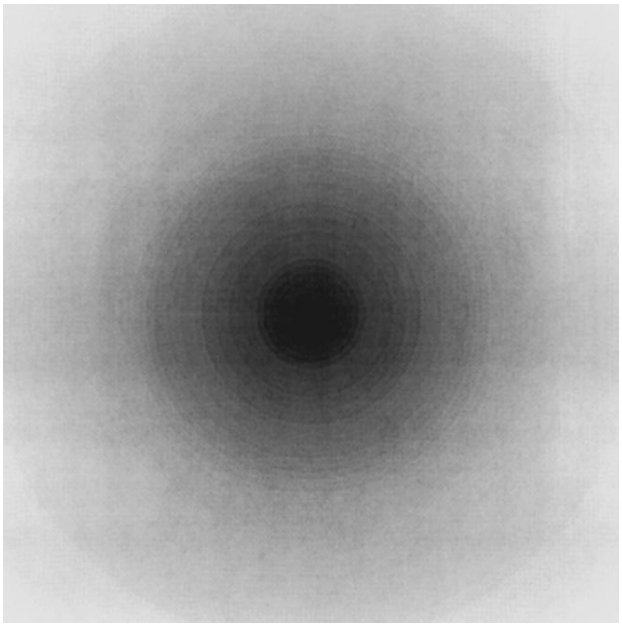

Fig. 2. A diffusion field of the DLA model determined for a multiply repeated start of a particle from a random point at the system boundary (circumscribed circle). The lighter the region, the more frequently it is visited by the particle (the greater the final concentration of particles). The brightest areas correspond to 80000 visits, and the black areas, to 25000 visits (301×347 lattice; $L = 2$).

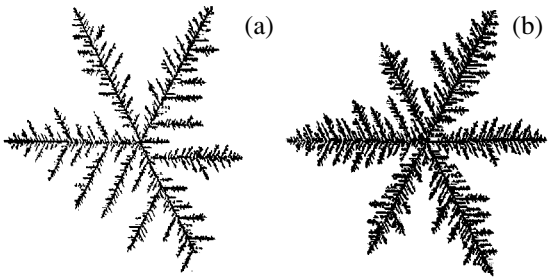

Fig. 3. Asymmetric structures obtained using a DLA model with (a) $L = 2$, $H = 50$ and (b) $L = 7$, $H = 50$.

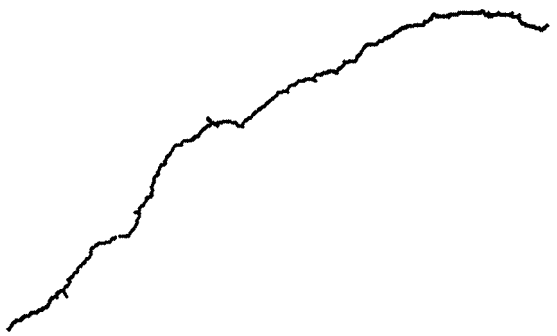

Fig. 4. A threadlike structure obtained using a modified DLA model with periodic "reset" of H ($L = 10$, $H = 50$).

cerning the possibility of interpreting DLA as a macroscopic simulation model equivalent to solving phenomenological equations [8], most researchers believe that the results of such modeling apply on both the atomic and macroscopic scale [1–3, 7, 9].

Thus, the results of our simulations either provide support to opponents of using DLA as a means of simulating physical processes in an arbitrary spatial scale or give evidence that there are exceptions to the Curie principle. The authors are rather inclined to the latter opinion, the more so that nature also gives examples of such exceptions. Indeed, the Earth's atmosphere shows the formation of snowflakes possessing both irregular shapes [10, 11] and three-arm configurations [7, 10, 11].

To summarize, any principle has a domain of applicability. The results of our investigation suggest two restrictions on the Curie principle. First, this is obviously a macroscopic principle. Second, this principle is valid for equilibrium processes and only partly applies to nonequilibrium ones. This is a classical principle of "equilibrium" physics. The more nonequilibrium a given process, the more significant the influence of each particular fluctuation and, hence, the more probable the exceptions to the Curie principle. The latter limitation is confirmed by the results of our DLA simulations. This method is traditionally employed for studying nonequilibrium and strongly nonequilibrium processes of structure formation.

REFERENCES

1. R. Jullien, Usp. Fiz. Nauk **157**, 339 (1989); Comments Condens. Matter Phys. B **13**, 177 (1987).
2. B. M. Smirnov, *Physics of Fractal Clusters* (Nauka, Moscow, 1991).
3. T. Vicsek, *Fractal Growth Phenomena* (World Scientific, Singapore, 1992).
4. P. Curie, *Selected Papers* (Nauka, Moscow, 1966), p. 95.
5. A. V. Shubnikov, Usp. Fiz. Nauk **59**, 591 (1956).
6. I. I. Shafranovskiĭ, *Symmetry in Nature* (Nedra, Leningrad, 1985).
7. J. Nittmann and H. E. Stanley, J. Phys. A **20**, L1185 (1987).
8. B. K. Johnson and R. F. Sekerka, Phys. Rev. E **52**, 6404 (1995).
9. R. Xiao, J. I. D. Alexander, and F. Rosenberger, Phys. Rev. A **38**, 2447 (1988).
10. A. D. Zamorskiĭ, *Atmospheric Ice* (Izd. Akad. Nauk SSSR, Moscow, 1955).
11. C. Magono and C. W. Lee, J. Fac. Sci. **2**, 321 (1966).

Translated by P. Pozdeev

Technical Physics Letters, Vol. 29, No. 7, 2003, pp. 547–549. Translated from Pis'ma v Zhurnal Tekhnicheskoĭ Fiziki, Vol. 29, No. 13, 2003, pp. 43–49.

The Effect of a Precursor on the Magnetostatic and Dynamic Characteristics of $Co_{68}Fe_4Cr_4Si_{12}B_{12}$ Amorphous Ribbons

E. E. Shalyguina[a,*], N. M. Abrosimova[a], M. A. Komarova[a], V. V. Molokanov[a], Ch. O. Kim[b], Ch. G. Kim[b], and Y. W. Rheem[b]

[a] *Moscow State University, Moscow, 119899 Russia*

** e-mail: shal@magn.ru*

[b] *Korea National University, Taejon, Korea*

Received January 28, 2003

Abstract—We have studied the influence of a precursor on the magnetostatic and dynamic characteristics of $Co_{68}Fe_4Cr_4Si_{12}B_{12}$ amorphous alloy ribbons. It is established that a rational choice of the precursor provides for a significant increase in the properties of soft magnetic ribbons and noticeably increases the magnetoimpedance. *© 2003 MAIK "Nauka/Interperiodica".*

Although amorphous magnetic materials were discovered more than three decades ago, the interest in studying the structure and the magnetic, kinetic, and dynamic properties of these materials is still great. This is primarily due to the considerable potential of using amorphous magnets in modern microelectronics, at a relatively low cost of production.

In recent years, much attention has been given to increasing the glass-forming ability of amorphous alloys, which is aimed at increasing the magnetic and mechanical characteristics, corrosion resistance, and other structure-dependent properties of these materials. As is known, the number of possible compositions possessing extremely high glass-forming ability is rather small, which is explained by the small number of eutectics for the glass-forming compounds.

It was proved [1, 2] that the glass-forming ability of amorphous alloys can be achieved by selecting the seeding material (precursor) and a proper thermal treatment of the melt. The main requirement on the precursor structure is the absence of rough separated primary phases necessitating a high overheating of the melt to provide for their complete dissolution. The clusters of primary phases acting as the crystallization centers hinder supercooling and glass formation. It was shown [3] that a significant increase in the glass-forming ability of amorphous alloys can be achieved by using as a precursor a soft magnet powder possessing an amorphous structure. A special additional thermal treatment of the melt can also increase the glass-forming ability of a given amorphous alloy [2]. Obviously, this modification of the technology of amorphous ally ribbons must influence the physical properties of the final material.

It is known that the practical application of amorphous alloys is determined by their characteristics, such as magnetoresistance and magnetoimpedance. As demonstrated in [4, 5], these characteristics depend on the micromagnetic structure (i.e., on the equilibrium distribution of magnetization) of a material. For this reason, the micromagnetic structure of amorphous alloys fabricated in the form of wires and ribbons has been extensively studied.

In this Letter, we report on the original results concerning the influence of the technology of production of $Co_{68}Fe_4Cr_4Si_{12}B_{12}$ amorphous alloy ribbons on the surface micromagnetic structure, magnetic properties, and dynamic characteristics of the material.

An initial $Co_{68}Fe_4Cr_4Si_{12}B_{12}$ amorphous alloy ribbon (sample 1) with a thickness of 20 μm was prepared by rapid solidification technique in air, using the melt of an ingot of this composition. Another ribbon of the same composition (sample 2) was obtained by rapid solidification technique in a He atmosphere, proceeding from the melt of a sample of the first ribbon after a special thermal treatment. The X-ray diffraction measurements confirmed that both ribbons were amorphous. The magnetostriction saturation constant λ_s for both ribbons was on the order of 1×10^{-7}.

The surface magnetic properties of the samples of amorphous ribbons were studied on a magnetooptical micromagnetometer described in detail elsewhere [6]. The ribbons were cut to pieces of length 20 mm. The alternating magnetic field with a frequency of $f = 80$ Hz was applied parallel to the sample surface. The sample surface was scanned with a 20-μm-diam light spot over the length L and the profiles of the in-plane magnetization components, the local magnetization curves, and

1063-7850/03/2907-0547$24.00 © 2003 MAIK "Nauka/Interperiodica"

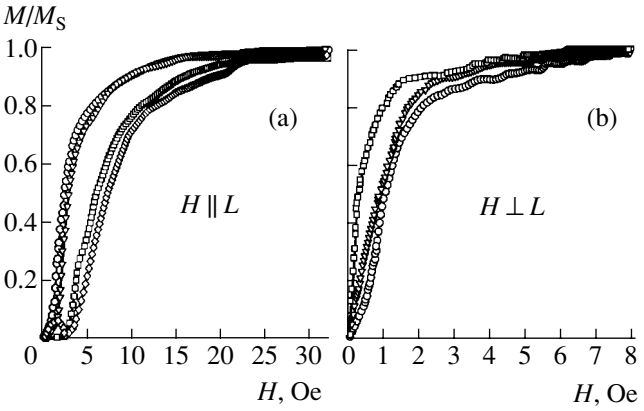

Fig. 1. Typical local magnetization curves measured on the contact side of ribbon 1 with a planar magnetic field applied (a) parallel and (b) perpendicular to the sample length L.

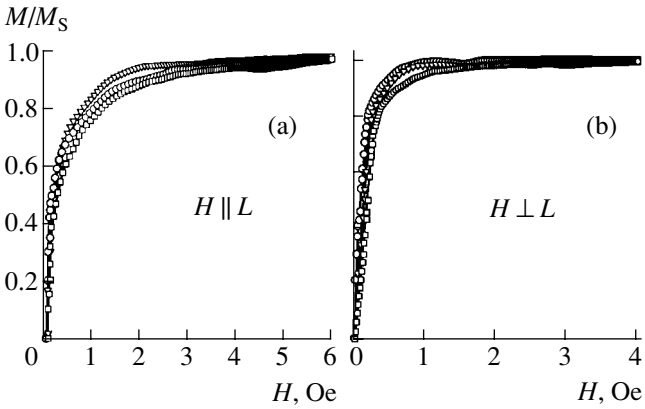

Fig. 2. Typical local magnetization curves measured on the contact side of ribbon 2 with a planar magnetic field applied (a) parallel and (b) perpendicular to the sample length L.

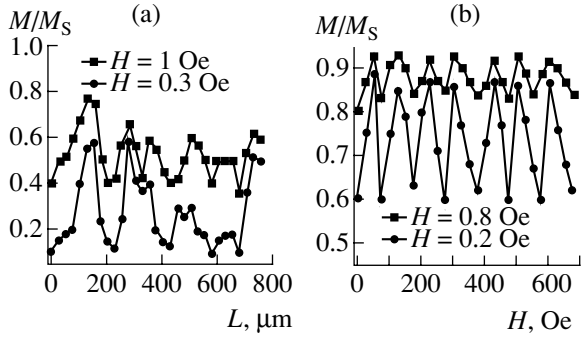

Fig. 3. Typical profiles of the in-plane magnetization component parallel to the magnetic field applied along the sample length L in the ribbons of (a) type 1 and (b) type 2 (measured by scanning the samples with a 20-μm-diam light spot along the central line of the contact side of the ribbon).

the hysteresis loops were obtained by measuring the equatorial Kerr effect δ. The results represented essentially the ratios $\delta(L, H)/\delta_S \propto M(L, H)/M_S$, where $\delta = (I - I_0)/I_0$; I and I_0 are the intensities of light reflected from the magnetized and nonmagnetized sample, respectively; δ_S is the equatorial Kerr effect at $M = M_S$; and M_S is the saturation magnetization of the sample studied. It should be noted that the length L is measured in the direction coinciding with that of the ribbon growth bands.

The magnetoimpedance Z was studied as a function of the external magnetic field applied in the direction of L parallel to the ac probing current $i_\sim = 5$ mA. The measurements were performed using a four-point-probe system of the HP 4192A type. The cyclic magnetic field was generated by Helmholtz coils. The magnetic field dependence of the magnetoimpedance ratio $\Delta Z/Z(\%) = \{Z(H) - Z_{sat}\}/Z_{sat} \times 100\%$ (Z_{sat} is the magnetoimpedance at $H = 36$ Oe) were measured for various frequencies of the probing current in the course of a cyclic variation of the applied field (from $+H$ to $-H$ and back).

The results of magnetooptical determination of the magnetic characteristics averaged over the sample surface showed that our ribbons possessed a planar magnetic anisotropy with the easy axis perpendicular to the ribbon length L, which is typical of magnetic materials with negative magnetostriction.

Figures 1 and 2 present typical local magnetization curves measured for ribbons of the two types with the external magnetic field applied parallel and perpendicular to the sample length L. As can be seen from these data, the local magnetization curves differ significantly for sample 1, while being almost identical for sample 2. These results are indicative of the difference in the degree of homogeneity of the local magnetic properties of the amorphous ribbons of the two types studied. The pronounced inhomogeneity of the local magnetic characteristics in sample 1 can be attributed to strong dispersion of the magnetic anisotropy—a phenomenon typical of magnetic materials obtained by the traditional rapid solidification technique technology [7–10]. The high homogeneity of the local magnetic characteristics observed in sample 2 can be explained by increased glass-forming ability of the melt, which was achieved via a rational selection of the precursor and a special thermal pretreatment of the melt. It should be noted that, despite the significant difference between the local magnetization curves of sample 1, the transverse orientation of the easy axis (perpendicular to the sample length L) is still clearly pronounced. An analysis of the experimental data showed that both the coercive force H_C and the saturation field H_S of sample 2 are about one-tenth of the corresponding values for sample 1.

Figure 3 shows typical profiles of the in-plane magnetization component parallel to the magnetic field applied along the sample length L in the ribbons of types 1 and 2. As can be seen, strong dispersion of the magnetic anisotropy in the former case and high homogeneity of the magnetic characteristics in the latter case account for an irregular and a periodic distribution of magnetization observed in samples 1 and 2, respec-

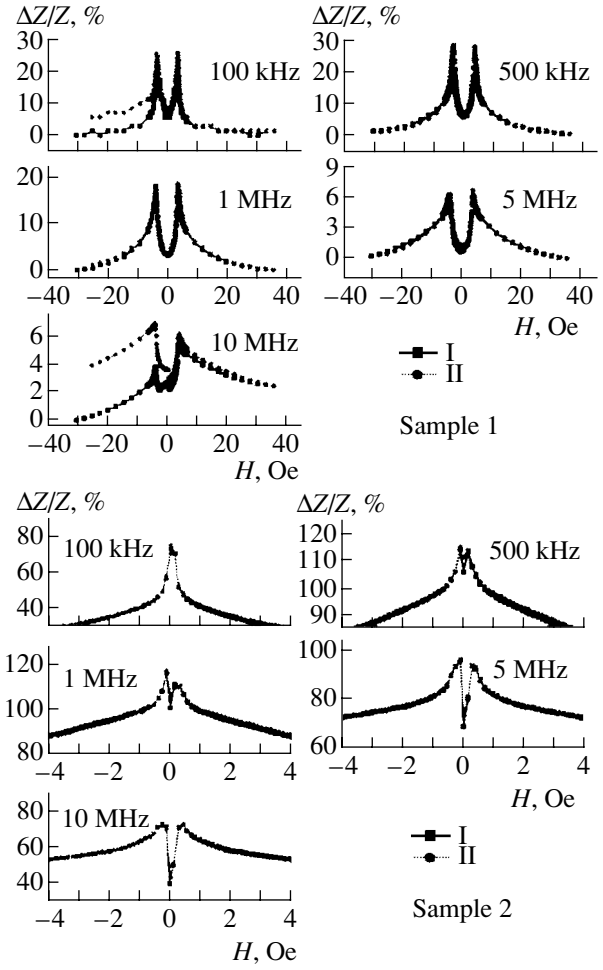

Fig. 4. Typical plots of the magnetoimpedance $\Delta Z/Z$ versus magnetic field strength H measured at various frequencies for samples 1 and 2. Curves I and II were measured with the magnetic field strength increased from $-H$ to $+H$ and decreased from $+H$ to $-H$, respectively.

tively. Using these data, it is possible to determine the characteristic size W of magnetic inhomogeneities in the sample studied. The W value is usually estimated as the distance between maxima (or minima) on the magnetization profiles. As can be seen, $W \sim 150$–200 μm for the sample of ribbon 1, while in ribbon 2 the W value does not exceed 100 μm.

The difference in the surface micromagnetic structure observed in the amorphous ribbons studied leads to dissimilar field and frequency dependences of the magnetoimpedance $\Delta Z/Z$ (Fig. 4). As can be seen from the data in Fig. 4, the magnetic field dependences exhibit two peaks. The general shape of the curves does not change with frequency, but the maximum values of these peaks are observed at different frequencies. A comparison of Figs. 1, 2, and 4 reveals that the $\Delta Z/Z$ peaks are observed for nearly the same fields as those corresponding to the magnetization reversal along the easy axis. This implies that the positions of the $\Delta Z/Z$ peaks reflect the magnetic softness of the sample studied. These data indicate that the main physical factor accounting for the magnetoimpedance is the magnetization reversal process. The maximum values of $\Delta Z/Z$ for samples 1 and 2 are 25 and 120%, respectively. The increase of magnetoimpedance in the latter case can be explained by a significant increase in homogeneity of the local magnetic properties of the material. This experimental fact agrees well with the theoretical results [11], according to which a higher dispersion of the magnetic anisotropy in amorphous magnets must be accompanied by a decrease in the magnetoimpedance.

To summarize, the results of our investigation showed that a significant increase in the soft magnet characteristics and magnetoimpedance of amorphous ribbons can be achieved via a rational choice of the precursor and a special thermal pretreatment of the melt.

Acknowledgments. This study was supported by the Russian Foundation for Basic Research (project nos. 02-02-16627 and 01-03-32986) and by the Institute of Policy, Development, and Planning in Science and Technology through RECAMM at Chungnam National University in Korea.

REFERENCES

1. V. Manov, E. Brook-Levinson, V. V. Molokanov, M. I. Petrzhik, and T. N. Mikhailova, in *Proceedings of Symposium of Materials Research Society, 1999*, Vol. 554, pp. 81–86.
2. V. V. Molokanov, M. I. Petrzhik, T. N. Mikhailova, *et al.*, Metally, No. 6, 100 (1999).
3. V. I. Kalita, D. I. Komlev, and V. V. Molokanov, Fiz. Khim. Obrab. Mater., No. 1, 118 (1997).
4. L. V. Panina and K. Mohri, J. Magn. Magn. Mater. **157–158**, 137 (1996).
5. F. L. A. Machado, C. S. Martins, and S. M. Rezende, Phys. Rev. B **51**, 3926 (1995).
6. E. E. Shalyguina, K. H. Shin, and N. M. Abrosimova, J. Magn. Magn. Mater. **239**, 252 (2002).
7. P. Vavassori, L. Callegaro, E. Puppin, *et al.*, J. Magn. Magn. Mater. **157–158**, 171 (1996).
8. E. E. Shalyguina, N. I. Tsidaeva, and L. M. Bekoeva, J. Phys. IV (France) **8**, Pr2-155 (1998).
9. E. E. Shalyguina, N. I. Tsidaeva, and L. M. Bekoeva, Sens. Actuat. **81**, 216 (2000).
10. E. E. Shalyguina, L. M. Bekoeva, and K. H. Shin, J. Magn. Magn. Mater. **215–216**, 472 (2000).
11. L. V. Panina, K. Mohri, T. Uchiyama, and M. Noda, IEEE Trans. Magn. **31**, 1249 (1994).

Translated by P. Pozdeev

Technical Physics Letters, Vol. 29, No. 7, 2003, pp. 550–553. Translated from Pis'ma v Zhurnal Tekhnicheskoĭ Fiziki, Vol. 29, No. 13, 2003, pp. 50–56.

A New Type of Attractor in Autonomous Systems

V. S. Anishchenko* and M. V. Loginova**

Nonlinear Dynamics Laboratory, Saratov State University, Saratov, Russia

*e-mail: * wadim@chaos.ssu.runnet.ru; ** masha@chaos.ssu.runnet.ru*

Received November 10, 2002; in final form, January 6, 2003

Abstract—We have studied the dynamic regimes of an autonomous chaotic system (a modified oscillator with inertial nonlinearity) and found a chaotic attractor of a new type. The autocorrelation function, power spectrum, and Lyapunov exponents of this attractor have been calculated. Some of these characteristics resemble the behavior of a strange nonchaotic attractor. © *2003 MAIK "Nauka/Interperiodica".*

This investigation was inspired by the communication of Belykh [1] in which it was ascertained that a dynamical system with a saddle separatrix loop can feature the appearance of an attracting hyperbolic subset, that is, of an attractor of the hyperbolic type. In the Poincaré section, this attractor possesses the structure of the Plykin attractor [2]. This is a very interesting result, since hyperbolic attractors (including the Plykin attractor) have never been experimentally observed in real differential systems.

Previously [3], a three-dimensional autonomous dynamical system was introduced in which a saddle–focus separatrix loop and the transition to a saddle separatrix loop regime can be realized depending on the system parameters. It was interesting to check for the prediction [1] and to attempt to find a hyperbolic chaos regime in this system by methods of numerical modeling. While not yet succeeding in finding a hyperbolic attractor, we have established the existence of a nonregular attractor of a new type. To our knowledge, attractors of this type have never been reported for autonomous three-dimensional systems. In this Letter, we describe the properties of the new type of attractors.

The classification of attractors is not only important from the standpoint of the basic concept of deterministic chaos, but it has a direct applied significance as well. In analysis of chaotic signals in experiment, it is very important to know the statistical characteristics of the attractors of various types. The lack of this knowledge markedly complicates diagnostics of the system behavior.

The system under consideration is described by the following set of equations [3, 4]:

$$\begin{aligned} \dot{x} &= mx + y - xz - dx^3, \\ \dot{y} &= -x + \gamma, \\ \dot{z} &= -gz + gI(x)x^2. \end{aligned} \tag{1}$$

The presence of a dissipative term (dx^3) in the right-hand part of the first equation does not allow the trajectory to go to infinity at large values of m. This is related to the condition of negative divergence of the vector field (1), which has the following form [3]:

$$m - g < z + 3dx^2.$$

For small values of m, the parameter d is usually ignored; however, in our case this quantity has to be taken into account.

System (1) has been studied by numerical methods for $d = 0.0001$, $\gamma = 0.05$ and the parameters m and g varied in the intervals $2 < m < 2.5$ and $0.1 < g < 0.14$. This was accompanied by alternation of the regions featuring regular and chaotic regimes. Figure 1a shows the typical form of the chaotic attractor observed for $g = 0.125$ and $m = 2.100$. The numerical calculation was performed using the Runge–Kutta scheme with a variable step and a preset accuracy ($\epsilon = 10^{-10}$). Under these conditions, the integration step did not exceed $\Delta t \approx 10^{-4}$. Taking this into account, the subsequent calculations were performed using schemes with a fixed step of $\Delta t = 10^{-4}$.

However, this is not the only type of a chaotic attractor possible in the system studied. We have found a new attractor with the phase portrait presented in Fig. 1b (for $g = 0.125$ and $m = 2.105$). This attractor exists in a very narrow interval of parameters (approximately for m from 2.1048 to 2.1052). Even visual examination reveals certain differences in the structure of two chaotic attractors. However, in order to have a deeper notion about these regimes, it is necessary to study some quantitative characteristics.

Figures 1c and 1d show the model maps of both attractors for a fixed g ($g = 0.125$) and different m ($m = 2.100$ and 2.105). The Poincaré section was performed with the plane $x = 0$. The implication map for $m = 2.100$ (Fig. 1c) has a maximum in the form of a quadratic parabola. The presence of a smooth maximum is evidence that the system features a smooth contact of stable and unstable manifolds, which results in the appear-

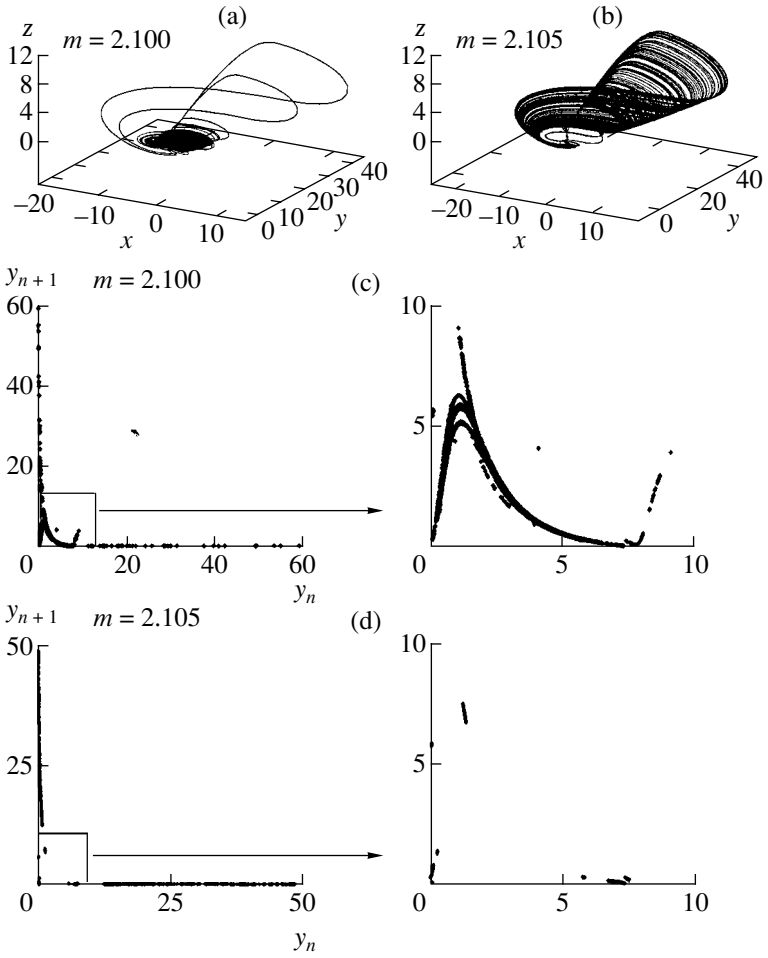

Fig. 1. Attractors of system (1) for $g = 0.125$ and $m = 2.100$ (a, c) and 2.105 (b, d): (a, b) phase portraits; (c, d) implication maps.

ance of stable cycles. Therefore, we deal with a nonhyperbolic chaos regime. The implication map for $m = 2.105$ (Fig. 1d) substantially differs from the preceding one. As can be seen, there is no quadratic maximum and no smooth contact of manifolds, which suggests that an attractor of some other type does exist.

Here, a question arises as to whether this attractor is chaotic or is merely a cycle with a very large period (which is typical of nonhyperbolic regimes). In order to elucidate this point, it is necessary to calculate the Lyapunov characteristic exponent in both cases. We have performed these calculations and obtained the following results:

m	λ_1	λ_2	λ_3
2.100	0.052435	0.000020101	−0.21692
2.105	0.0058609	−0.0000084835	−0.72996
2.1065	0.00019758	−0.012658	−1.3897

A comparison of these data shows that the high-order Lyapunov exponents differ by almost one order of magnitude. In the case of $m = 2.105$, the maximum Lyapunov characteristic exponent is very small (but still nonzero). For comparison, we have also calculated the Lyapunov exponents for a regular regime observed at $m = 2.1065$. As can be seen, the characteristic index is zero to within the fourth decimal digit. Therefore, despite the fact that the maximum characteristic index for $m = 2.105$ is rather small, we can still consider this regime as chaotic.

Thus, we have established that the new regime is characterized by a relatively small value of the high-order Lyapunov exponent and by the absence of a quadratic maximum in the implication map.

Then we calculated the autocorrelation function (ACF) and the power spectrum. The results of these calculations are presented in Fig. 2. As can be seen from Fig. 2a, the ACF for $m = 2.100$ has the form characteristic of a nonhyperbolic chaotic attractor (i.e., exhibits a relatively fast decay with increasing τ). A quite different behavior is observed for the new attractor (Figs. 2b and 2c). Here, the ACF does not decay to zero even for sufficiently large times. Moreover, it is seen that the

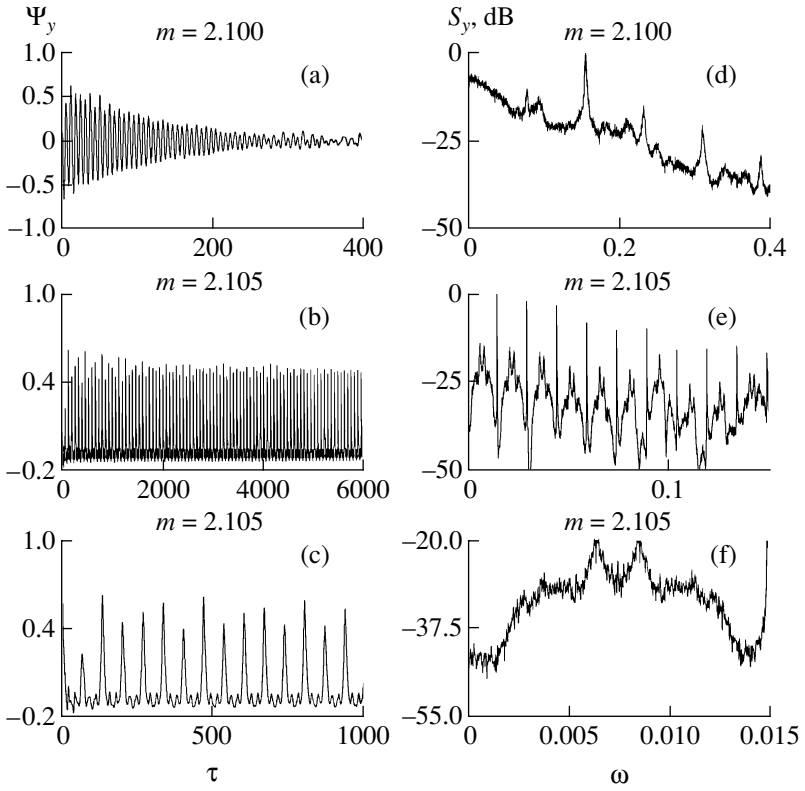

Fig. 2. The characteristics of attractors of system (1) for $g = 0.125$, $m = 2.100$ (a, d) and 2.105 (b, c, e, f): (a, b) autocorrelation functions; (d, e) power spectra (for variable y); (c, f) fragments of the autocorrelation function and power spectrum for $g = 0.125$, $m = 2.105$ on a greater scale.

ACF attains a certain constant level at large τ, which is typical of strange nonchaotic attractors [5, 6].

Figures 2d–2f show the power spectra relative to variable y for both attractors. In the case of $m = 2.100$, the spectrum is continuous with peaks at certain characteristic frequencies. This spectrum is typical of nonhyperbolic attractors. A different pattern is observed for $m = 2.105$. Here, the spectrum is sharply irregular (resembling a singular-continuous spectrum [6]) and its maximum is shifted toward lower frequencies. Note that the region of the spectrum depicted in Fig. 2f is repeated in the adjacent interval [0.015; 0.03]. This behavior also resembles that of a strange nonchaotic attractor.

For comparison, we have calculated the power spectrum for a stable periodic solution (existing close to the attractor under consideration). It was found that some peaks of this spectrum coincide with those in the spectrum of the chaotic attractor at $m = 2.105$. This coincidence can be explained in two ways: (i) the cycle has became unstable but the trajectory still moves in the vicinity of this cycle or (ii) the cycle is stable and we observe the coexistence of two regimes, chaotic and regular, related to the integration uncertainty. The results of calculations performed with a higher precision ($\epsilon = 10^{-10}$) confirmed the first explanation. Upon passage to the new attractor, a periodic regime becomes unstable (with the multiplicator exiting the unit circle). However, because of the finite (albeit high) precision of the calculation, we still cannot exclude the existence of yet another stable cycle and an intermittency of the cycle–chaos type related to the calculation errors.

Conclusions. A shift of the singular point of the system and introduction of an additional dissipative nonlinear term into the ordinary differential equations of a modified oscillator with inertial nonlinearity leads to the appearance of a new chaotic regime in the system. This regime possesses some properties close to those of a strange nonchaotic attractor: (i) the high-order Lyapunov exponent is very small (but is not zero, as for a strange nonchaotic attractor); (ii) the autocorrelation function decreases to a certain nonzero level and then ceases to decay; (iii) the power spectrum is sharply irregular, resembling a singular-continuous spectrum.

Strange nonchaotic attractors have never been observed in autonomous systems and were reported only for systems with quasiperiodic excitation [5–7].

The new type of attractor described above combines the properties of a usual chaotic attractor (positive Lyapunov exponent, continuous spectrum, splitting of correlations) and those resembling a strange nonchaotic attractor (positive Lyapunov exponent close to zero, the autocorrelation function decreases to zero with time,

the power spectrum resembles a singular-continuous spectrum).

Acknowledgments. This study was supported by the US Civilian Research and Development Foundation for the Independent States of the Former Soviet Union (CRDF Award No. REC-006).

REFERENCES

1. V. N. Belykh, in *Proceedings of the International Conference on Differential Equations and Dynamical Systems, Suzdal, 2000*, pp. 13–15.
2. R. V. Plykin, Usp. Mat. Nauk **35** (3), 94 (1980).
3. V. S. Anishchenko, *Stochastic Oscillations in Radiophysical Systems* (Saratov. Gos. Univ., Saratov, 1986).
4. V. S. Anishchenko, *Complex Oscillations in Simple Systems* (Nauka, Moscow, 2000).
5. C. Grebogi, E. Ott, S. Pelikan, and J. A. Yorke, Physica D **13**, 261 (1984).
6. A. S. Pikovsky and U. Feudel, J. Phys. A **27**, 5209 (1994).
7. V. S. Anishchenko, T. E. Vadivasova, and O. Sosnovtseva, Phys. Rev. E **54**, 3231 (1996).

Translated by P. Pozdeev

Technical Physics Letters, Vol. 29, No. 7, 2003, pp. 554–556. Translated from Pis'ma v Zhurnal Tekhnicheskoĭ Fiziki, Vol. 29, No. 13, 2003, pp. 57–63.

Interaction of a CO_2 Laser Beam with Free-Falling Liquid Drops during Modification of Dissolved Biomolecules

G. A. Baranov, A. A. Belyaev, S. B. Onikienko, S. A. Smirnov, and V. V. Khukharev

Efremov Institute of Electrophysical Equipment, St. Petersburg, Russia
e-mail: laser@mail.rcom.ru
State Military-Medical Academy, St. Petersburg, Russia

Received January 21, 2003

Abstract—Nonstationary processes involved in the interaction of a CO_2 laser beam with a free-falling drop of water were numerically simulated by calculating the gasdynamic streamlining of the drop by air, the temperature field in the drop, and the two-phase transformations on the liquid surface. Validity of the model and the results of calculations were checked in experiment. The study was aimed at explaining the effects related to degradation of large polysaccharide molecules in a drops of aqueous solution under the action of laser radiation.

Previously [1], we reported the results of a theoretical and experimental investigation of the process leading to degradation of polysaccharide molecules in a drop of aqueous solution under the action of laser radiation. It was demonstrated that absorption of the laser radiation at the liquid surface is accompanied by the generation of waves in water, in which the medium strain rate [2] is sufficiently high to produce significant deformation of amylopectin molecules [3]. The most probable hydrodynamic effect responsible for the degradation of large polysaccharide molecules with the formation of molecular fragments (highly effective in the immunology of infectious and oncological disorders) was determined [4].

This work is a continuation of the investigation reported in [1]. In addition to calculating the temperature field in a free-falling liquid drop exposed to laser radiation, we have numerically simulated the motion of a gaseous mixture (air with water molecules evaporated from the liquid surface) surrounding the drop. The evaporation rate was determined using the Hertz–Knudsen formula [5]. The results of numerical modeling, performed in addition to experiments on determining the velocity of repulsion of the drop from the laser beam, allowed us to estimate the condensation coefficient. This quantity influences both the evaporation rate and the temperature field in the drop and, hence, the onset of laser-induced explosion boiling in the surface layer of the liquid. Based on the analysis of these results, we explain termination of the laser-induced degradation of a polysaccharide (amylopectin), which is observed when the laser beam power exceeds a certain threshold.

Description of model. The motion of a gaseous mixture surrounding the drop was calculated using a system of nonstationary Navier–Stokes equations describing the mass and heat transfer in the system:

$$\rho\frac{\partial \mathbf{V}}{\partial t} + \rho(\bar{\mathbf{V}}\nabla)\bar{\mathbf{V}} = \rho\mathbf{g} - \nabla p + \nabla\mu(\nabla\mathbf{V}), \quad (1)$$

$$\frac{\partial \rho}{\partial t} + \nabla(\rho\mathbf{V}) = 0, \quad (2)$$

$$c_p\rho\frac{\partial T}{\partial t} + c_p\rho\bar{\mathbf{V}}(\nabla T) = \nabla\lambda(\nabla T), \quad (3)$$

$$\frac{\partial c_i}{\partial t} + \bar{\mathbf{V}}(\nabla c_i) = \nabla D_i(\nabla c_i), \quad (4)$$

$$p = \rho RT\sum_{i=1}^{N_k}\frac{c_i}{m_i}. \quad (5)$$

Here, T, p, and ρ are the temperature, pressure, and density of the gas phase, respectively; $\bar{\mathbf{V}}$ is the velocity vector; μ is the liquid viscosity; R is the universal gas constant; N_i is the number of components in the gaseous mixture; m_i and c_i are the molecular weight and the mass fraction of the ith component in the gaseous mixture; λ is the thermal conductivity; c_p is the heat capacity, and D_i is the coefficient of diffusion of the ith component.

The coefficients of viscosity, diffusion, and thermal conductivity were calculated using the Wilky and Mason–Saxena formulas [6]. The flux of water vapor

transferred through the liquid–gas interface was calculated by the Hertz–Knudsen formula

$$R_{H_2O} = \frac{\gamma m_{H_2O}(p^s_{H_2O} - p_{H_2O})}{\sqrt{2\pi m_{H_2O} RT}}, \quad (6)$$

where T is the surface temperature, $p^s_{H_2O}$ is the saturated water vapor pressure at this temperature, p_{H_2O} is the partial pressure of water at the surface, γ is the condensation coefficient, and m_{H_2O} is the molecular weight of water.

The thermal field in the drop was calculated in the form of temperature profiles along the normal to the liquid surface. The calculations were performed using an equation written in the frame of reference moving at a velocity equal to that of evaporated water (v_s) [7]:

$$\rho^* c_p^* \frac{\partial T^*}{\partial t} - \rho^* c_p^* V_s \frac{\partial T^*}{\partial y^*} = \lambda \frac{\partial^2 T^*}{\partial y^{*2}} + \alpha I e^{-\alpha y^*}, \quad (7)$$

with the boundary condition $\lambda^* \partial T^*/\partial y^* = \rho^* h V_s$. Here, t is the current time, y^* is the coordinate along the normal to the surface, λ^* is the thermal conductivity, c_p^* is the heat capacity, h is the specific heat of water evaporation, ρ^* is the water density, and T^* is the radiant power density. The velocity of the evaporation surface was calculated as

$$V_s = \frac{R_{H_2O}}{\rho^*}, \quad (8)$$

while the gas velocity at the drop surface was determined by the formula

$$V_g = V_s \frac{\rho^*}{\rho}. \quad (9)$$

The recoil force acting upon the drop in the laser beam direction (x axis) was defined as

$$F_x = \int_S V_{gx}^2 \rho \, ds, \quad (10)$$

where V_{gx} is the gas velocity component along the x axis.

Results of calculations and experiments. The experiments were performed in a setup described previously [1]. A drop with a diameter of $D = 2.6$ mm formed at a height of $h = 12$ mm above the zone of interaction with the CO_2 laser beam. After the interaction, the drop traveled a distance $H = 135$ mm down to a level where the horizontal displacement L (caused by the recoil force due to water evaporation) was determined. The laser beam had a diameter of $d = 1.6$ mm in the interaction zone and was characterized by a Gaussian power density distribution in the beam cross section.

In order to adequately calculate the temperature field in the drop and describe the related effects (e.g., the onset of laser-induced explosion boiling), it is necessary to know the condensation coefficient for water. For determining this value, we have calculated the horizontal displacement L using the system of Eqs. (1)–(10) and verified two values of the condensation coefficient reported in the literature: $\gamma = 0.04$ [8] and 1.0 [9]. In [10], the condensation coefficient was determined by one-dimensional modeling of water evaporation under the conditions of an acoustooptical experiment [11]. Calculations with both $\gamma = 0.04$ and 1.0 gave an amplitude of recoil pressure coinciding with measured values to within the experimental error.

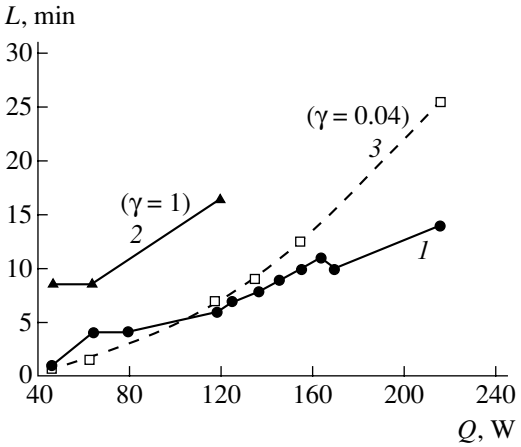

Fig. 1. The plots of (*1*) experimentally measured and (*2*, *3*) calculated values of the horizontal displacement L of a falling drop versus laser beam power Q.

Figure 1 shows the plots of experimentally measured and calculated values of the horizontal displacement L of the drop versus laser beam power Q. As can be seen, the best fit of theory to experiment is obtained with $\gamma = 0.04$. For $\gamma = 1.0$, a significant discrepancy between theoretical and experimental data takes place even at low values of the laser beam power (below 80 W), where the model is most adequate because of the low probability of uncertain effects related to explosion boiling.

Figures 2a–2c show the distribution of the mass fraction of water molecules evaporated from the drop surface. These patterns were calculated using Eqs. (1)–(6) for three moments of time counted from the beginning of interaction with the laser beam (the total interaction time was $\tau = 8.7 \times 10^{-3}$ s). There is intense ejection of vapor, and the shape of the vapor cloud agrees with the results of photographic monitoring of this process in experiment. The results of calculations show that water evaporation leads to the formation of a supersaturated vapor at the drop surface. Condensation of this vapor in the zone of interaction is unlikely [7] because water strongly absorbs the CO_2 laser radiation, as confirmed by measurements of the radiation power transmitted through a cloud of evaporated water [1].

According to the results of our calculations, the proposed model (1)–(10) with $\gamma = 0.04$ adequately

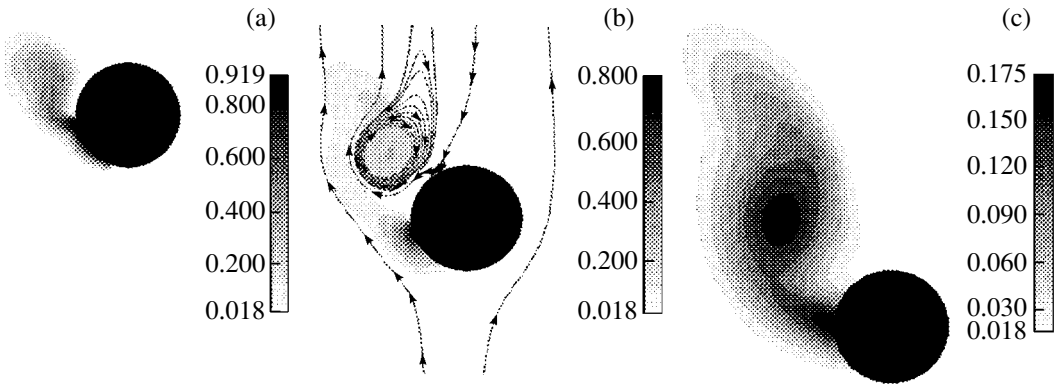

Fig. 2. Distributions of the mass fraction of evaporated water molecules around a falling drop calculated for three moments of time: (a) $t = 4.35$ ms; (b) $t = 7.35$ ms; curves show the current lines of air streamlining the drop and the distribution of water mass fraction; (c) $t = 11.75$ ms.

describes the experimentally observed effects. This value of the condensation coefficient was used in the analysis of factors responsible for the termination of the laser-induced degradation of amylopectin observed when the laser beam power exceeds a certain threshold ($Q \approx 80$ W). An analysis of the calculated temperature profiles in the surface layer of the drop showed that, as the laser beam power grows, the temperature increases up to a level at which the laser action leads to explosion boiling of water in the surface layer. The boiling front propagates through the falling drop. This leads to a decrease in nonequilibrium overheating of the surface layer of the liquid which, as was demonstrated in [1], accounts for the deformation of amylopectin macromolecules.

Conclusions. We have constructed a mathematical model describing the action of a CO_2 laser beam on a free-falling drop of water. Experiments on determining displacement of the drop under the action of a laser beam allowed us to establish the most probable value of the condensation coefficient for water ($\gamma = 0.04$). Calculations of the temperature field in the surface layer of the drop lead to the conclusion that termination of the laser-induced degradation of amylopectin dissolved in the drop falling through a laser beam can be related to the onset of explosion evaporation in the surface layer.

Acknowledgments. The authors are grateful to A.S. Segal' (State Institute of High-Precision Mechanics and Optics, St. Petersburg) for valuable remarks concerning heterogeneous systems and to Academician N.F. Morozov and Prof. D.A. Indeĭtsev (Institute of Mechanical Engineering Problems, Russian Academy of Sciences, St. Petersburg) for creative discussions of the model.

This study was supported by the Russian Foundation for Basic Research, project no. 01-01-00325.

REFERENCES

1. G. A. Baranov, A. A. Belyaev, S. B. Onikienko, *et al.*, Pis'ma Zh. Tekh. Fiz. **28** (17), 25 (2002) [Tech. Phys. Lett. **28**, 719 (2002)].
2. G. K. Batchelor, in *Theoretical and Applied Mechanics: Proceedings of the 14th IUTAM Congress, Delft, The Netherlands, 1976,* Ed. by W. T. Koiter (North-Holland, Amsterdam, 1977; Mir, Moscow, 1979).
3. M. Fiedorowicz and P. Tomasik, Carbohydrate Polym. **45** (1), 79 (2001).
4. G. A. Baranov, S. B. Onikienko, V. V. Khukharev, *et al.*, in *Proceedings of the 8th International Congress of European Medical Laser Association and the 1st Russian Congress of Medical Laser Association, Moscow, 2001,* pp. 15–16.
5. B. V. Alekseev and A. M. Grishin, *Physical Gasdynamics of Reacting Media* (Vysshaya Shkola, Moscow, 1985).
6. Yu. V. Lapin and M. Kh. Strelets, *Internal Flows in Gas Mixtures* (Nauka, Moscow, 1989).
7. V. I. Kovalev, Tr. Fiz. Inst. Akad. Nauk SSSR **136**, 51 (1982).
8. O. Knake and I. N. Stranski, Usp. Fiz. Nauk **68**, 261 (1959).
9. A. N. Neizvestnyĭ, Dokl. Akad. Nauk SSSR **243**, 626 (1978) [Sov. Phys. Dokl. **23**, 845 (1978)].
10. V. V. Korneev, Teplofiz. Vys. Temp. **28**, 536 (1990).
11. A. F. Vitshas, V. V. Korneev, A. N. Lobanov, *et al.*, Teplofiz. Vys. Temp. **25**, 312 (1987).

Translated by P. Pozdeev

Technical Physics Letters, Vol. 29, No. 7, 2003, pp. 557–559. Translated from Pis'ma v Zhurnal Tekhnicheskoĭ Fiziki, Vol. 29, No. 13, 2003, pp. 64–69.

A Laser Operating on Coherent Intersubband Transitions with Electron Transfer to the Valence Band

É. A. Gel'vich, E. I. Golant, I. V. Kuznetsova, and A. B. Pashkovskiĭ

"ISTOK" State Unitary Enterprise, Fryazino, Moscow oblast, Russia

Received January 10, 2003

Abstract—We suggest a new approach to creation of a quantum cascade laser with coherent electron transport on intersubband transitions with electron transfer from a quantum well to the valence band. © *2003 MAIK "Nauka/Interperiodica".*

Increasing demand for compact sources of coherent radiation in the terahertz frequency range has stimulated the development of semiconductor lasers employing electron transitions between quantum confinement levels in quantum wells (QWs) formed by various heterojunctions. The most known representative of these devices is the quantum cascade laser based on GaAs/AlGaAs and GaInAs/AlInAs heterojunctions [1], in which the electron processes take place only in the conduction band. Every injected electron traveling from emitter to collector participates in numerous radiative transitions (cascade scheme). The main nonradiative process in such lasers is scattering on the optical phonons, which results in a relatively high start current.

This disadvantage can be eliminated using the scheme of coherent quantum cascade laser [2], which differs from the usual heterostructures by a significantly smaller thickness of potential barriers, such that injected electrons pass through the active region not experiencing collisions with optical phonons, while retaining a sufficiently high probability of a radiative transition. It was demonstrated [3, 4] that this regime not only provides for a decrease in the threshold current, but allows reaching a record quantum efficiency of up to 66% per active cell (without taking into account the cascade process). Such a high quantum efficiency is, however, obtained only for the transitions between energy levels with sufficiently large numbers, for which the widths of the upper and lower levels become approximately equal. For the transitions between low-lying energy levels, the quantum efficiency is significantly lower because not all electrons transferred via the upper (broader) level can pass to the lower (narrower) level. For example, the quantum efficiency for the transitions between second and first (ground) levels drops to 12%.

A possible solution of this problem consists in using electron transitions between quantum confinement levels in QWs situated in different energy bands of a semiconductor material [5]. This approach allows the width of the working levels to be more readily controlled due to different barrier heights in the conduction and valence bands. In this scheme, the emission quantum energy is always greater than the bandgap width of the QW material, which limits the possibility of approaching the terahertz range. In order to remove this limitation, it is possible to use electron transitions in a QW implementing a broken-gap heterojunction [6]. In practice, this is achieved in an AlSb/InAs/GaSb/AlSb heterostructure with AlSb barriers and a QW containing the InAs/GaSb heterojunction. In this system, the electron transitions are performed to a level formed as a result of hydridization of the electron states in the conduction band of InAs and the hole states in the valence band of GaSb [7].

It should be noted that the possibility of using these hybrid states for the effective lasing remains insufficiently studied. For this reason, it is expedient to try an approach in which both working levels occur in the conduction band and the width of the lower level is determined by the power (a product of the width and height) of a potential barrier in the valence band. An example of such a structure is schematically depicted in the figure.

In order to estimate the high-frequency conductivity and quantum efficiency of this structure, we have used a method developed recently [8] based on the simplest two-band Kane model taking into account a nonparabolic law of dispersion of the charge carriers. In this model, the interaction between states of the conduction and valence bands is described taking into account only states in the light hole subband of the valence band. The interaction with other (distant) subbands is approximately taken into account by using a free fitting parameter (which additionally provides for the possibility of matching the effective masses of electrons and holes to the experimental data). The notation used in the formulas below is the same as in [8].

Let us consider a flux of electrons with the energy $\varepsilon = E - E_{c0}$ incident onto the left side of the structure depicted in the figure. The structure occurs in a homogeneous high-frequency electric field $U(x) = -qFx$ with

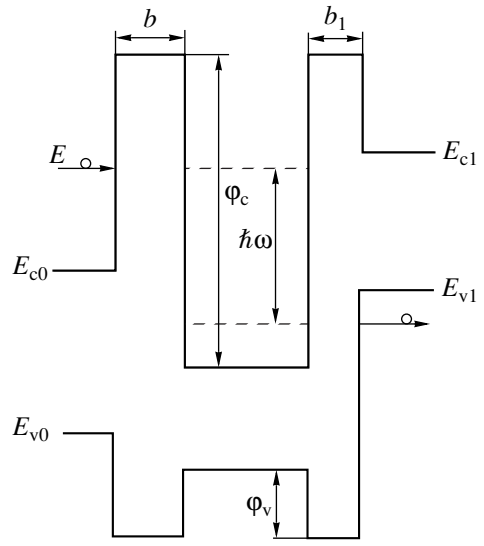

A schematic diagram of the semiconductor structure studied.

the electric field strength F varying in time according to the law $2F\cos\omega t = F(e^{i\omega t} + e^{-i\omega t})$. Let us consider the second barrier of the heterostructure (the boundary conditions at the first barrier have been treated in great detail in [8]). Let φ_c denote the barrier height in the conduction band, and φ_v, the same in the valence band. As can be shown for thin barriers ($kb \ll 1$),

$$\psi'(+0) - \frac{m(+0)}{m(-0)}\psi'(-0) \approx \left[\frac{2m(+0)}{\hbar^2}\varphi_c b_1\right]\psi(0)$$

$$= \frac{m(+0)}{m(-0)}Rg_c\psi(0), \quad E > E_c,$$

$$\psi(+0) - \psi(-0) \approx \frac{(E_c - E_v + \varphi_v)b_1}{E - E_{v1}}\psi'(-0) = g_v\psi'(+0), \quad (1)$$

$$E < E_v,$$

where the expression in square brackets (denoted by Rg_c) is analogous to the product of the barrier power and the effective electron mass $\frac{2m^*\alpha}{\hbar^2}$ [3, 4] and factor R is the ratio of powers of the second and first potential barriers.

In the resonance two-level approximation, the electron wave function for the levels with numbers N and L in the high-frequency electric field can be written as

$$\psi \approx \psi_N(x)e^{-i\omega_0 t} + \psi_L(x)e^{-i(\omega_0 - \omega)t}. \quad (2)$$

The wave function coefficients ψ_N and ψ_L inside the structure can be represented (as in the single-band model [3, 4]) in the form of a product of a constant factor by an alternating series (geometric progression)

$$1 - z + z^2 - z^3 + \ldots + (-1)^n z^n, \quad (3)$$

the sum of which in the domain of convergence ($z < 1$) is $1/(1 + z)$. Here,

$$z = \frac{4\xi_-(E_N)\xi_+(E_L)g_c^4R^2|m_{1-}|(1 + g_v^2k_{1-}^2)m_0}{k_{1-}k_0m_-m},$$

$$\xi_\pm(E) = \frac{qF}{2m(E)\omega^2} \quad (4)$$

$$\times \frac{E_p(2E - 2E_v \pm \hbar\omega) + 2\zeta(E - E_v)(E - E_v \pm \hbar\omega)}{E_p(E - E_v + \varepsilon \pm \hbar\omega) + \zeta(E - E_v)(E - E_v \pm \hbar\omega)}.$$

The calculation yields

$$\psi_N(x) = \begin{cases} \exp(ik_0x) + D\exp(-ik_0x), & x < 0, \\ A\sin(kx) + B\cos(kx), & 0 < x < a, \\ C\exp(-\kappa_1(x - a)), & x > a, \end{cases}$$

$$D = \frac{1 - z}{1 + z}, \quad A = \frac{1}{1 + z}\frac{2g_c}{k}, \quad B = \frac{2}{1 + z}, \quad C = \frac{2}{R}\frac{(-1)^{N+1}}{1 + z},$$

$$\psi_L(x) = \frac{1}{1 + z}\begin{cases} D_-\exp(\kappa_{0-}x), & x < 0, \\ A_-\sin(k_-x) + B_-\cos(k_-x), & 0 < x < a, \\ C_-\exp(-ik_{1-}(x - a)), & x > a, \end{cases} \quad (5)$$

$$C_- \approx -\frac{4m_{1-}Rg_c^2\xi_-(1 + g_v^2k_{1-}^2)}{im_-k_{1-}(1 + ig_v^2k_{1-})},$$

$$A_- \approx -\frac{4m_1R^2g_c^3\xi_-(1 + g_v^2k_{1-}^2)}{im_-k_-k_{1-}},$$

$$D_- \approx B_- \approx \frac{k_-A_-}{g_c},$$

where k is the wavevector of electrons inside the quantum well; k_0 and k_1 refer to electrons on the left and right sides of the structure, respectively, and k_{1-}, to the electrons having passed left to right with emission of the energy quantum $h\omega$; R is the ratio of the second to first barrier thicknesses.

Using expressions (5), the high-frequency conductivity of the structure studied can be determined as

$$\sigma = -\frac{\hbar\omega}{2aF^2}j[\psi_-(a)], \quad (6)$$

where $j[\psi_-(a)]$ is the flux of electrons from the structure to the valence band. For the electron energies small relative to the conduction band bottom ($E - E_{c0} \ll E_g$, E_g =

$E_c - E_v$) and $\zeta = 0$ (effective electron mass equal to the light hole mass), expression (6) reduces to the formula

$$\sigma = \frac{16q^2 g_c^4 k_- M^2 R^2 (1 + g_v^2 k_{1-}^2) E_{g1} n}{\pi L \omega^3 m^2 k_{1-}^3}. \quad (7)$$

Under these conditions, the width of the lower resonance level with the energy E_L is

$$\Gamma = \frac{4k_{1-}k_- m_{1-}(E_L - E_C)}{\pi L g_c^2 R^2 m_- (1 + g_v^2 k_{1-}^2)}. \quad (8)$$

These results are of special interest in two respects. First, there is a certain amplitude of the high-frequency field corresponding to $z = 1$, for which the reflection coefficient D in Eqs. (5) becomes zero. For this amplitude, all incident electrons with the energy corresponding to the center of the upper level pass to the lower level and then exhibit tunneling via the second potential barrier to the valence band. This process is fully analogous to the electron transfer in the case of coherent tunneling via two-barrier structures with energy levels belonging to the same band [3, 4].

Second, by selecting the mutual arrangement of bands in the structure so that the upper level would correspond to the forbidden band of the right-hand semiconductor, and the lower level, to that of the left-hand material (as depicted in the figure), it is possible to provide for the situation when the upper level width is determined by the power of the first (input) barrier and the lower level width, by that of the second (output) barrier. Under these conditions, the lower level width can be greater than that of the upper level, which is impossible in single-band transport schemes.

When the structure is pumped by the current with a real carrier energy distribution, such broadening of the lower (output) level results in that the increasing fraction of electrons transferred to the upper level will pass to the lower level with emission of an energy quantum. As can be readily shown, the quantum efficiency of this process, provided an optimum ratio of the upper to lower level width, may reach up to 80%. Under the coherent electron transport conditions, a small-signal conductivity (7) can be maintained at a sufficiently high level, ensuring an acceptable threshold current.

Acknowledgments. This study was supported by the Russian Foundation for Basic Research, project no. 00-02-17119.

REFERENCES

1. J. Faist, F. Capasso, D. L. Sivco, *et al.*, Science **264**, 553 (1994).
2. E. I. Golant, A. B. Pashkovskiĭ, and A. S. Tager, Pis'ma Zh. Tekh. Fiz. **20** (21), 74 (1994) [Tech. Phys. Lett. **20**, 886 (1994)].
3. E. I. Golant and A. B. Pashkovskiĭ, Pis'ma Zh. Éksp. Teor. Fiz. **63**, 559 (1996) [JETP Lett. **63**, 590 (1996)].
4. E. I. Golant and A. B. Pashkovskiĭ, Zh. Éksp. Teor. Fiz. **112** (7), 237 (1997) [JETP **85**, 130 (1997)].
5. R. Q. Yang, Superlattices Microstruct. **17**, 77 (1995).
6. K. Ohtani and H. Ohno, Appl. Phys. Lett. **74**, 1409 (1999).
7. E. Halvorsen, Y. Galperin, and K. A. Chao, Phys. Rev. B **61**, 16743 (2000).
8. E. I. Golant and A. B. Pashkovskiĭ, Pis'ma Zh. Éksp. Teor. Fiz. **75** (2), 88 (2002) [JETP Lett. **75**, 83 (2002)].

Translated by P. Pozdeev

Technical Physics Letters, Vol. 29, No. 7, 2003, pp. 560–562. Translated from Pis'ma v Zhurnal Tekhnicheskoĭ Fiziki, Vol. 29, No. 13, 2003, pp. 70–76.

Nanoparticle Velocity Relaxation in a Condensed Carrying Medium

V. Ya. Rudyak* and A. A. Belkin

Novosibirsk State Architecture-Building University, Novosibirsk, Russia

** e-mail: rudyak@ngasu.nsk.su*

Received January 16, 2003

Abstract—The interaction of a nanoparticle occurring in a carrying condensed medium with fluctuations of the medium momentum caused by the particle motion have been studied. The space–time velocity correlation functions of the nanoparticle and surrounding molecules were determined by the molecular dynamics method. These functions exhibit one or two maxima, depending on the system parameters. The first maximum is related to an acoustic wave propagating in the medium, and the second, to multiple collisions between the nanoparticle and nearest neighbor molecules. It is established that collective effects significantly influence both the velocity autocorrelation function and the diffusion coefficient of the nanoparticle. © *2003 MAIK "Nauka/Interperiodica".*

The increasing role of nanoparticles in various fields (advanced technologies, colloid chemistry, biophysics, etc.) makes it necessary to study the mechanisms of relaxation of such objects in liquids and gases. Nanoparticles occupy an intermediate position between molecules and coarse dispersed particles, which accounts for a rather specific physical pattern of their relaxation and related transfer processes. Attempts at describing, for example, the process of nanoparticle diffusion within the framework of the classical concept of Brownian particles are unsuccessful. For example, our study of the diffusion of nanoparticles in rarefied gases [1] showed that the well-known experimental Cunningham–Mulliken–Davis correlation based on the Einstein diffusion model is absolutely inapplicable to description of sufficiently small particles. The hydrodynamic models of streamlining in a continuous medium are obviously unjustified. It was experimentally established [2, 3] that the diffusion coefficients of large molecules and fullerenes in liquid solvents significantly exceed the values predicted by the Stokes–Einstein hydrodynamic law. The error of calculations using this law grows with decreasing ratio of the diameters of a disperse particle and a solvent molecule: for the diffusion of fullerene C_{60} in benzene, this error amounts to about 25%.

The process of nanoparticle relaxation is related to the nature of its interaction with the carrying medium. The character of relaxation of the velocity of a molecule (probe) in a molecular medium is determined by two processes [4]: individual interactions of the probing particle with molecules of the medium give rise to a local perturbation, which is subsequently dissipated by means of diffusion. Accordingly, the autocorrelation function of the probe velocity $\psi_{vv} = \langle \mathbf{v}_p(0)\mathbf{v}_p(t)\rangle / \langle v_p^2(0)\rangle$ (here and below, $\mathbf{v}_p$ is the velocity of a probing molecule or nanoparticle and angle brackets denote averaging) reveals two relaxation stages. As was originally established in [5], the second stage has a power character: $\psi_{vv} \sim t^{-3/2}$ (see also [6]). It should be noted that this power "tail" of the autocorrelation function accounts for only a few percent of the total magnitude.

Recently [6, 7], we have studied the diffusion of a nanoparticle in a condensed molecular medium by the molecular dynamics method. The interaction between molecules of the medium and between these molecules and the nanoparticle was modeled by the hard sphere potential. It was found that the autocorrelation function is described by a curve that also reveals at least two different regions, but both have exponential character. An analysis of the relaxation times showed that velocity decay in first region is related to individual interaction of the nanoparticle with molecules of the medium, so that this stage may be called kinetic. At this stage, the nanoparticle (unlike a diffusing molecule) loses a small part of the momentum and the velocity autocorrelation function decreases, depending on the particle mass, only by a few percents relative to the initial value.

In a condensed medium, the relaxation time in the second stage is about ten times that in the first (kinetic) stage. It was suggested [6, 7] that the second relaxation region of the velocity autocorrelation function reflects the interaction of the nanoparticle with microfluctuations of the fields of macroscopic variables of the carrying medium. This hypothesis was confirmed by numerical estimates. However, the mechanism of a collective interaction of the medium with the nanoparticle was not studied.

Here, we report on the results of investigation of this collective interaction using the molecular dynamics

1063-7850/03/2907-0560$24.00

method developed previously [6, 7] for a system of hard spheres in a cell with periodic boundary conditions. A cubic cell with volume V contains a single nanoparticle with diameter σ_p and N molecules with diameter σ. The relative density of the medium $\alpha = (V - V_p)/V_0$ was varied from 2 to 10 (V_p is the volume of the nanoparticle and $V_0 = N\sigma^3/\sqrt{2}$ is the close packed volume of the carrying medium).

For a closed system in the absence of external forces, the collective interaction of a nanoparticle with the medium can lead to a nonzero observable effect only in the presence of microfluctuations of the fields of macroscopic variables of the carrying medium. It is possible to separate two types of such fluctuations: (i) equilibrium homogeneous fluctuations, which are also present in the initial equilibrium homogeneous molecular medium, and (ii) nonequilibrium heterogeneous fluctuations caused by the motion of a nanoparticle in the molecular medium.

The first question that must be answered is which of the two types of fluctuations makes a decisive contribution to relaxation of the nanoparticle velocity at large times. In order to elucidate this, we have performed a series of numerical calculations aimed at determining the character of evolution of the velocity autocorrelation function of the nanoparticle in two essentially different situations. In the first case, we studied relaxation of the velocity of a nanoparticle occurring in thermal equilibrium with the molecular thermostat. In the second case, a nanoparticle placed into the equilibrium molecular medium had an initial velocity ten times greater than the thermal value. It was found (see Fig. 1) that the process of the particle velocity relaxation in both cases is the same. This implies that mechanisms of the interaction between the nanoparticle and the medium in both equilibrium and nonequilibrium situations are identical. Therefore, we may ascertain that the equilibrium stochastic fluctuations do not significantly influence behavior of the ψ_{vv} function in both situations described above. Otherwise, a rapidly moving nanoparticle could be stopped only provided that the fluctuational momentum would be comparable with that of the particle. In an equilibrium system, the probability of such a correlated molecular motion is extremely small.

Thus, relaxation of the nanoparticle velocity at large times is caused by nonequilibrium microfluctuations generated by this nanoparticle moving in a molecular medium. The influence of this motion on the distribution of molecular velocities v_f in the medium is conveniently described in terms of the space–time correlation function

$$\psi^f_{vr}(t, r) = \mathbf{v}_p(0)\frac{\sum_{i=1}^{N}\mathbf{v}_{fi}(t, r)}{N\langle v_p\rangle\langle v_f\rangle}, \quad (1)$$

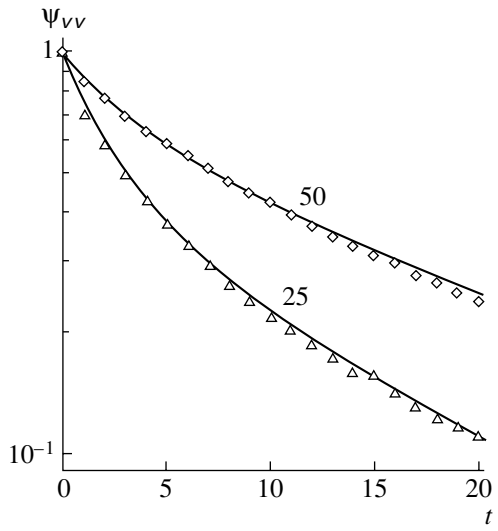

Fig. 1. The velocity autocorrelation functions of an equilibrium (solid curves) and a nonequilibrium (symbols) systems calculated for $\alpha = 4.8$, $R/r = 4$, and $M/m = 25$ and 50.

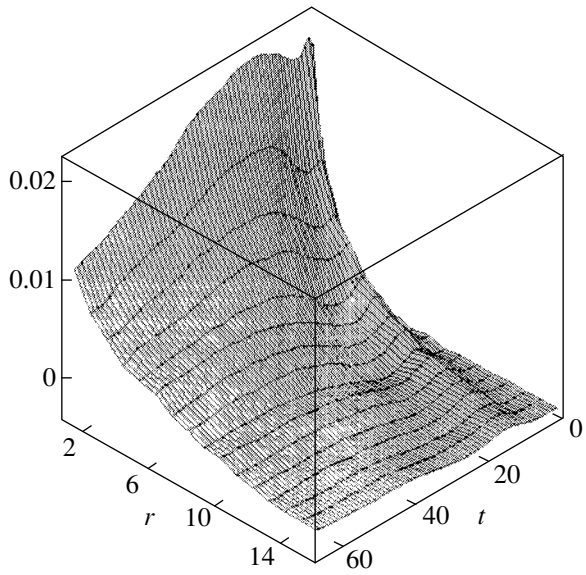

Fig. 2. A typical correlation function $\psi^f_{vr}(r, t)$ of an equilibrium system described by Eq. (1) for $\alpha = 4.8$, $R/r = 4$, and $M/m = 100$.

where r is the distance from the nanoparticle to the ith molecule. In order to calculate function (1), the space around the nanoparticle was divided into concentric spherical layers, each having a width equal to the molecular radius. Then, correlations entering into (1) were calculated in each layer for a discrete set of times.

Figure 2 shows the typical behavior of the correlation function (1) for an equilibrium system. Here, the time is measured in units of the mean free time of the carrying medium and the distances are expressed in

units of the molecular radius. As can be seen, the function exhibits two maxima, the first corresponding to the sound velocity in the medium under consideration. The second maximum (for massive nanoparticles) exceeds the first in both magnitude and width on the time scale. The character of this correlation function significantly depends on the nanoparticle to molecule mass ratio. As this ratio decreases, the second maximum decreases in intensity and vanishes. With increasing mass ratio, the second maximum grows and almost absorbs the first.

Thus, a nanoparticle generates an acoustic wave ion the carrying medium thus driving the nearest neighbor molecules in the direction parallel to the particle velocity vector. The nearest neighbors transfer the momentum to molecules of the subsequent layers and then move slower or even reverse the direction of motion. This corresponds to a region between the two maxima of the correlation function. Subsequent behavior of the correlation function depends on the nanoparticle mass and size. If the mass is sufficiently large and the nanoparticle can drive the nearest neighbor molecules again, function (1) will exhibit the second maximum. Naturally, this maximum will not appear in a rarefied medium, where the probability of multiple nanoparticle–molecule collisions is small and correlations rapidly decay. It should be noted that the velocity correlations are substantially retarded and the values of $\psi^f_{v,r}(t, r)$ at $t = 0$ are virtually zero at any distance from the nanoparticle.

The diffusion of Brownian particles is usually described in terms of the Einstein diffusion coefficient

$$D = kT/M\gamma, \tag{2}$$

where γ is a certain coefficient describing the resistance of the medium to the nanoparticle and M is the particle mass. However, since the relaxation of nanoparticles is not described by a single relaxation time, formula (2) is inapplicable to the system studied. The results of calculations showed that the diffusion coefficient can significantly exceed the values predicted both by the Stokes–Einstein law and by a modified kinetic theory (the difference reaching 30–50% for $\alpha = 4.8$, $R/r = 4$, and $M/m = 5$–100). On the other hand, the diffusion coefficient can be related to the velocity autocorrelation function ψ_{vv} of the nanoparticle using the Kubo formula

$$D = \frac{1}{3}\int_0^\infty \psi_{vv} dt. \tag{3}$$

In calculating the molecular self-diffusion coefficient, it is usually possible to neglect the power "tails" [3], after which the autocorrelation function in (3) acquires the form of an exponent with a certain relaxation time. In such cases, formulas (2) and (3) lead to virtually identical results. However, as was demonstrated above, we cannot ignore the tails of the autocorrelation function in the case under consideration. Nevertheless, it is possible to separate the systematic component of the resistance force related to kinetic processes involved in the interaction of a nanoparticle with molecules of the carrying medium. To this end, we may attempt to describe the evolution of the nanoparticle velocity fluctuation by the Langevin equation

$$M\dot{\mathbf{V}} = -\gamma^*\mathbf{V} + \mathbf{f}(t), \tag{4}$$

where $\gamma^* \sim \tau_k^{-1}$ is a resistance coefficient related to individual collisions of the nanoparticle with molecules of the carrying medium and τ_k is the usual kinetic relaxation time (in [6], this time was determined using a modified Enskog theory). The random force $\mathbf{f}(t)$ entering into the Langevin equation (4), in contrast to the Langevin source in the equation of Brownian motion, is no longer δ-correlated. It can be shown that, for an autocorrelation function of the type

$$\psi_{ff}(t', t'') = \langle \mathbf{f}(t')\mathbf{f}(t'')\rangle = \Gamma\delta(t'' - t') + a\exp[-\alpha(t'' - t')],$$

the nanoparticle velocity autocorrelation function is

$$\psi_{vv}(t', t'') = b_1\exp[-\gamma^*(t'' - t')] + b_2\exp[-\alpha(t'' - t')],$$

$$b_1 = \Gamma M/6\gamma^* kT, \quad b_2 = \alpha M/3kT(\gamma^{*2} - \alpha)^2,$$

which coincides with the function obtained previously by the molecular dynamics method [6].

Acknowledgments. This study was supported by the Russian Foundation for Basic Research, project nos. 01-01-00045 and 02-01-06333.

REFERENCES

1. V. Ya. Rudyak, S. L. Krasnolutskiĭ, A. G. Nasibulin, and E. I. Kauppinen, Dokl. Akad. Nauk **386**, 624 (2002) [Dokl. Phys. **47**, 758 (2002)].
2. D. F. Evans, T. Tominaga, and H. T. Davis, J. Chem. Phys. **74**, 1298 (1981).
3. T. Kato, K. Kikuchi, and Y. Achiba, J. Phys. Chem. **97**, 10251 (1993).
4. P. Resibois and M. de Leener, *Classical Kinetic Theory of Fluids* (Wiley, New York, 1977; Mir, Moscow, 1980).
5. B. J. Alder and T. E. Wainwright, Phys. Rev. A **1** (1), 18 (1970).
6. V. Ya. Rudyak, G. V. Kharlamov, and A. A. Belkin, Teplofiz. Vys. Temp. **31**, 283 (2001).
7. V. Ya. Rudyak, G. V. Kharlamov, and A. A. Belkin, Pis'ma Zh. Tekh. Fiz. **26** (13), 29 (2000) [Tech. Phys. Lett. **26**, 553 (2000)].

Translated by P. Pozdeev

Technical Physics Letters, Vol. 29, No. 7, 2003, pp. 563–565. Translated from Pis'ma v Zhurnal Tekhnicheskoĭ Fiziki, Vol. 29, No. 13, 2003, pp. 77–82.

The Surface Energy of a Metal Nanoparticle in the Presence of a Vacuum Gap between This Particle and a Dielectric Medium

V. A. Sozaev[a,*] and D. V. Yaganov[b,]**

[a] *Kabardino-Balkarian State University, Nal'chik, Kabardino-Balkaria, Russia*
** e-mail: sozaevv@kbsu.ru*
[b] *Institute of Applied Mathematics and Automation, Kabardino-Balkarian Scientific Center, Russian Academy of Sciences, Nal'chik, Kabardino-Balkaria, Russia*
*** e-mail: gemi_cast@rambler.ru*

Received February 17, 2003

Abstract—The surface energy of an alkali metal nanoparticle surrounded by a dielectric medium is calculated in the jelly approximation taking into account a vacuum gap between the particle surface and the medium. © *2003 MAIK "Nauka/Interperiodica".*

In developing novel nanocrystalline materials containing metal nanoparticles [1], it is difficult to provide for ideal contact between these particles and the surrounding dielectric medium. In connection with this, it would be interesting to evaluate the influence of a vacuum gap between a metal and a dielectric on the surface energy (and, hence, on the adhesion) of such a nanoparticle.

Consider a metal nanoparticle with radius R_0 surrounded by a dielectric medium with permittivity ε and let a vacuum nanogap of width H to exist between the metal surface and the dielectric. A stepwise distribution of the positive charge density in the system will be described by the function

$$n_+(r) = \begin{cases} n_0, & 0 < r < R_0; \\ 0, & R_0 < r, \end{cases} \quad (1)$$

where r is the coordinate measured in the radial direction and n_0 is the positive charge density. The electron density profile in the system is given by the function

$$n_-(r) = n_0 \begin{cases} 1 - e^{-\beta R_G}\cosh(\beta r), & r < R_G; \\ \sinh(\beta R_G)e^{-\beta r}, & R_G < r, \end{cases} \quad (2)$$

where β is a variation parameter, which depends on the permittivity ε and the charge distribution and is determined from the condition of minimum surface energy of the particle, and R_G is the coordinate of the Gibbs interface. The latter quantity is determined from the condition of charge conservation in the system,

$$4\pi q_s(R_0 + H)^2 + \frac{4\pi}{3}n_0R_0^3 = \frac{4\pi}{3}n_0R_G^3 + \frac{8\pi n_0 R_G}{\beta^2}, \quad (3)$$

where q_s is the surface charge density at the vacuum–dielectric interface.

The electrostatic potential profile in the system can be determined from the Poisson equation written in spherical coordinates,

$$\frac{1}{r^2}\frac{\partial}{\partial r}\left(r^2\frac{\partial\varphi}{\partial r}\right) = \frac{-4\pi[n_-(r) - n_+(r)]}{\varepsilon\theta(r - R_0 - H) + \theta(R_0 + H - r)}, \quad (4)$$

supplemented by the boundary conditions and the conditions of continuity of the potential and its derivative at the interfaces.

This yields for $R_G < R_0$

$$\varphi(r) = \begin{cases} \varphi_1(r) + C_1, & 0 < r < R_G, \\ \varphi_2(r) + \dfrac{4\pi n_0}{3}\left(\dfrac{r^2}{2} + \dfrac{R_0^3}{r}\right) + 4\pi q_s(R_0 + H)^2\dfrac{1}{r} + C_2, & \\ R_G < r < R_0, & \\ \varphi_2(r) + 4\pi q_s(R_0 + H)^2\dfrac{1}{r} + G_3, & R_0 < r < R_0 + H, \\ \varphi_2(r), & R_0 + H < r < \infty, \end{cases} \quad (5)$$

where

$$C_3 = -\varphi_2(R_0 + H)(1 - 1/\varepsilon) - 4\pi q_s(R_0 + H),$$

$$C_2 = C_3 - 2\pi n_0 R_0^2,$$

$$C_1 = -\varphi_2(R_0 + H)(1 - 1/\varepsilon) - 4\pi q_s(R_0 + H) - 2\pi n_0(R_0^2 - R_G^2) + 4\pi n_0/\beta^2;$$

1063-7850/03/2907-0563$24.00 © 2003 MAIK "Nauka/Interperiodica"

The values of the variation parameter β, the Gibbs coordinate R_G, and the surface energy σ_j of a sodium nanoparticle (R_0 = 10.8193 a.u.) for various values of the gap width H between the particle and a dielectric medium with permittivity ε

H, a.u.	ε = 2			ε = 81		
	β, a.u.$^{-1}$	R_G, a.u.	σ, mJ/m^2	β, a.u.$^{-1}$	R_G, a.u.	σ, mJ/m^2
0	0.960	10.6188	243.3	0.885	10.5834	222.7
0.1	0.968	10.6219	236.0	0.903	10.5926	226.6
0.5	0.990	10.6308	240.3	0.956	10.6170	236.3
1	1.006	10.6367	242.6	0.991	10.6310	241.2
2	1.017	10.6406	243.8	1.014	10.6396	243.6
3	1.019	10.6414	243.9	1.019	10.6412	243.9
4	1.020	10.6416	244.0	1.020	10.6415	244.0
5	1.020	10.6416	244.0	1.020	10.6416	244.0

for $R_0 < R_G < R_0 + H$

$$\varphi(r) = \begin{cases} \varphi_1(r) + C_1, & 0 < r < R_0, \\ \varphi_1(r) - \dfrac{4\pi n_0}{3}\left(\dfrac{r^2}{2} + \dfrac{R_0^3}{r}\right) + C_2, & R_0 < r < R_G, \\ \varphi_2(r) + 4\pi q_s (R_0 + H)^2 \dfrac{1}{r} + C_3, & R_G < r < R_0 + H, \\ \varphi_2(r), & \max(R_G, R_0 + H) < r < \infty, \end{cases} \quad (6)$$

where

$$C_3 = -\varphi_2(R_0 + H)(1 - 1/\varepsilon) - 4\pi q_s (R_0 + H),$$

$$C_2 = 2\pi n_0 R_G^2 + 4\pi n_0/\beta^2 + C_3,$$

$$C_1 = -\varphi_2(R_0 + H)(1 - 1/\varepsilon) - 4\pi q_s (R_0 + H) - 2\pi n_0 (R_0^2 - R_G^2) + 4\pi n_0/\beta^2;$$

and for $R_G > R_0 + H$

$$\varphi(r) = \begin{cases} \varphi_1(r) + C_1, & 0 < r < R_0, \\ \varphi_1(r) - \dfrac{4\pi n_0}{3}\left(\dfrac{r^2}{2} + \dfrac{R_0^3}{r}\right) + C_2, & R_0 < r < R_0 + H, \\ \varphi_1(r) - \dfrac{4\pi n_0}{3\varepsilon}\left(\dfrac{r^2}{2} + \dfrac{R^3}{r}\right) - 4\pi q_s (R_0 + H)^2 \dfrac{1}{\varepsilon r} + C_3, & \\ R_0 + H < r < R_G, & \\ \varphi_2(r), & R_G < r < \infty, \end{cases} \quad (7)$$

where

$$C_3 = 2\pi n_0 R_G^2/\varepsilon + 4\pi n_0/\varepsilon\beta^2,$$

$$C_2 = -\varphi_1(R_0 + H)(1 - 1/\varepsilon) - 4\pi q_s (R_0 + H)/\varepsilon + \frac{4\pi n_0}{3}\left(\frac{(R_0 + H)^2}{2} + \frac{R_0^3}{R_0 + H}\right)(1 - 1/\varepsilon) + C_3,$$

$$C_1 = C_2 - 2\pi n_0 R_0^2.$$

In Eqs. (5)–(7), the functions $\varphi_1(r)$ and $\varphi_2(r)$ are as follows:

$$\varphi_1(r) = \frac{4\pi n_0 e^{-\beta R_G}}{\beta^2}\left[\cosh(\beta r) - \frac{2\sinh(\beta r)}{\beta r}\right];$$
$$\varphi_2(r) = -\frac{4\pi n_0 \sinh(\beta R_G)}{\beta^2}\left[1 + \frac{2}{\beta r}\right]e^{-\beta r}. \quad (8)$$

In the homogeneous background approximation, the surface energy of the particle is given by the formula [2]

$$\sigma_j = \frac{1}{R_0^2}\left\{\frac{1}{2}\int_0^\infty \varphi(r)[n_-(r) - n_+(r)]r^2 dr + 0.3(3\pi^2)^{2/3}\int_0^\infty [n_-^{5/3}(r) - n_+^{5/3}(r)]r^2 dr - 0.75(3/\pi)^{1/3}\int_0^\infty [n_-^{4/3}(r) - n_+^{4/3}(r)]r^2 dr \right.$$
$$\left. - 0.056\int_0^\infty \left[\frac{n_-^{4/3}(r)}{0.079 + n_-^{1/3}(r)} - \frac{n_+^{4/3}(r)}{0.079 + n_+^{1/3}(r)}\right]r^2 dr + \frac{1}{72}\int_0^\infty \frac{|\nabla n_-(r)|^2}{n_-(r)}r^2 dr + C_{xc}(r_S)\int_0^\infty \frac{|\nabla n_-(r)|^2}{n_-^{4/3}(r)}r^2 dr \right\}, \quad (9)$$

where $C_{xc}(r_S) = (2.702 - 0.174 r_S) \times 10^{-3}$ and $r_S = \left(\frac{4}{3}\pi n_-\right)^{-1/3}$. Formula (9) takes into account contributions to the particle surface energy from (i) the electrostatic self-energy due to the interaction between the electron gas and the jelly charge, (ii) the kinetic energy of the noninteracting electron gas (corrected for the field inhomogeneity) in the Weizsäcker–Kirznits approximation, and (iii) exchange-correlation energy calculated in the local density approximation with a correction for nonlocality in the Geldart–Resolt approximation.

The numerical calculations were performed for a sodium nanoparticle containing 20 atoms. The procedure included minimization of the surface energy by varying the parameter β at a step of 0.001 (the quantity

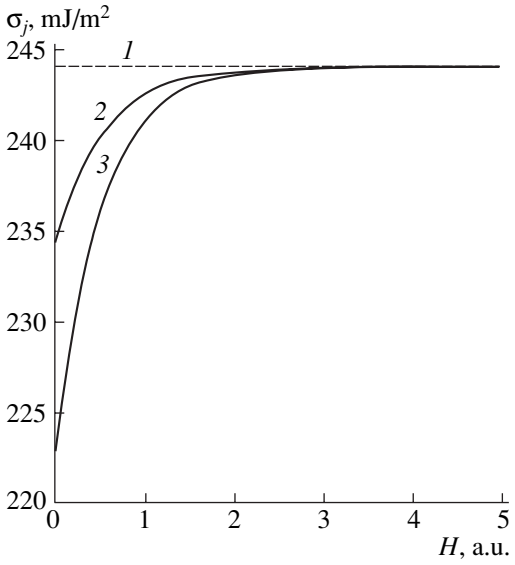

The plots of surface energy σ_j of a sodium nanoparticle versus width H of the gap between the particle and a dielectric medium with $\varepsilon = 1$ (*1*), 2 (*2*), and 81 (*3*).

inverse to β characterizes the length of the electron distribution "tail" at the vacuum–dielectric interface). The calculation accuracy was 10^{-5} for the coordinate R_G and 10^{-3} for the surface energy σ_j. The results of calculations are presented in the table and in the figure, where the gap width and the particle diameter are expressed in atomic units (Bohr's atomic radius, 1 a.u. = 0.529×10^{-10} m).

As can be seen from the figure, the surface energy increases (accordingly, the adhesion energy decreases) with the gap width, tending to a line parallel to the abscissa axis (this line represents the energy of the nanoparticle–vacuum interface). An increase in the dielectric permittivity of the medium leads to a decrease in the surface energy of the sodium nanoparticle.

Allowance for the charge q_s in the calculations of σ_j showed that the surface energy decreases in the presence of a positive charge and increases if the charge is negative. The values of the variation parameter and the Gibbs interface coordinate change with the charge sign in a similar manner.

Conclusions. (1) As the width of the vacuum gap between a metal nanoparticle and the surrounding dielectric medium increases, the surface energy of the particle increase, approaching the value for the particle–vacuum interface. (2) Significant changes in the surface energy take place for a gap width of $H < 3$ a.u., which indicates that such values correspond to the formation of high-adhesion contacts.

Acknowledgments. This study was supported by the Russian Foundation for Basic Research, project no. 03-02-96010.

REFERENCES

1. A. I. Gusev, *Nanocrystalline Materials: Properties and Production Methods* (Ural. Otd. Ross. Akad. Nauk, Yekaterinburg, 1998).
2. A. Z. Kashezhev, A. Kh. Mambetov, V. A. Sozaev, and D. V. Yaganov, Poverkhnost, No. 12, 53 (2001).

Translated by P. Pozdeev

Technical Physics Letters, Vol. 29, No. 7, 2003, pp. 566–568. Translated from Pis'ma v Zhurnal Tekhnicheskoĭ Fiziki, Vol. 29, No. 13, 2003, pp. 83–88.

Application of Holographic Interferometry for Determining the Solubility of Gases in Liquids

V. B. Konstantinov*, A. F. Malyĭ, and V. A. Babenko**

Ioffe Physicotechnical Institute, Russian Academy of Sciences, St. Petersburg, 194021 Russia

*e-mail: * V.Konstantinov@mail.ioffe.ru; ** babenko@mail.ioffe.ru*

Received January 24, 2003

Abstract—The effect of a gas dissolved in a liquid on the variation of the refractive index of the compressed mixture was studied. The compression process was monitored with the aid of a holographic interferometer. The sensitivity of this method allows the compressibility of water and the solubility of helium and nitrogen to be studied at pressures below 4 atm. A procedure for obtaining qualitative and quantitative data on the solubility of gases in liquids is proposed. *© 2003 MAIK "Nauka/Interperiodica".*

The investigation of processes in transparent media is significantly facilitated upon visualization of the related effects. Using the method of holographic interferometry, it is possible to detect very small changes in the object parameters such as deformation and refractive index. Advantages of holographic interferometry are not very high requirements to the quality of the optical system elements and the possibility of automated compensation of the influence of background temperature fields and dissolved gases on the results of measurements. The compression of a liquid containing dissolved gases leads to a change of the refractive index as a result of density and temperature variations. A change in the refractive index determined by the holographic interferometry can be used in studying the solubility of gases in liquids. A necessary condition for such measurements is the thermal stabilization, since an increase in the temperature in the course of compression is accompanied by a decrease in the density and, hence, in the refractive index of the medium.

The compressibility coefficients of liquids are very small (typically, on the order of 10^{-5} atm^{-1}). The sensitivity of a holographic interferometer increases with increasing optical pathlength of the object beam in a medium studied. The longer the pathlength, the lower the average pressure required for obtaining the interferogram [1]. The pressure-induced changes in the refractive index of a liquid with a dissolved gas range from very small (e.g., for helium, which is almost insoluble in water in a wide range of pressures) up to the values comparable to the refractive index (e.g., for nitrogen, which is well soluble in water).

In our experiments, a holographic interferometer was used to determine the change in the refractive index Δn by measuring a relative shift Δk of the interference fringes. These quantities are related as

$$\Delta n = (\lambda/L)\Delta k, \quad (1)$$

where λ is the laser wavelength and L is the pathlength of the object beam in the liquid studied [2, 3]. The experiments were performed using a laser with $\lambda = 0.63$ μm and an optical cell with $L = 10$ mm.

Compression changes the density of the medium. A relation between the densities of liquids (d_1), gases (d_2) and the refractive index is described by the Gladstone–Dale formula for the specific refraction [4]:

$$(n-1)/d = r. \quad (2)$$

Here, it is assumed that the specific refraction r is independent of the external conditions (temperature and pressure) and the sample state. The specific refractions of mixtures are virtually additive and depend on the weight fractions of the components. For a liquid–gas mixture with the component weight fractions p_1 and p_2, respectively, this yields

$$r_\Sigma = (n_\Sigma - 1)/d_\Sigma = p_1 r_1 + p_2 r_2, \quad (3)$$

where n_Σ is the refractive index of the mixture,

$$d_\Sigma = d_1 + d_2, \quad (4a)$$

$$p_1 = m_1/(m_1 + m_2), \quad p_2 = m_2/(m_1 + m_2), \quad (4b)$$

and m_1 and m_2 are the masses of liquid and gas, respectively.

Let us evaluate the values of m_1 and m_2 in the mixture. The mass of 1 liter of water at $T = 20$°C is 1 kg (to within the third decimal figure) [5], while the mass of a gas (nitrogen) dissolved in water can be calculated using the coefficient of solubility. At $T = 20$°C and a pressure of 1 atm, this coefficient is $\alpha = 0.0154$ (of the ratio of masses of equal volumes of the gas and liquid). Note that the coefficient α neither indicates the amount of nitrogen dissolved in water with increasing pressure nor informs on the linearity of this relation. According to published data [5], the coefficient of solubility for

1063-7850/03/2907-0566$24.00

nitrogen in water is $\alpha^{25} = 0.348(l_{N_2}/l_{H_2O})$ atm^{-1} at T = 25°C and ΔP = 25 atm. By taking the ratio $\alpha^{25}/25$, we obtain $\alpha = 0.0139(l_{N_2}/l_{H_2O})$ atm^{-1}, which coincides to within the third decimal figure with the vale of $\alpha = 0.0143(l_{N_2}/l_{H_2O})$ atm^{-1} at T = 25°C and a pressure of 1 atm. Therefore, the value of α at T = 20°C and partial gas pressure can be used in what follows as the coefficient of nitrogen solubility in water under increasing pressure.

The mass of nitrogen is $m_2 = \alpha d$, where d is the gas density at T = 20°C. The tabulated value at T = 0°C and P = 1 atm is $d = 1.2505 \times 10^{-3}$ g/cm^3. Using the Gay–Lussac law, we obtain $d = 1.16552 \times 10^{-3}$ g/cm^3 and, accordingly, $m_2 = 0.0179$ g.

Now let us estimate the mass fractions p_1 and p_2 in Eq. (4b). Using the known masses m_1 and m_2, we conclude that p_1 is nearly equal to unity $p_2 = m_2/m_1$. The latter ratio is essentially the coefficient of solubility α expressed via the ratio of masses: $\alpha' = m_2/m_1$ atm^{-1}. Then, in the case of simultaneous compression of the liquid and the gas in contact with this liquid, formula (3) can be presented in the following form:

$$r_\Sigma = r_1 + \alpha'\Delta P r_2, \tag{5}$$

where $r_1 = 0.332$, $r_2 = 0.2375$, and $\alpha' = 17.9 \times 10^{-6}$ atm^{-1}. As can be seen from this expression, the total specific refraction will change with the pressure, but (taking into account the value of α') the second term can be ignored even at very high pressures. Indeed, this contribution is smaller than 5×10^{-5} at ΔP = 10 atm, which is below the experimental accuracy. Therefore, the total specific refraction is

$$r_\Sigma = (n_\Sigma - 1)/d_\Sigma = r_1 = (n_1 - 1)/d_1. \tag{6}$$

Using the expression of the isobaric compressibility,

$$\chi = -(V - V_0)/[(P_2 - P_1)V_0] = -\Delta V/(\Delta P V), \tag{7}$$

where $\Delta V = V_0 - V$ is the volume difference upon compression, we obtain

$$V/V_0 = 1 - \chi\Delta P. \tag{8}$$

Rewriting formula (4a) as

$$d_\Sigma = d_1 = d_2 = (m_1 + m_2)/V, \tag{9}$$

taking into account that (for the isothermal compression)

$$m_1 + m_2 = m_1(1 + \alpha'\Delta P), \tag{10a}$$

$$V = V_0(1 - \chi\Delta P), \tag{10b}$$

and using expression (6), we obtain

$$(n_\Sigma - 1)/(n_0 - 1) = d_\Sigma/d = 1. \tag{11}$$

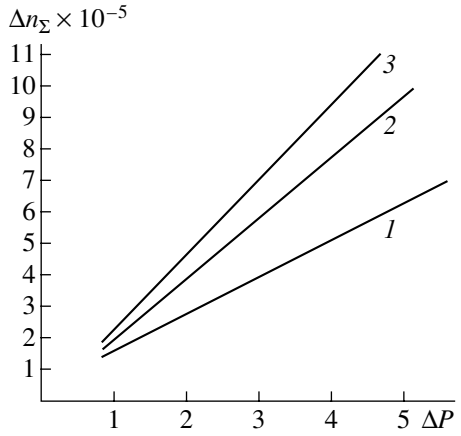

Plots of the change Δn_Σ in the total refractive index of water versus pressure of (*1*) helium, (*2*) nitrogen (theoretical calculation), and (*3*) nitrogen (experiment).

The ratio d_Σ/d_0 can be determined using formulas (10) as

$$d_\Sigma/d_0 = (1 + \alpha'\Delta P)/(1 - \chi\Delta P). \tag{12}$$

Since $\chi\Delta P \ll 1$,

$$1/(1 - \chi\Delta P) = 1 + \chi\Delta P. \tag{13}$$

Retaining terms of the first order of smallness, we obtain

$$d_\Sigma/d_0 = 1 + \chi\Delta P + \alpha'\Delta P. \tag{14}$$

Thus, a change in the refractive index Δn upon compression of the mixture is

$$\Delta n_\Sigma = (n - 1)(\chi + \alpha')\Delta P. \tag{15}$$

Equating expressions (1) and (15), we obtain

$$\chi + \alpha' = \lambda\Delta K/(L(n_0 - 1)\Delta P). \tag{16}$$

In experiment, the compression of liquid and gas can be performed either mechanically or by connecting a chamber with liquid to a vessel with gas under pressure. The figure shows plots of the change Δn_Σ in the refractive index of water versus pressure of (1) helium, (2) nitrogen (calculated using the above theory), and (3) nitrogen (experiment).

In the experiments with helium, the results of theoretical calculations coincided with the experimental data, since the solubility of helium in water is extremely small (in the pressure range studied). These data correspond to the published values of the compressibility of water [5].

The experiments showed that the solubility of nitrogen in water is higher than that predicted by the theory. The pressure dependence was always linear and only the slope varied. The slope variations can be explained, in addition to the effect of dissolved nitrogen, by an increase in the object beam pathlength in the medium and by a change in the temperature. However, the experiment with helium gives a change in the refractive

index Δn_Σ coinciding to within 2–4% with the liquid compressibility factor, which confirms that expansion of the cell with the liquid under pressure is relatively small. Estimates of a change in Δn_Σ related to the temperature deviation from the value $T = 20°C$ used in the calculation down to $T = 0°C$ showed that even this unreal temperature variation cannot be responsible for the difference observed between the experimental and theoretical plots. Therefore, we may suggest that the coefficient of nitrogen solubility in water at low pressure is significantly greater than the value used in the calculation and amounts to $\alpha' = 30 \times 10^{-6}$ atm^{-1}. It is also possible that this coefficient varies with increasing pressure (that is, the solubility of nitrogen does not linearly vary depending on the range of pressures).

Thus, we have demonstrated that dissolved gases may significantly influence change in the refractive index of a liquid under compression. Using this effect, it is possible to detect the presence of dissolved gases in a liquid, provided that the compressibility coefficient of this liquid is known. At the same time, both the experimental data and the above theoretical analysis show that identification of the dissolved gas by the value of solubility (calculated from the experimental data) and determination of the amount of dissolved gas is possible only provided that the low-pressure solubility coefficient is known.

Acknowledgments. This study was supported by the Russian Foundation for Basic Research (project no. 00-15-96771 for the Scientific School of Yu.N. Denisyuk).

REFERENCES

1. A. F. Maliy, L. G. Malkhasyan, V. B. Konstantinov, *et al.*, Pis'ma Zh. Tekh. Fiz. **20** (3), 87 (1994) [Tech. Phys. Lett. **20**, 254 (1994)].
2. Yu. I. Ostrovsky, M. M. Butusov, and G. V. Ostrovskaya, in *Springer Series in Optical Science* (Springer-Verlag, Berlin, 1980), Vol. 20.
3. H. Phillipp, T. Neger, *et al.*, Measurement **10** (4) (1992).
4. B. V. Ioffe, *Refractometric Methods of Chemistry* (Leningrad, 1969).
5. *Reference Book of Chemistry*, Ed. by B. P. Nikol'skiĭ (Moscow, 1964).

Translated by P. Pozdeev

Technical Physics Letters, Vol. 29, No. 7, 2003, pp. 569–571. Translated from Pis'ma v Zhurnal Tekhnicheskoĭ Fiziki, Vol. 29, No. 13, 2003, pp. 89–94.

Nanocrystalline Silicon Films Formed under the Impact of Pulsed Excimer Laser Radiation on Polyimide Substrates

M. D. Efremov, V. A. Volodin*, L. I. Fedina, A. A. Gutakovskiĭ, D. V. Marin, S. A. Kochubeĭ, A. A. Popov, Yu. A. Minakov, and V. N. Ulasyuk

Institute of Semiconductor Physics, Siberian Division, Russian Academy of Sciences, Novosibirsk, Russia
** e-mail: volodin@isp.nsc.ru*
Institute of Microelectronics and Informatics, Russian Academy of Sciences, Yaroslavl, Russia
ELTAN Ltd., Fryazino, Moscow oblast, Russia
Received February 7, 2003

Abstract—Polycrystalline silicon films on polyimide substrates were obtained by a method based on the crystallization of amorphous films under the impact of nanosecond pulses of excimer laser radiation. Characteristics of the film structure were studied by methods of Raman scattering and high-resolution electron microscopy. For the laser crystallization regimes employed, nanocrystalline silicon films with an average grain size of 5 nm were obtained. The results are of interest for the development of large-scale microelectronic devices (active thin-film transistor matrices) on cheap flexible substrates. © *2003 MAIK "Nauka/Interperiodica".*

The development of large-scale microelectronics poses the problem of obtaining high-quality semiconductor films on cheap nonrefractory substrates. In recent years there is a pronounced tendency to increase the area of such devices (inverse Moore's law [1]). Another important trend is the competition between semiconductor films and organic materials both in large-scale optoelectronics and in the fields of traditional semiconductor applications [2]. This has stimulated the development of new semiconductor film technologies, in particular, for the obtaining of semiconductor films on flexible plastic substrates of large area. Here, the main difficulty is the low plasticity temperature range of the substrate materials. This problem can be solved by using the method of crystallization under the conditions of pulsed heating provided by excimer laser radiation [3–5]. Recently, thin-film transistors were fabricated [6] using polycrystalline silicon films obtained by this method on poly(ether sulphone) films.

In our experiments, we obtained the initial silicon films by plasmochemical deposition in a low-frequency discharge. This methods is characterized by increased deposition rate and provides for satisfactory electrical properties of the deposit [7]. The silicon films with a thickness of 100 nm were deposited onto a polyimide film with a 370-nm-thick buffer Si_3N_4 layer. The choice of substrate material was determined by high mechanical and electrical properties of polyimide and by a relatively high plasticity temperature range (up to 250°C). The laser treatments were performed using a XeCl excimer laser operating at a wavelength of 308 nm. The coefficient of light absorption in amorphous silicon at this wavelength is 1.5×10^6 cm^{-1} [8], which implies that all incident radiation is absorbed in the silicon films, not reaching the substrate. This, together with a small laser radiation pulse duration (on the order of 10 ns), ensured that the irradiation did introduced significant overheating of the substrate film. According to the results of calculations of the spatial distribution and time variation of the temperature in the laser treatment regimes employed, the temperature at the substrate/buffer interface did not exceed 120°C. We used the regimes of laser treatment at an energy density in the vicinity of and above a threshold for the formation of macroscopic regions of local melting of the amorphous silicon. According to the published data [9], the value of the melting threshold determined in the experiments on the light reflection with a nanosecond time resolution is 120–150 mJ/cm^2. The method of crystallization under the impact of nanosecond excimer laser radiation pulses is described in more detail elsewhere [4].

The Raman spectra of the samples were recorded using an automated setup based on a DFS-52 spectrometer (LOMO, St. Petersburg) linked to computer via a CAMAC interface. The spectra were excited by 514.5 nm radiation from an Ar laser. The Raman measurements were performed in a quasibackscattering mode at a laser beam incidence angle close to the Brewster angle for silicon. The scattered light was detected without a polarizer (i.e., with an arbitrary polarization). The film structure was studied by high-resolution electron microscopy (HREM) using a JEOL 4000EX electron microscope (Japan) operating at an accelerating voltage of 250 keV, for which the lateral point resolution is 0.19 nm.

Figure 1 shows typical Raman spectra of the initial silicon film and the films treated by the excimer laser radiation. The spectrum of the initial silicon deposit

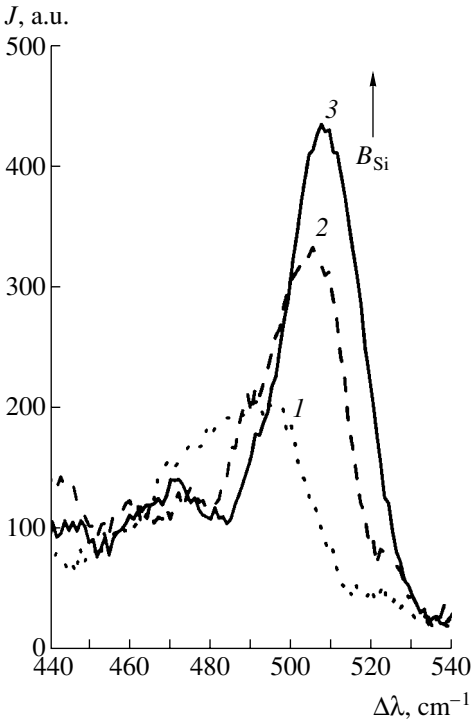

Fig. 1. Raman spectra of silicon films: (*1*) initial deposit; (*2*) silicon films processed by XeCl laser without melting; (*3*) silicon films processed in the regime with partial melting.

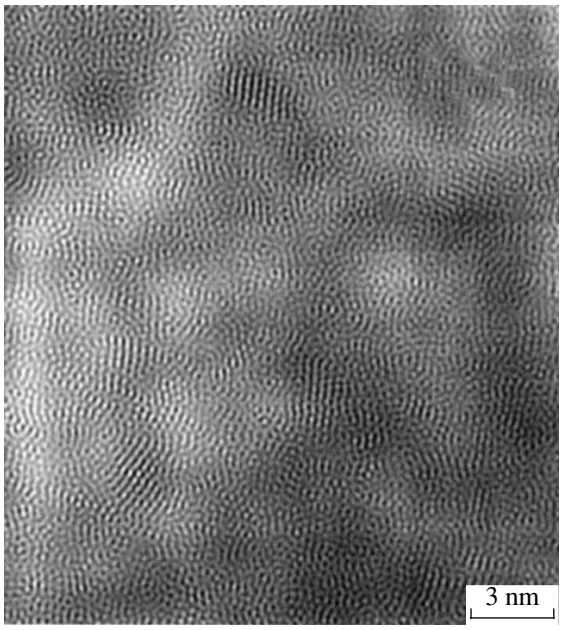

Fig. 2. A typical HREM image of a nanocrystalline silicon obtained by laser crystallization in the regime without melting.

(curve *1*) contains a peak with a width of about 50 cm^{-1} and a maximum at about 485 cm^{-1}. This signal corresponds to the Raman scattering on optical vibrations of the Si–Si bonds in amorphous silicon. The presence of a high-frequency shoulder extended up to 500 cm^{-1} is evidence of a small amount of nanocrystalline inclusions with an average size on the order of 1.5 nm. In order to initiate crystallization of the amorphous films under the impact of excimer laser radiation at an energy density below the melting threshold, it was necessary to the treat the samples in a repeated mode (5 pulses). The Raman spectrum of a sample processed in this regime (Fig. 1, curve *2*) shows significant transformation of the peak, which becomes narrower (22 cm^{-1}) and is shifted to higher wavenumbers (a maximum at 503 cm^{-1}). The intrinsic vibrational modes of nanocrystals are spatially localized. For this reason, the Raman spectra of nanocrystals exhibit a peak whose position depends on the grain size and, as the grain size increases above 50 nm, becomes almost identical to the signal from a single crystal silicon (520 cm^{-1}). The width of this peak is determined by the dispersion of grain dimensions and by the phonon lifetime. The grain average size was estimated by calculation using the method of effective convolution of the vibrational states [10]. According to the results of these calculations, the average grain size corresponding to spectrum *2* in Fig. 1 is about 3 nm. When the laser energy density was increased above the melting threshold, the film exhibited crystallization after exposure to a single radiation pulse and the average grain size in the film increased. According to the corresponding Raman peak position (Fig. 1, curve *3*) at 508 cm^{-1}, the average size of nanograins in this film was estimated at 4–5 nm. The ratio of intensities of the amorphous and nanocrystalline signal components shows that the latter film is almost completely crystallized.

The results of HREM observations agreed well with the above analysis of the Raman spectra. Figure 2 shows a typical HREM image of the atomic structure of a nanocrystalline silicon film corresponding to spectrum *2* in Fig. 1. As can be seen, the average grain size in this sample is about 3 nm. However, the dimensions of some grains reach up to 10 nm. The local volume density of grains varies from 10^{16} to 10^{19} cm^{-3}. It should be noted that a characteristic morphological feature of the grains formed in the course of solid-state laser recrystallization is the absence of distinct grain boundaries in the amorphous matrix. In our opinion, this is related to the chain crystallization mechanism, according to which the crystal phase is nucleated on one-dimensional chains of silicon atoms oriented in the ⟨110⟩ direction, formed by means of small displacements of the closely spaced atoms in the amorphous silicon matrix. The presence of ⟨110⟩-oriented atomic chains is clearly traced in the structure of amorphous matrix surrounding the grains, but the dimensions of these chains are small and correspond to the minimum grain size in the amorphous matrix (1–1.5 nm according to Fig. 2). It is suggested that the formation of such grains in the initial amorphous silicon films is related to the formation of silicon clusters in the gas phase during

the plasmochemical deposition [11]. This initial crystallization can be additionally stimulated by the ion component in the deposited silicon vapor [12].

Thus, we have crystallized the initially amorphous silicon films on a plastic substrate by treating these films with nanosecond pulses of excimer laser radiation. This technology can be used in a scan mode for the obtaining of nano- and microcrystalline silicon films of large-area substrates.

REFERENCES

1. M. S. Shur, S. L. Rumyantsev, and R. Gaska, in *Proceedings of the 10th International Symposium "Nanostructures: Physics and Technology," 2002*, pp. 618–622.
2. Zh. I. Alferov, in *Proceedings of the 10th International Symposium "Nanostructures: Physics and Technology," 2002*.
3. S. Chen and I. C. Hsieh, Solid State Technol., No. 1, 113 (1996).
4. M. D. Efremov, V. V. Bolotov, V. A. Volodin, *et al.*, Fiz. Tekh. Poluprovodn. (St. Petersburg) **36**, 109 (2002) [Semiconductors **36**, 102 (2002)].
5. M. D. Efremov, V. V. Bolotov, V. V. Volodin, *et al.*, Solid State Commun. **108**, 645 (1998).
6. D. P. Gosain, T. Noguchi, and S. Usui, Jpn. J. Appl. Phys. **39**, L179 (2000).
7. B. G. Budagyan, A. A. Popov, and A. E. Berdnikov, in *Abstracts of the All-Russia Symposium on Amorphous and Single-Crystal Semiconductors, St. Petersburg, 1998*, pp. 21–22.
8. V. I. Gavrilenko, A. M. Grekhov, D. V. Korbutyak, and V. G. Litovchenko, *Optical Properties of Semiconductors* (Naukova Dumka, Kiev, 1987).
9. T. Sameshima and S. Usui, J. Appl. Phys. **70**, 1281 (1991).
10. V. Paillard, P. Puech, M. A. Laguna, *et al.*, J. Appl. Phys. **86**, 1921 (1999).
11. L. Kronik, R. Fromherz, E. Ko, *et al.*, Nature Materials **1**, 1 (2002).
12. C. Spinella, S. Lombardo, and F. Priollo, J. Appl. Phys. **84**, 5383 (1998).

Translated by P. Pozdeev

Technical Physics Letters, Vol. 29, No. 7, 2003, pp. 572–574. Translated from Pis'ma v Zhurnal Tekhnicheskoĭ Fiziki, Vol. 29, No. 14, 2003, pp. 1–7.

A Mechanism of Current Noise Reduction in Systems of Ion Beam Formation from Vacuum Arc Plasma

V. A. Shklyaev*, S. Ya. Belomyttsev, V. V. Ryzhov, and I. Yu. Turchanovskiĭ

Institute of High-Current Electronics, Siberian Division, Russian Academy of Sciences, Tomsk, Russia

** e-mail: shklaev@to.hcei.tsc.ru*

Received February 19, 2003

Abstract—The influence of a residual gas plasma on the ion beam transport in the drift chamber of an ion source based on the vacuum arc discharge was numerically simulated by the pellet injection method. The plasma formed as a result of ionization of the residual gas causes a change in the potential profile in the drift chamber. This leads to the appearance of an extended slow ion transport zone (occurring at a virtual anode potential) and to a change in the mechanism of suppression of the ion current noise as compared to the well-known mechanism operative in an equipotential vacuum gap. The results of model calculations show that the modified mechanism is related to a spatial redistribution of the density of ions (in the beam characterized by a certain scatter of velocities) in the slow ion transport zone. *© 2003 MAIK "Nauka/Interperiodica".*

The parameters of ion beams generated in a vacuum arc discharge depend on the state of plasma and, since the arc discharge featuring transient processes in cathode spots is essentially unstable, the ion beam current is subject to fluctuations in time. In order to obtain ion beams with parameters independent of the plasma source instability, the systems of ion beam formation are provided by grid control [1–3].

In a system for the ion beam formation with grid control (Fig. 1), plasma generated by the arc discharge expands and enters the accelerating gap through an anode grid. A high voltage applied to the gap separates the plasma electrons and ions and accelerates the latter. Passing through a cathode grid, ions enter the equipotential drift chamber, where the spatial charge of ions forms (under certain conditions) a virtual anode.

The main role in stabilization of the ion current in such systems belongs to the equipotential drift chamber. Should the beam current in the flat drift chamber exceed a certain critical level, a virtual anode is formed that reflects some of the ions, thus limiting the current passing through the chamber. The flat equipotential

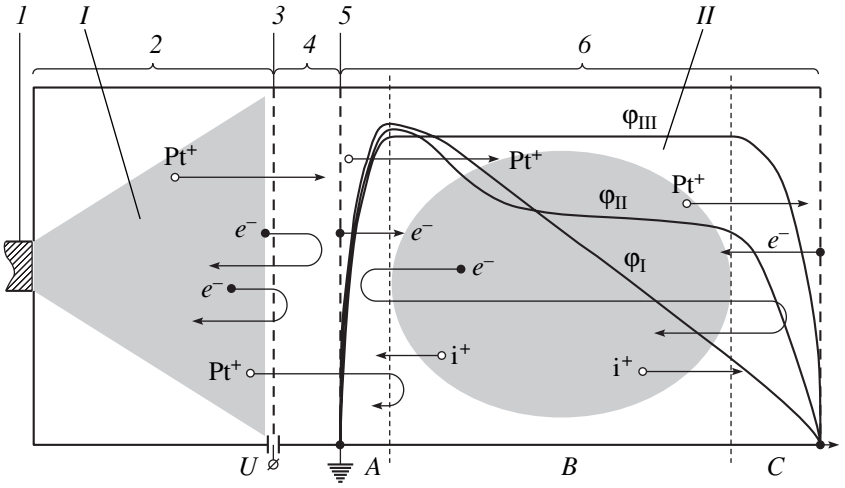

Fig. 1. A schematic diagram of the ion beam source with grid control illustrating the dynamics of variation of the virtual anode potential profile as a result of the residual gas ionization in the drift chamber: (*I*) vacuum arc discharge plasma; (*II*) residual gas plasma; (*1*) plasma source; (*2*) plasma expansion chamber; (*3*) anode grid; (*4*) accelerating gap; (*5*) cathode grid; (*6*) equipotential drift space; Pt^+ are the beam ions and i^+, the residual gas ions. Solid curves show the potential profiles for a vacuum gap (φ_I), for the stage of a slow ion transport zone formation (φ_{II}), and for the stationary state (φ_{III}).

1063-7850/03/2907-0572$24.00 © 2003 MAIK "Nauka/Interperiodica"

drift region can transmit an output current j_{out}, which is related to the injected beam current j_{in} by the equation

$$\frac{1}{j_{out}^{1/2}} + \frac{1}{(2j_{in} - j_{out})^{1/2}} = \frac{2}{j_{cr1}^{1/2}}. \quad (1)$$

Here, j_{cr1} is the first critical current equal to the Child–Langmuir current for a gap with the length $d/2$, d being the drift space length [4]. As the injected beam current increases, the j_{out} value asymptotically tends to $j_{cr1}/4$ and, hence, small variations in j_{in} will not significantly influence the output beam current.

It should be emphasized that the above mechanism decreasing the relative amplitude of current fluctuations in such systems is operative only in the quasistationary case, whereby the characteristic time of the injection current variation due to the plasma source instability is much greater than the flight time τ_f required for an ion to travel through the entire drift space:

$$T \gg \tau_f = 7.21 \times 10^{-7} d\left(\frac{m_i}{E}\right)^{1/2}. \quad (2)$$

Here, d is the drift chamber length [cm], m_i is the ion mass [amu], E is the ion energy [eV], and τ_f is measured in seconds.

Systems of ion beam formation with grid control have been studied in [2, 3]. In both studies, a decrease in the amplitude of the beam current fluctuations at the output relative to that at the input was experimentally confirmed despite the fact that condition (2) was not satisfied. On the other hand, the results of our calculations show that the ion current noise in a high-vacuum drift chamber can even increase rather than decrease [5]. At the same time, both experimental investigations [2, 3] showed that the current transmitted through a drift chamber was greater than the limiting value for an equipotential vacuum gap [4]. One possible reason for an increase in the output current can be the plasma formation in the drift chamber as a result of ionization of the residual gas.

In order to study the mechanism of the current noise reduction in the drift chamber of an ion beam source of the type depicted in Fig. 1, we have studied the ion beam transport through an equipotential drift space by numerical modeling using the one-dimensional code Tracks (ES-1D) [5]. The ion transport was simulated, with allowance for the presence of a residual gas plasma, by the method of pellet injection with initial conditions corresponding to the experimental parameters used in [3]. A bunch of platinum ions with an energy of 47 keV and a given angular velocity distribution was accelerated by a voltage of 100–300 V and injected into a 6-cm-long drift chamber. The initial beam current density was varied from 1 μA/cm^2 to several milliamperes per square centimeter within a time period of 50 μs, after which a sinusoidal signal with a

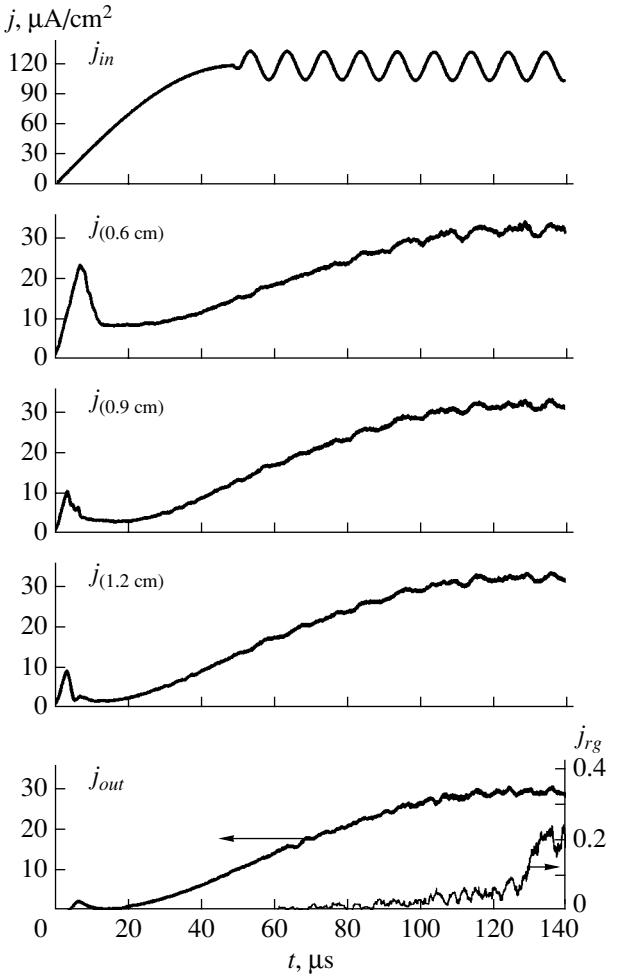

Fig. 2. Simulated time series of (top to bottom) the injected ion beam current j_{in}, the currents $j(x$ [cm]) in intermediate sections of the drift chamber, the output current j_{out}, and the current j_{rg} of residual gas ions. The first peak corresponds to the moment of the virtual anode formation in the drift chamber (at $t \sim 5$–7 μs).

period of 10 μs and an amplitude of $2\Delta j_{in}/j_{in} = 25\%$ was superimposed to model noise in the injected current.

In modeling the plasma formation, it was assumed that secondary electrons were emitted from the drift chamber walls under the action of injected ions. The secondary electron emission coefficient was varied from 10^{-1} to 10^{-3} (electrons per ion). The results of our calculations showed that a potential profile in the drift space represents a potential well for these electrons, in which they can oscillate and produce ionization of the residual gas. According to the experimental conditions studied, the residual gas concentration was varied from 10^{11} to 10^{12} cm^{-3}. The ionization cross section was taken equal to $\sim 10^{-16}$ cm^2, which is the maximum value for molecular hydrogen. The density of oscillating electrons was limited by their recombination with ions of the injected beam and by the loss on the chamber walls. The process of plasma formation was modeled so as to

ensure that the rate of the ion current increase at the output corresponded to that observed in experiment [3].

The results of numerical simulation showed that interaction of the ion beam with the ionized residual gas leads to the formation of a steady-state potential profile in the drift chamber, which can be separated into three characteristic regions (Fig. 1). In region *A*, situated in front of the potential maximum, ions are decelerated in the space charge field, while electrons are accelerated toward region *B*. In region *B*, occurring at a virtual anode potential, electrons are held by this potential, while ions are transported with low energies in the regime of full compensation by the space charge of oscillating electrons (formed both as a result of secondary electron emission from the walls and due to residual gas ionization in regions *A* and *C)*. In region *C*, ions are accelerated toward the system output, while electrons are retarded and returned back to region *B*.

Figure 2 shows the calculated time series of the injected and output currents, as well as the currents in intermediate sections of the beam transport zone. As can be seen, the current noise amplitude decreases in the region of slow ion transport (Fig. 1, region *B*).

For an ion beam with a certain scatter in the particle velocity, the current noise can also decrease as a result of a spatial redistribution of the ion density in the beam. A minimum transport zone length in which the current noise is reduced can be estimated for the condition that fast ions will reach the output simultaneously with the ones possessing an average velocity, injected one period before the former ions. This yields

$$L \geq v_{\max}\frac{v_{\max}+v_{\min}}{v_{\max}-v_{\min}}T, \qquad (3)$$

where L is the beam transport length over which the current noise amplitude is reduced; $v_{\max}$ and $v_{\min}$ are the maximum and minimum ion velocities in the beam; and T is the noise period. Estimates using condition (3) showed that, for the model parameters studied, the beam transport zone length ensuring reduction in the noise must be not less than 1–2 cm, in agreement with the results of numerical simulation.

Thus, under real experimental conditions, ionization of the residual gas leads to a change in the potential profile in the drift chamber and to the formation of a slow ion transport zone responsible for the ion current noise reduction. The mechanism of the current noise reduction is related to a spatial redistribution of the density of ions (in a beam characterized by a significant scatter of velocities) in the slow ion transport zone. Under these conditions, the amplitude of current fluctuations can decrease (Fig. 2) even if the characteristic time of current variations is comparable with the flight time of ions through the drift space, which is confirmed by the experimental data [2, 3].

REFERENCES

1. S. Humphries, Jr., C. Burkhart, S. Coffey, *et al.*, J. Appl. Phys. **59**, 1790 (1986).
2. S. Humphries, Jr. and H. Rutkowsky, J. Appl. Phys. **67**, 3223 (1990).
3. E. Oks, G. Yushkov, I. Litovko, *et al.*, Rev. Sci. Instrum. **73** (2), 702 (2002).
4. R. B. Miller, *Introduction to the Physics of Intense Charged Particle Beams* (Plenum Press, New York, 1982; Mir, Moscow, 1984).
5. V. A. Shklyaev, S. Ya. Belomyttsev, V. V. Ryzhov, and I. Yu. Turchanovskiĭ, in *Proceedings of the 6th International Conference on Modification of Materials with Particle Beams and Plasma Flows, Tomsk, 2002*, p. 631.

Translated by P. Pozdeev

Technical Physics Letters, Vol. 29, No. 7, 2003, pp. 575–577. Translated from Pis'ma v Zhurnal Tekhnicheskoĭ Fiziki, Vol. 29, No. 14, 2003, pp. 8–14.

Application of the Multifractal Concept to Characterization of the Structure of Composite Films of Fullerene C_{60} Doped with CdTe

A. V. Nashchekin, A. G. Kolmakov, I. P. Soshnikov, N. M. Shmidt, and A. V. Loskutov

Ioffe Physicotechnical Institute, Russian Academy of Sciences, St. Petersburg, 194021 Russia
Baikov Institute of Metallurgy and Materials Science, Russian Academy of Sciences, Moscow, 117334 Russia

Received February 11, 2003

Abstract—Peculiarities in the surface morphology of fullerene C_{60} based composite films containing various amounts of CdTe (0 to 100 mass %) were studied using methods of information theory. The characteristic size of the surface structure elements for these films amounts to 150–200 nm. It is shown that the concept of multifractals and the methods of multifractal analysis can be used for a quantitative comparison of the surface topography of such composite films. The multifractal analysis reveals the interval of fullerene based film compositions containing 15–20% CdTe, which corresponds to the most equilibrium conditions of film formation and provides for the most ordered material configuration. It was established that, using films with such compositions, fullerene-containing network nanostructures with a lateral resolution of 250 nm can be obtained by direct electron-beam lithography. *© 2003 MAIK "Nauka/Interperiodica".*

Introduction. After the discovery of fullerenes in 1985 and the subsequent development of their production technology, fullerene-based materials have found increasing application in various fields, including electronics and optoelectronics [1–4]. Fullerenes and related compounds are also promising materials for obtaining nanostructures. In particular, recently we demonstrated [4] that fullerene based films can be used for the creation of two-dimensional photonic crystals. The optical properties of such films can be modified by doping the base material with semiconductor compounds such as CdSe and CdTe [3, 4]. This doping also influences the topography of the film surface, which can be revealed by methods of atomic force microscopy and scanning electron microscopy. However, the quantitative comparison of topographic features on the surface of fullerene films was hindered by the lack of corresponding methods.

A useful approach to the quantitative description of objects with complicated structures in the physics of condensed matter and materials science is offered by information theory, in particular, by methods developed for the multifractal parametrization of structures [5]. This approach essentially supplements the traditional methods and allows properties such as the degree of homogeneity and ordering of the configuration studied as a whole to be quantitatively characterized. Good prospects of the use of multifractal parametrization methods for a quantitative description of the surface topography of film materials for electronic and optoelectronic applications were demonstrated recently [6].

This study was aimed at assessing the possibility and efficacy of using the concept of multifractals for the quantitative characterization of topographic features on the surface of composite films based on fullerene C_{60} doped with various amounts of CdTe (0 to 100 mass %).

Materials and methods. The experiments were performed on C_{60}–CdTe composite films with thickness from 200 to 1000 nm obtained by thermal deposition in vacuum onto GaAs(100) and Si(100) substrates. The samples were prepared in a VUP-5M vacuum stage ("Elektron" Corporation, Sumy) with an effusion source. The substrate temperature during film deposition was 160°C. The initial components were special purity grade fullerene C_{60} (99.98%) and CdTe (99.999%). Prior to being placed into the effusion source, the C_{60}–CdTe mixture was comminuted to a particle size of 1 μm and sintered for 2 h at 300–350°C. The content of CdTe in the $(C_{60})_{1-x}(CdTe)_x$ composition was x = 0, 15, 40, or 100% (pure CdTe).

The surface topography of the film surface was studied on a CamScan Series 4 DV100 scanning electron microscope (SEM). Additional information about the surface topography was obtained by imaging the samples at two different magnifications.

The multifractal characteristics of the surface topography were obtained using an original approach to the multifractal parametrization based on the method of rough division measure generation [5]. Preliminary processing of the SEM micrographs consisted in their approximation by rough images generated by methods of computer graphics. The approximated images were

1063-7850/03/2907-0575$24.00 © 2003 MAIK "Nauka/Interperiodica"

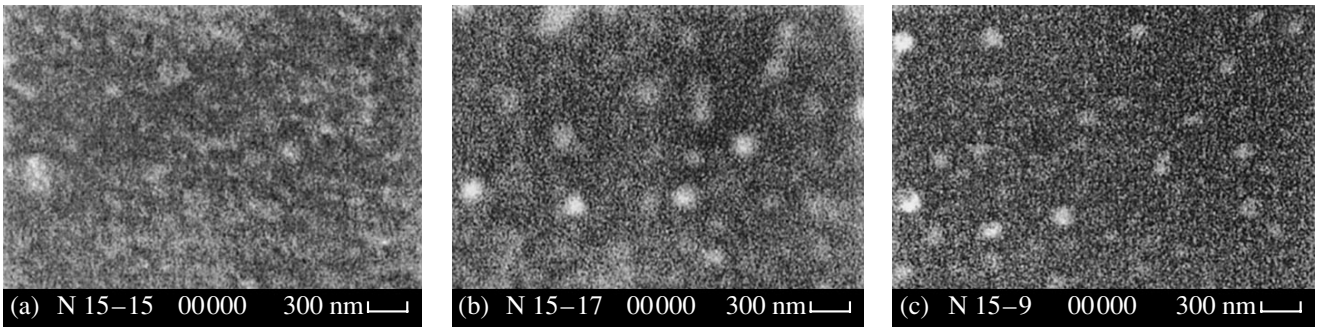

Fig. 1. SEM images showing the surface topography of various films of the fullerene C_{60}–CdTe system: (a) C_{60}–15% CdTe; (b) C_{60}–40% CdTe; (c) 100% CdTe.

obtained using the following procedure: pixels corresponding to the surface protrusions (hills) were assigned measure 1 (white color), while the other pixels were assigned zero (black color) [5]. Thus, multifractal calculations were performed for the black-and-white images of the sample surface topography thus prepared, representing graphic files in the bmp format. The subsequent calculations were performed using a special computer program MFRDrom [5] developed by G.V. Vstovsky.

According to the results of our previous theoretical and experimental investigations [5], parametrization should be performed in terms of quantitative multifractal characteristics such as the generalized entropy (Renyi dimension) D_q with positive q_{max} (in our case, $q_{max} = 100$) and the order parameter Δ_q (with positive q_{max}) determined from "descending" branches of the canonical multifractal spectra and "ascending" branches of the pseudomultifractal spectra. The quantities D_q bear some quantitative information about thermodynamic conditions of the sample structure formation [5]. In some cases, it is possible to ascertain that D_q ($q \gg 1$) increases with the entropy. In connection with this, D_q can be an effective means of recognizing structures indistinguishable (or poorly distinguishable) by traditional quantitative methods. In other words, this characteristic provides for the possibility of recognizing structures formed under identical conditions, on the one hand, and establishing relations with the conditions of structure formation, on the other hand.

The quantity Δ_q reflects the degree of ordering (and symmetry breakage) in the general configuration of the system studied. An increase in the absolute value of Δ_q in the series of structures studied is indicative of an increase in the fraction of a periodic component, the amount of information (negative entropy) "pumped" into the system, and the degree of symmetry breakage [5]. The values of Δ_q obtained from the canonical multifractal and pseudomultifractal spectra reflect somewhat different orders. The parameter Δ_q^c determined from the canonical spectra characterizes the degree of ordering and the symmetry breakage in a macroconfiguration of the system, while the parameter Δ_q^p obtained by the pseudomultifractal calculation reflects local symmetry breakage in a measure of the given structure (determined relative to the multifractal transformation), averaged over the structure [5].

A multifractal analysis consists in studying the distribution of a selected quantity over some geometric carrier. In this study, we have analyzed the distribution of structural elements representing sharp protrusions (hills) of the surface relief on the sample image plane.

Results and discussion. The results of our examination of the surface topography of a fullerene based C_{60}–CdTe composite in a SEM revealed significant changes on the film surface with increasing CdTe content in the system (Figs. 1a–1c). These changes possess a complicated character, which is manifested by coars-

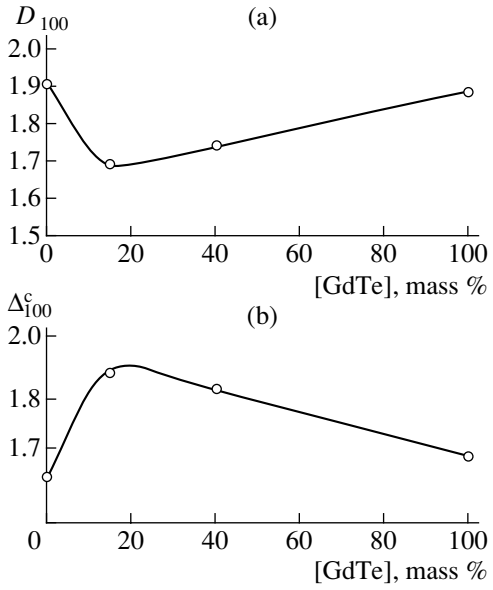

Fig. 2. Relationships between the main multifractal characteristics of the surface topography (calculated in the canonical variant) and composition (mass %) of the fullerene based C_{60}–CdTe composite films.

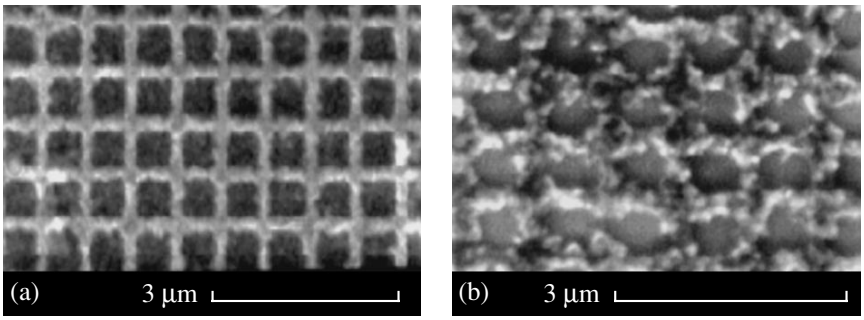

Fig. 3. SEM micrographs of the nanodimensional network structures obtained by electron-beam lithography on fullerene based composite films: (a) C_{60}–15% CdTe (lateral period, 780 nm); (b) C_{60}–40% CdTe (lateral period, 900 nm).

ening of the surface relief and by the clusterization effects. Traditional methods of processing of the SEM images do not allow a quantitative comparison of such trends. We have obtained adequate quantitative characteristics with the aid of multifractal analysis. To this end, the SEM images of C_{60}–CdTe films with variable CdTe content were computer processed and characterized by the Renyi dimension (D_{100}) and the degree of ordering in the whole macroconfiguration (Δ^{c}_{100}).

The plot of D_{100} versus CdTe content in the fullerene based films exhibits a clearly pronounced minimum for the compositions containing 15–20% CdTe (Fig. 2a). Since the parameter D_q bears information about thermodynamic conditions of the sample structure formation [5], this behavior indicates that the composite films with minimum D_q values are formed under the most equilibrium conditions and exhibit the maximum level of structural self-organization.

The plot of the order parameter Δ^{c}_{100} versus CdTe content in the film exhibits a clear maximum (Fig. 2b). These data show evidence of the maximum degree of ordering in the same fullerene based compositions with 15–20% CdTe.

The conclusions derived from the data of multifractal analysis agree well with the results of electron-beam lithography. Using this technique in combination with chemical etching [4], we fabricated nanodimensional network structures with a period of 780 nm using fullerene based films with various CdTe content. The best resolution (~250 nm) was obtained for compositions containing 15–20% CdTe (cf. Figs. 3a and 3b).

Conclusions. (1) The introduction of CdTe into fullerene C_{60} films leads to significant changes in the surface topography, which is manifested by coarsening of the surface relief and by clusterization effects. These changes possess a complicated character, and traditional methods of processing of the SEM images do not allow a quantitative comparison of such trends in films with variable CdTe content.

(2) Using the concept of multifractals and the methods of multifractal analysis, it is possible to perform a quantitative comparison of the surface topography of fullerene based C_{60}–CdTe films with different compositions. This analysis reveals the interval of film compositions corresponding to 15–20% CdTe, which corresponds to the most equilibrium conditions of film formation and provides for the most ordered final material configuration.

(3) The data of the multifractal analysis are well correlated with the results of electron-beam lithography. In the network structures formed by direct electron-beam lithography and chemical etching in C_{60} films doped with CdTe, the best resolution was achieved with compositions containing 15–20% CdTe.

Thus, the first experiments on application of the concept of multifractals and the methods of multifractal analysis to the quantitative characterization of topographic features on a composite film surface gave good results, offering a promising approach to optimization of composite film technology.

Acknowledgments. This study was supported by the Federal Targeted Program "Integration" (project no. B-0101) and by the Joint Russian–Ukrainian Scientific-Technological Program "Research and Development of Nonlinear Optical Switching Structures Based on Fullerene-Containing Composite Materials" (project no. 2000-5F).

REFERENCES

1. M. S. Dresselhaus, G. Dresselhaus, and P. C. Elkund, *Science of Fullerene and Carbon Nanotubes* (Academic, San Diego, 1995), p. 965.
2. *Optical and Electronic Properties of Fullerenes and Fullerene-Based Materials*, Ed. by J. Shinar (Dekker, New York, 1999), p. 392.
3. T. L. Makarova, Fiz. Tekh. Poluprovodn. (St. Petersburg) **35** (3), 257 (2001) [Semiconductors **35**, 243 (2001)].
4. M. E. Gaevski, S. O. Kognovitskiĭ, S. G. Konnikov, A. V. Nashchekin, *et al.*, Nanotechnology, No. 11, 270 (2000).
5. G. V. Vstovsky, A. G. Kolmakov, and V. F. Terentjev, Mater. Sci., No. 2 (9), 62 (1999).
6. A. G. Kolmakov, V. V. Emtsev, W. V. Lundin, *et al.*, Physica B (Amsterdam) **308**–**310**, 1141 (2002).

Translated by P. Pozdeev

Technical Physics Letters, Vol. 29, No. 7, 2003, pp. 578–581. Translated from Pis'ma v Zhurnal Tekhnicheskoĭ Fiziki, Vol. 29, No. 14, 2003, pp. 15–23.

Controlled Magnetoresistance in $Y_{3/4}Lu_{1/4}Ba_2Cu_3O_7$–CuO Composites at 77 K

D. A. Balaev, K. A. Shaihutdinov, S. I. Popkov, and M. I. Petrov

Kirensky Institute of Physics, Siberian Division, Russian Academy of Sciences, Krasnoyarsk, Russia

e-mail: smp@iph.krasn.ru

Received January 28, 2003

Abstract—We have studied the low-temperature magnetoresistance of $Y_{3/4}Lu_{1/4}Ba_2Cu_3O_7$–CuO composites obtained by fast sintering technique and established a relation between the probing to critical current density ratio j/j_c and the shape of the magnetoresistance curve $\rho(H)$. For $j/j_c < 1$, the electric resistance arises at a threshold value of the magnetic field strength H_c. For $j/j_c \geq 1$, a linear variation of $\rho(H)$ at 77 K in the range from 0 to 14 Oe can be provided by selecting the CuO content (in the 15–30 vol % interval) and the j value (in the 0.003–0.2 A/cm^2 range). In the latter case, the slope $d\rho/dH$ (i.e., the sensitivity of the electric resistivity with respect to the magnetic field) is 1–20 mΩ cm/Oe and the relative field-induced increase in the resistivity $\rho_0 = (\rho(H) - \rho(H = 0))/\rho(H = 0)$ amounts to 1320 and 685% at H = 200 and 35 Oe, respectively. Composites possessing controlled magnetoresistance are promising materials for the active elements of magnetic field sensors capable of operating at a practically convenient liquid nitrogen temperature. © *2003 MAIK "Nauka/Interperiodica".*

Previously [1], we presented preliminary data on the magnetoresistance of composites based on high-temperature superconductors (HTSCs). The composites, representing a system of artificial Josephson junctions with a non-HTSC component playing the role of barriers between HTSC grains, possess large magnetoresistance in a broad range of temperatures (below the superconducting temperature T_c of the HTSC component) and relatively weak (below 200 Oe) magnetic fields. This property allows such composites to be used in magnetic field sensors capable of operating at a practically convenient liquid nitrogen temperature.

The effect of magnetic field on the resistance of pure HTSC ceramics was studied shortly after the discovery of the phenomenon of high-temperature superconductivity [2–10]. A strong sensitivity of the resistivity ρ of HTSC materials to a weak external magnetic field is observed in a very narrow temperature interval below T_c. To obtain a significant response at T = 77 K, it is necessary to employ high transport currents (~10^2–10^3 A/cm^2), which encounters considerable technical difficulties related to the heat removal from current-carrying leads [3, 5]) and strong magnetic fields (H ~ 10–60 kOe). The magnetic field hysteresis of the electric resistance [4, 6, 7, 9–11] and the nonlinear character of the $\rho(H)$ function [3–7, 11] also restrict the possible applications of magnetoresistive HTSC ceramics.

Below we report the results of a thorough investigation of the magnetoresistance $\rho(H)$ at various transport current densities j in a series of composites based on yttrium ceramics and copper oxide. The parameters of the magnetoresistance observed at 77 K in these HTSC–CuO composites show more optimistic prospects for the practical use of such materials in magnetic field sensors.

The samples of composites were synthesized from an HTSC composition $Y_{3/4}Lu_{1/4}Ba_2Cu_3O_7$ (referred to below as YBCO) and copper oxide CuO by fast sintering technique as described previously [1, 12]. The samples were annealed according to the following schedule: 2 min at 910°C, 3 h at 350°C, and cooling down to room temperature with the furnace. The X-ray diffraction measurements confirmed the absence of foreign phases in the final composites. We have synthesized and studied the samples of two different compositions denoted below as YBCO + 15 vol % CuO and YBCO + 30 vol % CuO (with an HTSC component fraction of 85 and 70 vol %, respectively).

The electric resistivity as a function of the temperature, $\rho(T)$, and the magnetic field strength, $\rho(H)$, was studied by a standard four probe technique using samples with typical dimensions of $1 \times 2 \times 12$ mm. The distance between the potential contacts was ~10 mm and the probing (transport) current density was varied in the range from 0.002 to 0.2 A/cm^2 (which corresponds to a total current of ~0.1–10 mA). The superconducting state (R = 0) was detected to within ~10^{-6} Ω cm. The critical current density j_c was determined using the initial part of the current–voltage characteristic according to the conventional criterion of 10^{-6} V/cm [13]. During the magnetoresistance measurements, the magnetic field was applied perpendicularly to the electric current direction. No special measures were taken for shielding the Earth's magnetic field. The magnetization measure-

ments were performed using a vibrating-sample magnetometer [14].

Figure 1 shows the experimental $\rho(T)$ curves of the YBCO + 15 vol % CuO and YBCO + 30 vol % CuO composites measured at 77 K using different values of the probing transport current. All variants of the observed $\rho(T)$ curves can be divided into three types depending on the probing current density (at a given temperature). When the current density is below the critical value, $j < j_c$, there is an interval in which $\rho \leq 10^{-6}$ Ω cm. Only beginning with a certain H_c ($H_c \approx$ 10 Oe for YBCO + 15 vol % CuO at $j = 0.12$ A/cm^2 and $T = 77$ K), for which the given current density is critical, does the resistivity exhibit a nonlinear growth with the magnetic field strength (Fig. 1a, curve *1*). For $j \approx j_c$, the growth of $\rho(H)$ begins at the origin of coordinates (Fig. 1a, curve *2*). Finally, for $j > j_c$, the resistivity varies from a certain zero-field value $\rho(H = 0)$ (Fig. 1, curve *3*) and $\rho(H)$ is a linear function of the field strength in the interval from 0 to 14 Oe with a slope of $d\rho/dH \approx 2.5$ mΩ cm/Oe.

For the YBCO + 30 vol % CuO composition, the critical current j_c (77 K) is below 0.001 A/cm^2 and all the $\rho(H)$ curves measured in the entire interval of probing currents j (Fig. 1b) are similar to curve *3* in Fig. 1a. These $\rho(H)$ plots are also linear in the interval from 0 to 14 Oe, but the slope is $d\rho/dH \approx 17.5$ mΩ cm/Oe.

In the magnetic fields with $|H| \leq 37$ Oe, both composites were characterized by coinciding $\rho(H)$ curves measured when increasing and decreasing the absolute value of the field strength. For greater magnetic field amplitudes, the $\rho(H)$ curves exhibit a hysteresis. Figure 2 shows the pattern of $\rho(H)$ and the corresponding magnetization curve $M(H)$ measured for the same specimen of YBCO + 30 vol % CuO with the field varied in the interval -210 Oe $\leq H \leq 210$ Oe. Note that the behavior of $M(H)$ is typical of HTSC ceramics [11]. The $\rho(H)$ loops are well reproduced in the course of multiply repeated field cycling. The thermomagnetic history can be reset by heating a sample above T_c followed by cooling in a zero field. A comparison of the $\rho(H)$ and $M(H)$ curves shows that the sample resistance is a complicated function of the magnetization.

The results of $\rho(H, j)$ measurements at other temperatures were similar to those presented in Figs. 1 and 2. The ratio of the probing to critical current density, j/j_c, is the main parameter determining the type of the $\rho(H)$ curve. Figure 3 shows the temperature dependence of the critical current density $j_c(T)$ in the vicinity of T_c. Using these data and selecting the probing current density, it is possible to predict the shape of the $\rho(H)$ characteristic of a given magnetic field sensor for any temperature in the range studied. In ceramics with natural grain boundaries, the values of j_c(77 K) range within 10–250 A/cm^2 [5, 6, 15]. For this reason, $\rho(H)$ curves of various types such as *1–3* in Fig. 1a are more difficult to obtain in pure ceramics than in composites.

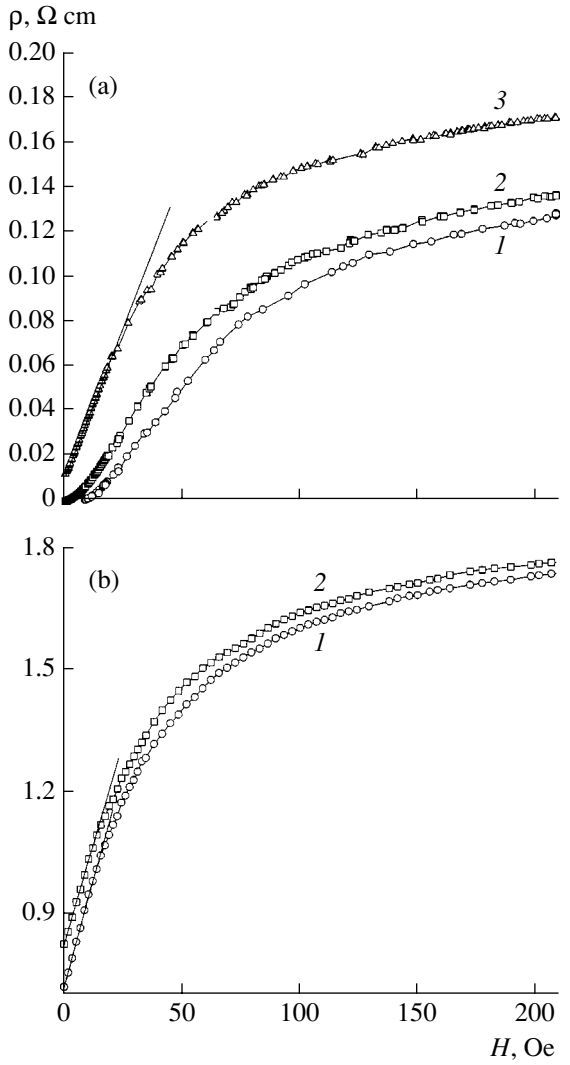

Fig. 1. Plots of the resistivity ρ versus magnetic field strength H at $T = 77$ K: (a) YBCO + 15 vol % CuO composite, $j = 0.037$ A/cm^2 < j_c (*1*), $j = 0.12$ A/cm^2 ≈ j_c (*2*), and $j = 0.37$ A/cm^2 > j_c (*3*); (b) YBCO + 30 vol % CuO composite, $j = 0.0032$ (*1*) and 0.032 A/cm^2 (*2*).

The phenomenon of magnetoresistance observed in polycrystalline HTSCs (including composites) is explained by the fact that these materials represent a system of Josephson junctions. The boundaries between the HTSC grains are weak bonds of the Josephson type, the electric resistance of which is highly sensitive to external magnetic fields [13]. The number of weak bonds per unit length is very large, on the order of 10^3 per mm for a typical size of superconducting granules reaching ~1.5 μm (according to scanning electron microscopy data). Accordingly, the response of one HTSC–grain boundary–HTSC junction has to be multiplied by this number. In the YBCO–CuO composites studied, copper oxide forms dielectric layers between HTSC grains [12]. By selecting the volume content of components, it is possible to control the

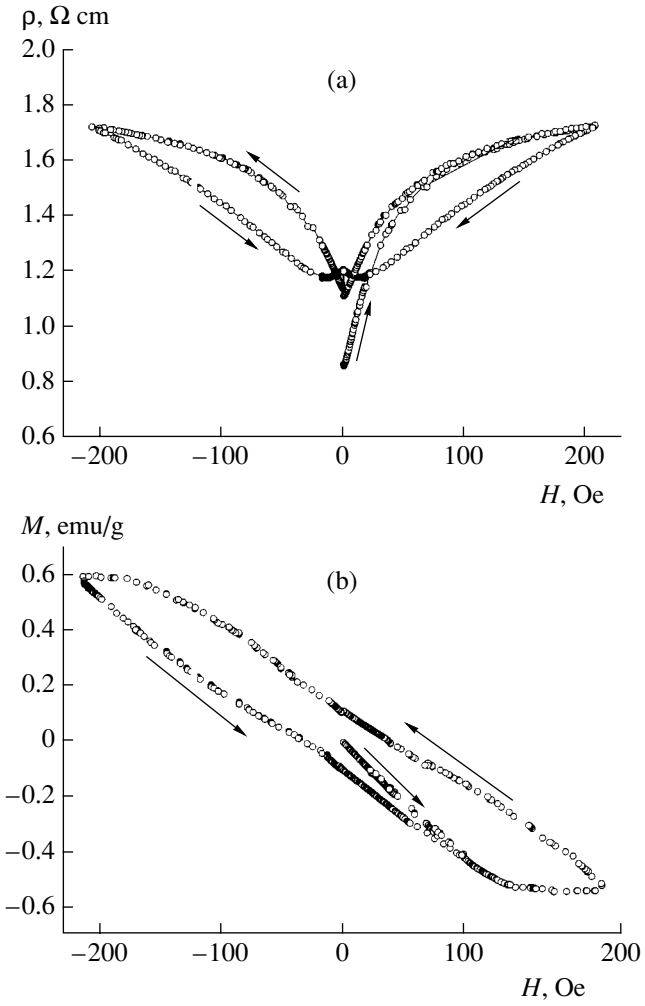

Fig. 2. Plots of (a) the resistivity ρ (j = 0.0032 A/cm^2) and (b) magnetization M versus magnetic field strength H for an YBCO + 30 vol % CuO composite at T = 77 K. Arrows indicate the direction of field variation.

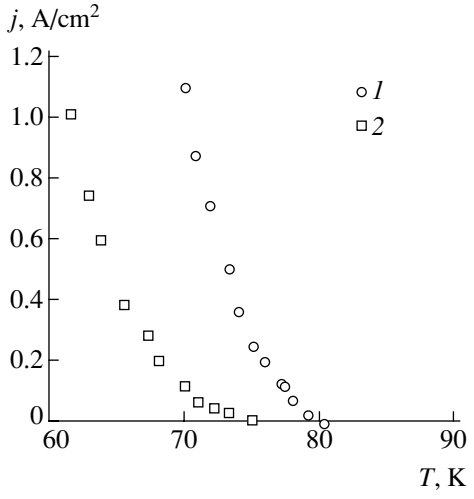

Fig. 3. Plots of the critical current density j_c versus temperature for (*1*) YBCO + 15 vol % CuO and (*2*) YBCO + 30 vol % CuO composites.

"strength" of the Josephson bonds so as to provide that the overall superconducting transition takes place at a preset temperature (in our case, ~80 K for YBCO + 15 vol % CuO and ~76 K for YBCO + 30 vol % CuO). Then, a significant magnetoresistance at 77 K can be observed for relatively weak magnetic fields and low probing current densities. In addition, CuO can be considered as an insulator at low (<100 K) temperatures [16]. This leads to an increase in the resistivity of YBCO–CuO composites in the normal state as compared to that of the pure HTSC ceramics [12]. For this reason, the slope $d\rho/dH$ (i.e., the sensitivity with respect to the magnetic field) obtained in the composites (2–20 mΩ cm/Oe) is greater by at least two orders of magnitude than that in polycrystalline HTSCs (0.01–0.15 mΩ cm/Oe, as estimated from the data reported in [2, 3, 5, 6]).

Another important parameter characterizing the magnetoresistance is the relative field-induced increase in the resistivity $\rho_0 = (\rho(H) - \rho(H = 0))/\rho(H = 0)$, which is the factor by which the resistivity grows upon application of the magnetic field H. Of course, the growth in the resistivity relative to that in the superconducting state (R = 0) is always very large. In practice, it is more important to estimate the resistivity growth relative to a certain finite value of $\rho(H = 0)$. In YBCO + 15 vol % CuO, the value of ρ_0 for $j > j_c$ (Fig. 1a, curve *3*) amounts to 1320% at H = 200 and 685% at 35 Oe (i.e., in the region of reversibility). The zero-field resistivity $\rho(H = 0, T = 77\ \text{K})$ at j = 0.37 A/cm^2 is 8 mΩ cm. In YBCO + 30 vol % CuO, the value of ρ_0 for j = 0.0032 A/cm^2 amounts to 140 and 78% at H = 200 and 35 Oe, respectively, and $\rho(H = 0, T = 77\ \text{K})$ is 725 mΩ cm.

The behavior of $\rho(H)$ such as that depicted in Fig. 1a can be used in devices intended to signal in response to a threshold magnetic field strength H_c. HTSCs materials operating in this regime are called supermagnetoresistors [5]. In out composites, the required H_c value can be adjusted by selecting the volume content of a non-HTSC component and the transport current density.

Thus, the behavior of $\rho(H)$ in the composites under study is determined by the probing (transport) to critical current density ratio j/j_c. For j/j_c, the electric resistance arises at a threshold value of the magnetic field strength H_c. For $j/j_c \geq 1$, there is a region in which $\rho(H)$ is a linear function with a high value of the sensitivity with respect to the field strength: $d\rho/dH$ ~ 1–20 mΩ cm/Oe. The relative increase in the resistivity ρ_0 in the region of reversibility at T = 77 K reaches several hundred percent. The resistivity response to magnetic field in the $Y_{3/4}Lu_{1/4}Ba_2Cu_3O_7$–CuO composites studied (at relatively low values of the probing current, j ~ 1 mA/cm^2) is two orders of magnitude greater than that in pure polycrystalline HTSC ceramics. All these results are indicative of good prospects for using these composites in the active elements of magnetic field sen-

sors capable of operating at a practically convenient liquid nitrogen temperature. In the region of reversible magnetoresistance ($|H| \leq 37$ Oe), the characteristics of such sensors (ρ_0, $d\rho/dH$, $\rho(H)$) are comparable with those of the best devices based on magnesium oxide [17].

Acknowledgments. The authors are grateful to A.F. Bovina for the X-ray diffraction analysis of composites, to A.D. Balaev for his help in conducting magnetic measurements, to D.M. Gokhfeld for his help in work and discussion of results, and to S.V. Komogortsev for fruitful discussions.

This study was supported in part by the Joint Program "Yenisei" of the Krasnoyarsk Regional Science Foundation and the Russian Foundation for Basic Research (project no 02-02-97711) and by the Siberian Division of the Russian Academy of Sciences within the framework of the Lavrentiev Competition of Young Scientist Projects 2002.

REFERENCES

1. D. A. Balaev, D. M. Gokhfeld, S. I. Popkov, *et al.*, Pis'ma Zh. Tekh. Fiz. **27** (22), 45 (2001) [Tech. Phys. Lett. **27**, 952 (2001)].
2. M. A. Dubson, S. T. Herbet, J. J. Calabrese, *et al.*, Phys. Rev. Lett. **60**, 1061 (1988).
3. T. Ohnuma, T. Kuroko, and M. Ishii, in *Proceedings of International Superconductivity Electronics Conference (ISEC-89), Tokio, 1989*, pp. 206–209.
4. S. Shifang, Z. Yong, P. Guoquiang, *et al.*, Europhys. Lett. **6**, 359 (1988).
5. H. Nojima, S. Tsuchimoto, and S. Kataoka, Jpn. J. Appl. Phys. **27**, 746 (1988).
6. Ya. V. Kopelevich, V. V. Lemanov, É. B. Sonin, *et al.*, Fiz. Tverd. Tela (Leningrad) **30**, 2432 (1988) [Sov. Phys. Solid State **30**, 1402 (1988)].
7. M. A. Vasyutin, A. I. Golovashkin, N. D. Kuz'michev, *et al.*, Preprint No. 85, FIAN im. P.N. Lebedeva AN SSSR (Lebedev Physical Institute, Academy of Sciences of USSR, Moscow, 1990).
8. A. C. Wright, K. Zhang, and A. Erbil, Phys. Rev. B **44**, 863 (1991).
9. A. V. Mitin, Physica C **235–240**, 3311 (1994).
10. A. V. Mitin, Sverkhprovodimost: Fiz. Khim. Tekh. **7**, 62 (1994).
11. N. D. Kuz'michev, Pis'ma Zh. Éksp. Teor. Fiz. **74**, 291 (2001) [JETP Lett. **74**, 262 (2001)].
12. M. I. Petrov, D. A. Balaev, K. A. Shaihutdinov, *et al.*, Supercond. Sci. Technol. **14**, 798 (2001).
13. A. Barone and G. Paterno, *Physics and Applications of the Josephson Effect* (Wiley, New York, 1982; Mir, Moscow, 1984).
14. A. D. Balaev, Yu. V. Boyarshinov, M. M. Karpenko, *et al.*, Prib. Tekh. Éksp. **3**, 167 (1985).
15. M. I. Petrov, D. A. Balaev, B. P. Khrustalev, *et al.*, Physica C **235–240**, 3043 (1994).
16. B. A. Gizhevskiĭ, A. A. Samokhvalov, N. M. Chebotaev, *et al.*, Sverkhprovodimost: Fiz. Khim. Tekh. **4**, 827 (1991).
17. É. L. Nagaev, Usp. Fiz. Nauk **166**, 833 (1996) [Phys. Usp. **39**, 781 (1996)].

Translated by P. Pozdeev

Technical Physics Letters, Vol. 29, No. 7, 2003, pp. 582–585. Translated from Pis'ma v Zhurnal Tekhnicheskoĭ Fiziki, Vol. 29, No. 14, 2003, pp. 24–32.

Near IR Diffuse Reflectance Spectroscopy for *in situ* Monitoring of the Degree of Oxidation of $YBa_2Cu_3O_{7-x}$ Powders

V. N. Kuznetsov* and A. A. Lisachenko

Institute of Physics, St. Petersburg State University, St. Petersburg, Russia

** e-mail: kuznets@photonics.phys.spbu.ru*

Received December 24, 2002

Abstract—We have studied the evolution of the diffuse reflectance spectra of $YBa_2Cu_3O_{7-x}$ powders with $0.1 \le x \le \sim 1.0$ in the spectral interval of 0.5 eV$\le h\nu \le$ 6.0 eV. Combination of the optical spectroscopy with thermal desorption measurements revealed a band at 1.25 eV that reversibly varied in the redox cycle. This band, assigned to interband absorption in the CuO_2 planes with low coordination of Cu(2), can be used for *in situ* monitoring of the degree of oxidation of $YBa_2Cu_3O_{7-x}$ powders with $x \ge 0.5$. © *2003 MAIK "Nauka/Interperiodica".*

Dependence of the optical spectra of $YBa_2Cu_3O_{7-x}$ (YBCO) on the oxygen content was established long ago [1, 2]. This discovery allowed the optical spectroscopy to be used both for studying the nature of high-temperature superconductivity and for nondestructive monitoring of the oxygen deficit (measured by the x value). Single crystals and compact ceramics are successfully studied using the specular reflectance technique, but the ceramic samples have to be polished so as to obtain a specular reflecting surface. This technique cannot be used for measuring the spectra of powders *in situ*. The specular reflectance spectra of powders are virtually unstudied because of the low amplitude of the reflected signal. Amplification of the signal would allow exclusion of the sample preparation stage and use of the diffuse reflectance component.

This study was aimed at assessing the possibility of using the diffuse reflectance spectroscopy for *in situ* monitoring of the degree of oxidation of YBCO powders in the course of thermal treatment in vacuum and in oxygen.

The spectra of the diffuse reflectance (DR) $\rho(h\nu)$ were studied in the spectral interval of 0.5 eV $\le h\nu \le$ 6.0 eV. The measurements were performed on a Beckman Model 5270 spectrophotometer with an integrating sphere and $BaSO_4$ reference. A sample of YBCO powder was placed into a quartz cell provided with a means of pumping to ultrahigh vacuum, controlled gas admission, and the temperature and pressure monitoring. The measurements of thermal desorption (TD) were performed in the spectrophotometric and mass-spectrometric [3] systems. The experiments were mostly performed on an YBCO powder with $x \approx 0.1$ synthesized at the Institute of Physics (St. Petersburg State University) by sintering component oxides.

Figure 1 shows the DR spectra of the initial YBCO powder (curve *1*) and the powder calcined at 1200 K in air (curve *1a*) in comparison to the typical spectra of ceramics from various batches (curves *2* and *2a*). Spectra *1* and *1a* show a monotonic increase in $\rho(h\nu)$ in the region of $h\nu < 2$ eV and exhibit bands with maxima at 2.4–2.5, 4.5–4.6, and 5.2–5.3 eV. The same features

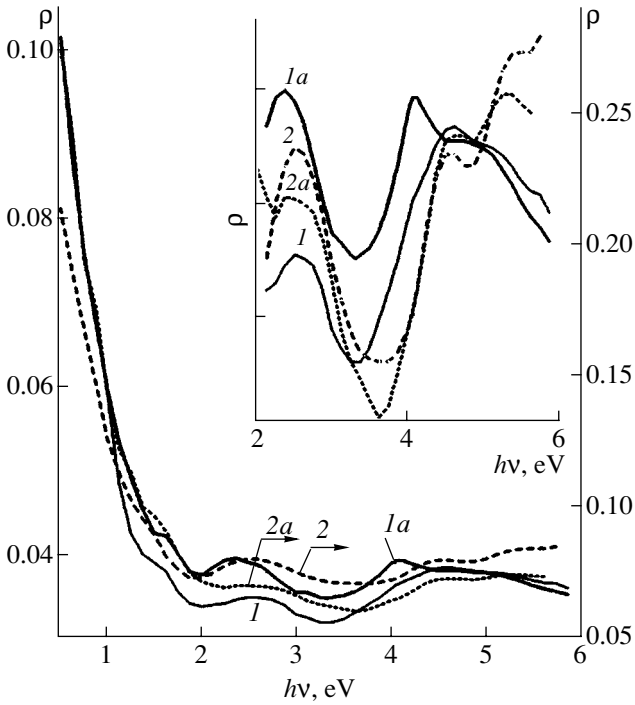

Fig. 1. Diffuse reflectance spectra of YBCO: (*1*, *1a*) powder; (*2*, *2a*) ceramics. The spectra in the inset are shifted along the abscissa axis. See the text for explanations.

1063-7850/03/2907-0582$24.00 © 2003 MAIK "Nauka/Interperiodica"

are present in the DR spectra of ceramic samples. This pattern is also characteristic of the specular reflectance spectra of polished compact ceramics [1, 2] and YBCO single crystals [4]. Indeed, the specular reflectance spectra of single crystals display bands at 2.78, 4.52, and 5.32 for the **E** || **a** polarization and 2.84, 4.62, and 5.3 eV for the **E** || **b** polarization [4]. Upon calcination at 1200 K in air followed by rapid cooling, the DR spectrum exhibits an additional band at ~4.1 eV (Fig. 1, curve *1a*), which is also present in the specular reflectance spectra of polished YBCO ceramics and single crystals with $x \geq 0.5$ [1, 2, 4]. Thus, the DR spectra of powders reproduce all the main features of the specular reflectance spectra of single crystals and polished ceramics.

Figure 2 compares the DR spectra of an YBCO powder measured in air (curve *1*) and upon heating to various temperatures in vacuum (curves *2–4*). As can be seen, heating to 290 K in vacuum suppresses the intensity of reflection at $h\nu < 1.5$ eV. This can be explained by the removal of oxygen, leading to a decrease in the density of free electrons. As a result, the Drude reflectance decreases and the plasma reflectance boundary shifts toward lower energies. Heating to 290 K < $T \leq$ 740 K in vacuum weakly modifies the spectrum (Fig. 2, curve *2*), but increasing the temperature to $T = 900$ K results in the appearance of bands at 1.3 and 4.1 eV (curve *3*). Upon heating to $T = 1000$ K (curve *4*), the band at 1.25 eV becomes predominant. Thus, the growth of reflectance at 1.25 and 4.1 eV in the course of heat treatment in vacuum repeats the pattern of changes observed in the specular reflectance spectra of YBCO single crystals and polished ceramics with $x \geq 0.5$ [1, 2, 4].

Taking into account that a band in the near infrared (NIR) region begins to dominate in the DR spectrum of oxygen-deficient powders, we have thoroughly studied the behavior of this band in the course of heat treatment of the YBCO powder in vacuum and in oxygen. Figure 3 (curve *1a*) shows a change in the NIR band intensity ($\Delta\rho_{NIR}$) plotted versus temperature for the YBCO powder heated in vacuum. The $\Delta\rho_{NIR}$ value was calculated as a difference of the ρ values at 1.25 eV in the DR spectra measured in vacuum at room temperature and after heating to a given temperature. As can be seen, the intensity of the NIR band starts growing at $T \approx 800$ K. According to the results reported in [5] (reproduced in the inset in Fig. 3), this treatment corresponds to $x \approx 0.5$. For the same *x*, a NIR band was also observed in the specular reflectance spectra of YBCO ceramics [1, 2].

Figure 3 (curve *3a*) also shows a TD curve of oxygen, representing the oxygen desorption rate V_d for a mass peak with $m/e = 32$ amu versus *T* measured in a linear heating regime. As can be seen from a comparison of curves *1a* and *3a*, the NIR band appears simultaneously with the onset of oxygen desorption at 835 K. Previously, one or two weakly resolved peaks at 730–770 and 820– 870 K observed in the spectra of O_2 thermodesorption from YBCO [6, 7] were attributed to the oxygen release from an orthorhombic phase. The appearance of the NIR band in the specular reflectance spectra of YBCO ceramics was explained by the transition of YBCO from orthorhombic to tetragonal phase [1, 8]. A peak observed in the TD spectrum of YBCO at ~1020 K was also assigned to the tetragonal phase [5, 6]. Thus, the conditions of appearance of the NIR band in our DR spectra agree with the known dependence of this signal on the parameter *x* and with changes in the YBCO structure.

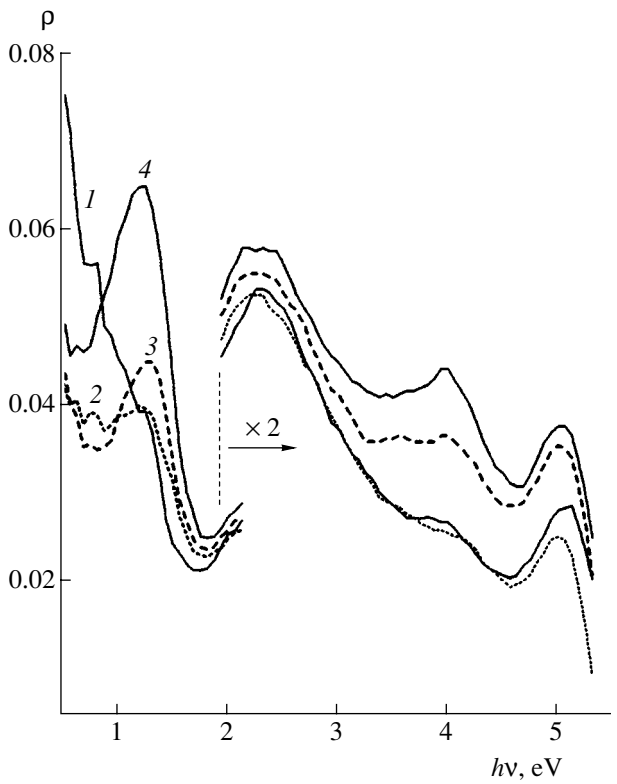

Fig. 2. Diffuse reflectance spectra of YBCO powders (*1*) before and (*2–4*) after heating in vacuum at (*2*) 290 K ≤ $T \leq$ 740 K, (*3*) 900 K, and (*4*) 1000 K.

We have also studied variation of the NIR band intensity in the course of repeated oxidation of the YBCO powder in oxygen at $P = 100$ Torr. Figure 3 (curve *2*) shows the $\Delta\rho_{NIR}$ value as a function of the temperature of 25-min heating in oxygen for a powder preliminarily annealed at 1000 K in vacuum. As can be seen, the NIR band is almost completely removed by annealing in oxygen ($P = 100$ Torr) at a temperature in the interval 400 K ≤ $T \leq$ 580 K. In addition, a sample annealed in vacuum at 1000 K was used to measure the temperature variation of the oxygen absorption rate V_a (determined as $V_a = dP/dt$) in the course of heating in oxygen at $P = 0.1$ Torr (Fig. 3, curves *4a* and *4b* representing the 1st and 3rd heating cycles, respectively). The V_a versus *T* curves show that $T \approx 400$ K is a threshold temperature for the oxygen absorption from the gas

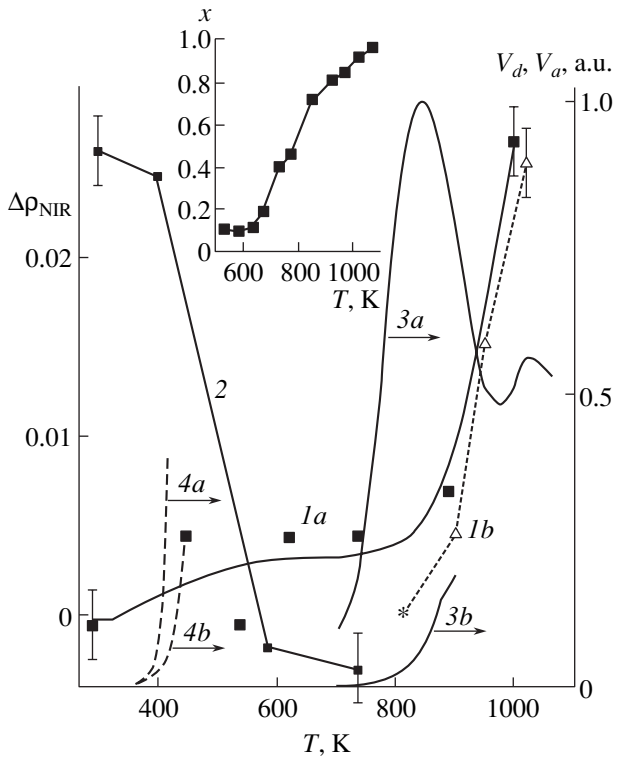

Fig. 3. (*1a*, *1b*, *2*) Plots of a change in the NIR band intensity ($\Delta\rho_{NIR}$) versus the temperature of a 30-min annealing of YBCO powders (*1a*, *1b*) in vacuum and (*2*) in oxygen; (*3a*, *3b*, *4a*, *4b*) the temperature variation of the rate of oxygen (*3a*, *3b*) desorption (V_d) and (*4a*, *4b*) absorption (V_a) from an YBCO powder heated at a rate of β = 0.1 (*3a*, *3b*) and 0.3 K/s (*4a*, *4b*); oxygen pressure P = 100 (*2*), 0.1 Torr (*4a*, *4b*). The inset reproduces the plot of x versus annealing temperature from [5]. See the text for explanations.

phase. The results of TD measurements using ^{18}O isotope showed that this temperature corresponds to the onset of intense oxygen incorporation into the YBCO structure [3]. Therefore, these data show the possibility of spectroscopic monitoring of the variable oxygen content in the YBCO structure in the course of exchange with the gas phase provided there is reversible variation of the NIR band intensity in the redox cycle.

In addition, Fig. 3 (curve *1b*) shows a plot of the NIR band intensity versus temperature of heating in vacuum for a sample preliminarily oxidized by annealing in oxygen. Before the measurement of curve *1b*, the part of the oxygen corresponding to the peak at 850 K was removed in the course of TD measurements. For this sample, the oxygen desorption is observed at $T \geq$ 800 K (Fig. 3, curve *3b*) and the NIR band intensity corresponds to the point of curve *1b* denoted by the asterisk. Subsequent points on this curve were obtained in the course of 30-min heating at increased temperatures in vacuum. A comparison of curves *1b* and *3b* in Fig. 3 shows that the growth in the NIR band intensity is related to the removal of oxygen from the YBCO structure in course of transition to the tetragonal phase at $T >$ 800 K. Thus, the NIR band exhibits reversible variation in the redox cycles of YBCO powder. Removal of the structural oxygen at $T \geq$ 800 K leads to the appearance of the NIR band, while the absorption of oxygen at $T \geq$ 400 K results in vanishing of this band.

Let us consider the nature of the band at 1.25 eV. The NIR band is assigned to an optical transition with charge transfer between the $p\sigma_x$ and $p\sigma_y$ bands of oxygen and the d_{x2-y2} band of copper belonging to the CuO_2 planes [8–11]. The appearance of this band is explained by the removal of oxygen from Cu(1)O(1) planes and the structural transition to a tetragonal phase. In this state, the YBCO crystal is a dielectric with populated O2*p* and vacant Cu3*d* bands. The corresponding variations in the reduced density of states are manifested both in the absorption spectra and in the reflectance spectra. At the same time, no data were reported on the conditions of annealing of the NIR band in the course of YBCO oxidation. We have established that the NIR band vanished upon annealing the powder in oxygen in a rather narrow temperature interval 400 K < $T \leq$ 580 K (Fig. 3, curve *2*). Investigations of the ^{18}O isotope diffusion into YBCO ceramics at T = 600–720 K showed that the diffusant initially occupies the O(1) and O(5) positions in the structure [12]. The diffusion of oxygen into powders was also studied at lower temperatures ($T \geq$ 523 K) [13]. Our estimates based on the data reported in [13] show that the oxide layer formed for 25 min at T = 500 K and P = 760 Torr has a thickness of ≤30 nm. Thus, the vanishing of the NIR band in the course of annealing of the YBCO powder in oxygen is related to occupation of the O(1) sites and reconstruction of the initial orthorhombic phase in a thin near-surface layer.

The position of the NIR band maximum in the reflectance spectra of ceramics and thin films varies from ~1.4 to ~1.7 eV [1, 2, 14, 15], depending on the number of oxygen atoms coordinated to Cu(2) [8, 9]. For N = 6 in La_2CuO_2 with two apical oxygen atoms O(4) forming an octahedron with oxygens in the CuO_2 plane, the NIR band is peaked at 2.0 eV; for N = 5 in a pyramidal cell of $LaGdCuO_4$, the band has a maximum at 1.7 eV; and for N = 4 in the cells of Nd_2CuO_4 and $CaCuO_2$ deprived of the apical oxygen atoms, the peak shifts to 1.5 eV [8, 9]. The maxima at 1.7–1.8 and 1.4–1.5 eV are also observed in the spectra of induced photoconductivity in oxygen-deficient YBCO [16, 17]. In [17], the maximum at 1.4–1.5 eV was attributed to absorption by photoelectrically active defects in the CuO_2 planes at the grain boundaries. It should also be noted that a NIR band at 1.5 eV was observed in the specular reflectance spectra of a tetragonal YBCO phase formed at the boundary of the twinning regions [18]. Thus, the maximum of the optical absorption of various cuprates in the region of interband transitions in the CuO_2 planes varies within 1.3–1.8 eV. The lower limit

of this range corresponds to absorption at the boundaries of grains and twinning regions, where the coordination of Cu(2) can be lower than that in the bulk. From these considerations, it follows that the band peaked at 1.25 eV in the DR spectra of YBCO powders is due to the interband absorption in the surface (subsurface) low-coordinated CuO_2 planes.

The above results and analysis indicate that the DR band at 1.25 eV can be used for *in situ* monitoring variations in the content of oxygen during the formation and breakage of the orthorhombic phase in YBCO powders. The DR measurements require no sample preparation, allow integration of the reflected light in a large solid angle, and make possible variations in the arrangement of sample and detector relative to the probing beam. A convenient source of the probing radiation is offered by a Nd laser operating at $h\nu = 1.14$ eV.

Conclusions. (1) The diffuse reflectance spectra of YBCO powders and ceramics in the spectral interval of $0.5\ \text{eV} \le h\nu \le 5.5\ \text{eV}$ reproduce all the main features of the specular reflectance spectra of single crystals and polished ceramics.

(2) The intensity of the NIR band at 1.25 eV in the diffuse reflectance spectra of $YBa_2Cu_3O_{7-x}$ powders is correlated with the parameter x for $x \ge 0.5$, which allows this band to be used for a nondestructive distant *in situ* monitoring of the stoichiometry of YBCO powders.

REFERENCES

1. M. K. Kelly, P. Barboux, J. M. Tarascon, *et al.*, Phys. Rev. B **38**, 870 (1988).
2. J. Humlicek, M. Garriga, and M. Cardona, Solid State Commun. **67**, 589 (1988).
3. V. N. Kuznetsov, Pis'ma Zh. Tekh. Fiz. **27** (10), 1 (2001) [Tech. Phys. Lett. **27**, 394 (2001)].
4. Ya. O. Dovgiĭ, L. T. Karplyuk, I. V. Kityk, *et al.*, Fiz. Tverd. Tela (Leningrad) **32**, 3099 (1990) [Sov. Phys. Solid State **32**, 1798 (1990)].
5. N. V. Kir'yakov, É. A. Grigor'yan, Yu. G. Sikharulidze, *et al.*, Sverkhprovodimost: Fiz. Khim. Tekh. **3**, 1121 (1990).
6. V. V. Semin, A. V. Nazarenko, and S. É. Khabarov, Pis'ma Zh. Tekh. Fiz. **15** (7), 72 (1989) [Sov. Tech. Phys. Lett. **15**, 278 (1989)].
7. M. S. Hegde, Mater. Res. Bull. **23**, 1171 (1988).
8. M. K. Kelly, P. Barboux, J. M. Tarascon, *et al.*, Phys. Rev. B **40**, 6797 (1989).
9. Y. Tokura, H. Takagi, T. Arima, *et al.*, Physica C **162–164**, 1231 (1989).
10. J. M. Leng, J. M. Ginder, W. E. Farneth, *et al.*, Phys. Rev. B **43**, 10582 (1991).
11. S. L. Cooper, D. Reznik, A. Kotz, *et al.*, Phys. Rev. B **47**, 8233 (1993).
12. V. B. Vykhodets, T. E. Kurennykh, K. I. Trifonov, *et al.*, Zh. Éksp. Teor. Fiz. **106**, 648 (1994) [JETP **79**, 355 (1994)].
13. K. Conder and Ch. Kruger, Physica C **269**, 92 (1996).
14. H. P. Geserich, G. Scheiber, J. Geeerk, *et al.*, Europhys. Lett. **6**, 277 (1988).
15. K. Widder, J. Munzel, M. Goppert, *et al.*, Physica C **300**, 115 (1998).
16. S. L. Budko, H. H. Feng, M. F. Davis, *et al.*, Phys. Rev. B **48**, 16707 (1993).
17. W. Markowitsch, C. Stockinger, W. Lang, *et al.*, Phys. Status Solidi B **215**, 547 (1999).
18. M. P. Petrov, A. I. Grachev, M. V. Krasin'kova, *et al.*, Solid State Commun. **67**, 1197 (1988).

Translated by P. Pozdeev

Technical Physics Letters, Vol. 29, No. 7, 2003, pp. 586–588. Translated from Pis'ma v Zhurnal Tekhnicheskoĭ Fiziki, Vol. 29, No. 14, 2003, pp. 33–38.

New Storage Phosphors for Thermal Neutron Detection

A. V. Sidorenko[a,*], P. A. Rodnyi[a], and C. W. E. van Eijk[b]

[a] *St. Petersburg State Technical University, St. Petersburg, 195251 Russia*
e-mail: sidorenkoa@mail.ru

[b] *Delft University of Technology, 2629 JB, Mekelweg 15, Delft, The Netherlands*

Received January 10, 2003

Abstract—The main requirements on neutron detectors based on storage phosphors (SPs) are formulated. It is shown that commercial gadolinium-containing neutron SPs (Gd-SPs) based on mixtures of BaFBr:Eu^{2+} with Gd_2O_3 (a neutron converter) do not possess optimum neutron characteristics because of a high sensitivity to gamma radiation. A comparative study of photostimulated luminescence (PSL) kinetics was performed for samples of halogen-containing borates $Sr_2B_5O_9Br(Cl)$ and $Ca_2B_5O_9Br(Cl)$ activated with Ce^{3+} ions and of the commercial Gd-SPs upon neutron and gamma irradiation. The results suggest that the PSL characteristics of the above borates with 100% content of ^{10}B must be similar to those of Gd-SPs. Use of the halogen borates as SPs offers an advantage to Gd-SPs, because the former neutron detectors are less sensitive to gamma radiation.

The principle of operation of a neutron detector based on storage phosphors (SPs) can be described as follows. The flux of incident particles is absorbed in the active layer of a screen containing SPs in an organic binder matrix. The particles primarily loss their energy for ionization, thus producing electron–hole pairs. In contrast to scintillators, in which the energy of electron–hole pairs is rapidly transferred to the luminescent centers, electrons and holes in SPs are partly trapped. As a result, the secondary emission pattern is modulated by a spatial distribution of the centers capable of trapping the radiation-induced electrons and holes. This (record) stage is followed by the readout procedure, whereby the SP screen is scanned (pixel by pixel) with a focused laser beam. In each element, the laser radiation stimulates the trapped electrons and/or holes to transfer their energy to the emission centers producing the photostimulated luminescence (PSL). The emitted photons are detected by a photoelectron multiplier, whose output is proportional to the ionizing radiation flux absorbed in the given pixel. The overall pattern reproduces a profile of the incident flux intensity.

Screens based on X-ray-sensitive SPs are widely used in medicine (radiography) and in various means of nondestructive monitoring. However, use of such screens for detecting thermal neutrons is still in the stage of experiment. The most promising applications are now expected in the field of neutron diffraction in biological objects [1]. Taking into account the weak intensity of the neutron diffraction, it is necessary to use intense neutron fluxes. A detecting system has to be arranged as close as possible to a nuclear reactor, which is typically characterized by a high level of background gamma radiation. Therefore, SPs intended for detecting neutrons should not be as sensitive to the gamma radiation component, otherwise the image quality will be impaired.

Thus, the main requirements to SPs can be formulated as follows: (i) high absorption coefficient for thermal neutrons; (ii) low sensitivity to gamma radiation; (iii) high efficiency of laser stimulation; (iv) high PSL yield; and (v) slow "discoloration" (fading). The last point is very important, since the time interval between record and readout may exceed one day.

In the past two decades, X-ray radiation was usually detected with the aid of phosphors based on alkali earth halides activated with Eu^{2+} ions. In particular, BaFBr:Eu^{2+} is still the best SP for X-ray detectors. The properties of SPs have been extensively studied, but the proposed mechanisms of carrier trapping and the models of recombination are still rather controversial. According to the most realistic model, electrons are trapped by halogen vacancies with the formation of an F-center while the holes are trapped by Eu^{2+} ions with the formation of a trivalent ion. As a rule, a red laser stimulates the emission of electron from F^- centers; these electrons recombine with adjacent holes (trapping centers) to produce a blue emission typical of Eu^{2+} ions [2]. However, screens intended for detecting X-rays cannot be used in neutron detectors because of a lack of sensitivity to these particles.

Commercial gadolinium-containing neutron-sensitive phosphors (Gd-SPs) are obtained by mixing BaFBr:Eu^{2+} with Gd_2O_3 (a neutron converter). However, high effective atomic charge (Z_{eff}) also makes this material highly sensitive to gamma radiation. In practice, this sensitivity can be reduced by replacing both SP and neutron activator components with other compounds possessing lower Z_{eff} values. Alternatively, only

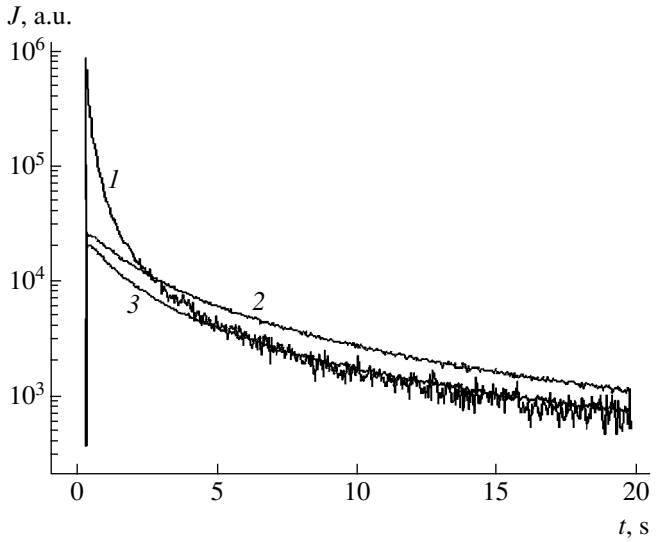

Fig. 1. The kinetics of PSL stimulated by laser radiation (λ = 470 nm) in various SP samples upon preliminary β irradiation: (*1*) Gd-SP; (*2*) $Sr_2B_5O_9Br$:1%Ce^{3+}, Na^+; and (*3*) $Ca_2B_5O_9Br$:1%Ce^{3+}, Na^+. The curve for Gd-SP is corrected for an incomplete overlap of the PSL spectrum (band maximum at 390 nm) and the transmission spectrum of a wideband filter (U-340) used in the photodetector for separating scattered laser radiation; the PSL spectra of halogen-containing borates fully overlap with the filter transmission window.

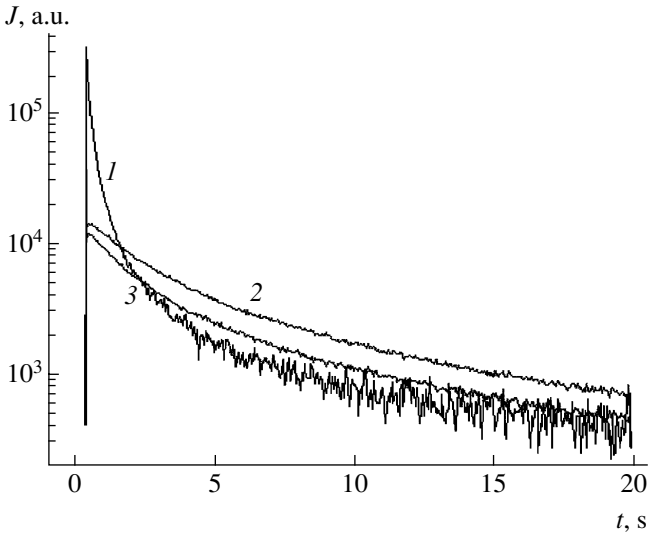

Fig. 2. The kinetics of PSL stimulated by laser radiation (λ = 470 nm) in various SP samples upon preliminary neutron irradiation: (*1*) Gd-SP; (*2*) $Sr_2B_5O_9Br$:1%Ce^{3+}, Na^+; (*3*) $Ca_2B_5O_9Br$:1%Ce^{3+}, Na^+. The curve for Gd-SP is corrected for an incomplete overlap of the PSL spectrum (band maximum at 390 nm) and the transmission spectrum of a wideband filter (U-340) used in the photodetector for separating scattered laser radiation; the PSL spectra of halogen-containing borates fully overlap with the filter transmission window.

a low-Z_{eff} phosphor that contains a neutron-sensitive element in the crystal lattice is introduced. In addition to gadolinium, there are other elements, such as ^{6}Li and ^{10}B, which can be used as neutron converters. Despite possessing the maximum cross section for neutron capture, the Gd-containing SPs are not optimum for neutron detectors because of the aforementioned high Z_{eff}. Selecting ^{6}Li or ^{10}B offers a compromise between large neutron capture cross section and small energy shift in an SP under the action of secondary radiation.

Our investigations are concentrated on halogen-containing borates $Sr_2B_5O_9Br(Cl)$ and $Ca_2B_5O_9Br(Cl)$ activated with Ce^{3+} ions. Some of the samples also contained a coactivator component (singly charged cations $M^+ = Li^+$, Na^+, or K^+) providing for a better solubility of Ce^{3+} ions. The relevant physical characteristics of the SP compositions studied are presented in the table. The energies of α particles and ^{7}Li nuclei released upon the capture of a neutron by ^{10}B are about 40 times that of the corresponding energies of conversion electrons and X-ray quanta in the case of Gd trapping centers. Therefore, the relative intensity of the neutron-induced PSL with respect to the level of emission due to β particles has to be much greater for the borate SPs than for the Gd based systems.

Detailed investigations of the thermoluminescence and PSL in SPs exposed to ionizing radiation of various types included samples of all compositions mentioned above. The curves of the PSL intensity variation under constant laser irradiation provide important information about SPs: the integral PSL yield determines the conversion efficiency of a given SP (i.e., the fraction of ionizing radiation converted into photons), while the PSL kinetics determines the readout rate. The study of fading showed that the PSL intensity after a 4-h storage falls within 46–63% of the initial value measured immediately upon irradiation. For the BaFBr:Eu^{2+}

Calculated values of Z_{eff}, density, and neutron absorption range for SPs studied

SP composition	Density[1], g/cm^3	Z_{eff}	Neutron absorption range[2], mm
$Ca_2B_5O_9Br$	2.03	24.7	0.15
$Sr_2B_5O_9Br$	2.28	32.2	0.17
BaFBr:Eu^{2+} · Gd_2O_3	3.5	56	0.041

Note: [1] The density was calculated using data on the crystal lattice parameters, assuming the grain filling factor to be 0.7; in BaFBr:Eu^{2+} · Gd_2O_3 (Gd-SP), the molar ratio of BaFBr:Eu^{2+} to Gd_2O_3 was assumed to be 1 : 1.

[2] For an incident neutron wavelength of 1.8 Å; the neutron capture cross section was 3837 barn for ^{10}B and 48890 barn for Gd; borate-based SPs were assumed to contain 100% of ^{10}B.

phosphor, this value amounted to 65%. The yield of thermoluminescence for the borate phosphors was on the same order of magnitude as that for $BaFBr:Eu^{2+}$.

Based on the results of our experiments, it was concluded that $Ca_2B_5O_9Cl:Ce^{3+}$ coactivated with Na^+ ions offers a most promising SP for practical applications: this composition possesses high photoluminescent properties and is characterized by the minimum Z_{eff}.

Figures 1 and 2 present comparative data on the PSL kinetics in laser-stimulated samples of halogen-containing borates and Gd-SP. The samples were exposed either to β radiation from a $^{90}Sr/^{90}Y$ source or to a flux of neutrons with an energy corresponding to $\lambda = 1.8$ Å (IRI reactor, Delft). As can be seen, the difference between the PSL yields of halogen-containing borates with a natural content of ^{10}B and that of Gd-SP is approximately the same for both β and neutron irradiation. However, the energy of secondary particles transferred to the phosphor as a result of the (^{10}B, *n*) reaction is 40 times that due to the (Gd, *n*) reaction. The results are explained by lower neutron absorption and higher PSL absorption in an SP layer in the former case. In Gd-SP, photons are predominantly formed in the near-surface layer (because of a greater neutron capture cross section of this material) and, hence, a smaller fraction of these photons is absorbed in the SP layer.

The results of our calculations showed that the level of PSL absorption in Gd-SP is about one-tenth of that in halogen-containing borates. In halogen-containing borates with 100% content of ^{10}B, this absorption has to be twice as small as that in Gd-SP. Therefore, it can be expected that the PSL characteristics of the above borates with 100% content of ^{10}B must be similar to those of Gd-SPs. The results of investigations for such compounds will be published soon.

REFERENCES

1. S. Schweizer, Phys. Status Solidi A **187**, 335 (2001).
2. D. A. A. Myles, C. Bon, P. Langan, *et al.*, Physica B **241–243**, 1122 (1998).

Translated by P. Pozdeev

Technical Physics Letters, Vol. 29, No. 7, 2003, pp. 589–591. Translated from Pis'ma v Zhurnal Tekhnicheskoĭ Fiziki, Vol. 29, No. 14, 2003, pp. 39–45.

Charged Particles Accelerated by Wake Fields in a Dielectric Resonator with Exciting Electron Bunch Channel

V. A. Balakirev, I. N. Onishchenko, D. Yu. Sidorenko, and G. V. Sotnikov*

Kharkov Institute of Physics and Technology, National Scientific Center, Kharkov, Ukraine

** e-mail: sotnikov@kipt.kharkov.ua*

Received January 10, 2003

Abstract—We have studied the acceleration of electrons by wake fields excited in a resonator by a train of electron bunches. The resonator comprised a cylindrical metal waveguide section, containing a dielectric sleeve with a vacuum channel and ends closed by metal walls. Expressions describing the wake field excited by uniformly moving exciting electron bunches have been derived. The self-consistent process of resonator excitation by a train of charged bunches and the particle acceleration in the excited wake field has been numerically simulated. © *2003 MAIK "Nauka/Interperiodica".*

The possibility of accelerating a beam of charged particles by means of a resonator excited by the same beam was studied long ago [1, 2]. Besides theoretical results, there are promising experimental results on the acceleration of electrons in various resonator structures excited by electron beams [3, 4]. However, the previous theoretical descriptions of the excitation of dielectric slow-wave structures by charged particle bunches in wake field schemes ignored the effects related to the presence of longitudinal boundaries in the dielectric structures [5, 6].

When a train of charged bunches propagates in a dielectric waveguide of finite length without reflection at the ends, a wake field wave excited by these bunches is outgoing from the system at a group velocity [7]. This poses a restriction from above on the number of bunches whose wake fields can add in the waveguide. The higher the coefficient of reflection from the ends, the lower the negative influence of the microwave energy loss on the field amplitude. In application to an electron accelerator employing the wake field in a dielectric, the most effective accumulation of the wake field energy from a large number of regular bunches and high-gradient acceleration at a relatively small charge of each bunch can be achieved with dielectric resonators.

Consider a resonator in the form of a round cylindrical metal waveguide section with a length of L_{sys}, partly filled with a homogeneous isotropic dielectric with a vacuum channel for the transport of charged particles. The dispersion function of an infinite waveguide can be written as follows:

$$D(\omega, k_z) = \varepsilon k_v \frac{A_1(k_d a)}{A_0(k_d a)} - k_d \frac{I_1(k_v a)}{I_0(k_i a)},$$

where ε is the relative permittivity; $k_d^2 \equiv k_d^2(\omega, k_z) = \varepsilon\omega^2/c^2 - k_z^2$ (k_d is the radial wavenumber in the dielectric); $k_v^2 \equiv k_v^2(\omega, k_z) = k_z^2 - \omega^2/c^2$ (k_v is the radial wavenumber in vacuum); c is the velocity of light in vacuum; $A_j(x) = N_0(k_d b)J_j(x) - J_0(k_d b)N_j(x)$; N_j, J_j, and I_j are the cylindrical functions of the jth order ($j = 0, 1$); a is the radius of the vacuum channel; and b is the radius of the metal sheath. The roots of the dispersion equation $D(\omega, k_z) = 0$ determine the natural frequencies ω and the longitudinal wavenumbers k_z of the natural waves of the waveguide. The ends of the waveguide are closed with metal walls transparent to charged particles.

Let a bunch of particles bearing a charge q and having the form of a thin ring of radius r_b be injected into the resonator through the entrance wall ($z = 0$) at the moment $t = 0$. The bunch is assumed to propagate uniformly along the waveguide at a velocity of v_b. The charge density distribution in the bunch is described as $\rho = [q/(2\pi r_b v_b)]\delta(r - r_b)\delta(t - t_b - z/v_b)$. Omitting tedious calculations, we present a final expression for the longitudinal electric field excited by such a thin ring-shaped bunch:

$$E_z^{vac}(r, z, t, r_b, t_b) = -\frac{2qv_b}{L_{sys}} \sum_{m=1}^{\infty} \left(\sum_{n=0}^{\infty} \cos(k_n z) \times \frac{\alpha_n \omega_{mn} I_0(k_{v,mn} r_b) I_0(k_{v,mn} r)}{(\omega_{mn}^2 - \omega_n^2) F(\omega_{mn}, k_n)} \times \left\{ \sin[\omega_{mn}(t - t_b)]\theta(t - t_b) - (-1)^n \right.$$

1063-7850/03/2907-0589$24.00 © 2003 MAIK "Nauka/Interperiodica"

$$\times \sin\left[\omega_{mn}\left(t - t_b - \frac{L_{sys}}{v_b}\right)\right]\theta\left(t - t_b - \frac{L_{sys}}{v_b}\right)\Bigg\} \qquad (1)$$

$$+ \sum_{n=1}^{\infty} \cos(k_n z)\frac{2\omega_{mn}^2 I_0(k_{v,mn} r_b)}{\omega_n k_{v,mn}^2 c^2 F(\omega_{mn}, k_n)}\left[\frac{k_n^2(\varepsilon - 1)}{k_{d,mn}^2} I_0(k_{v,mn} a)\right.$$

$$\left. - \frac{k_n^2 c^2 - \omega_n^2}{\omega_{mn}^2 - \omega_n^2} I_0(k_{v,mn} r)\right]\Bigg\{\sin[\omega_n(t - t_b)]\theta(t - t_b)$$

$$- (-1)^n \sin\left[\omega_n\left(t - t_b - \frac{L_{sys}}{v_b}\right)\right]\theta\left(t - t_b - \frac{L_{sys}}{v_b}\right)\Bigg\}\Bigg),$$

where

$$F(\omega, k_z) = \frac{\omega^2 a^2 I_1^2(k_v a)}{2c^2 k_v^2 k_d^2}\left[\frac{4}{\pi^2 a^2 A_1^2(k_d a)}\right.$$

$$\left. - \frac{(\varepsilon^2 k_v^2 + k_d^2) I_0^2(k_v a)}{I_1^2(k_v a)} + \frac{2(\varepsilon k_v^2 + k_d^2) I_0(k_v a)}{k_v a I_1(k_v a)}\right],$$

$\alpha_0 = 1$ and $\alpha_n = 2$ for $n = 1, 2, \ldots$; $k_n = \pi n / L_{sys}$, $\omega_n = k_n v_b$ ($n = 0, 1, 2, \ldots$); $D(\omega_{mn}, k_n) = 0$; $k_{d,mn} \equiv k_d(\omega_{mn}, k_n)$, $k_{v,mn} \equiv k_v(\omega_{mn}, k_n)$; and $\theta(x) = 1$ for $x > 0$ and $\theta(x) = 0$ for $x \le 0$. The field generated by a bunch of finite dimensions is obtained by integrating the elementary field (1) over the bunch volume. In the case of a rectangular charge density distribution in the bunch, the integration result can be expressed in quadratures.

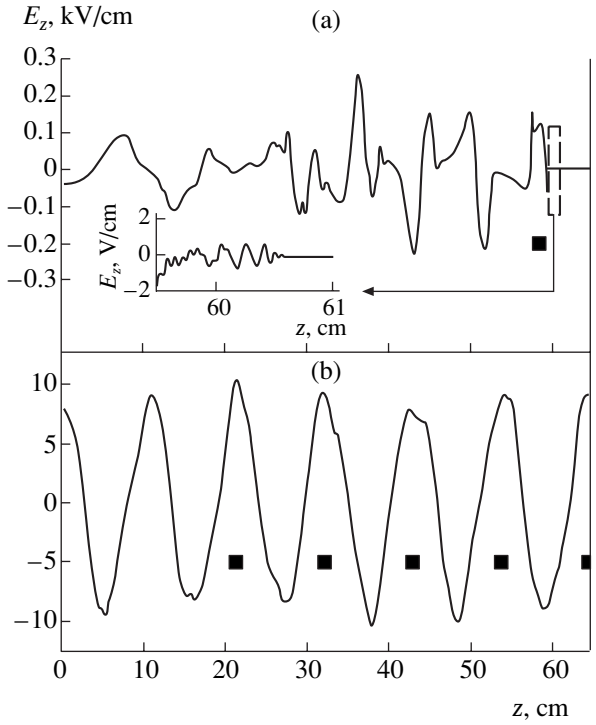

Fig. 1. Longitudinal electric field profile $E_z(z)$ in the resonator (a) for a single bunch and (b) for a train of 200 bunches. The positions of bunches are denoted by black rectangles (the extreme left bunch in the bottom panel is number 200).

We have performed a numerical calculation for a resonator with the following parameters [8]: $L_{sys} = 64.7$ cm; $b = 4.325$ cm; $a = 1.05$ cm; and $\varepsilon = 2.1$. Each electron bunch had an energy of 2 MeV and a rectangular charge density profile with a total charge of –0.32 nC, a length of 1.7 cm, and a radius of 0.5 cm. The bunch repetition period $L_{mod} = 10.78$ cm corresponded to a resonance frequency of the first radial harmonic of the waveguide: $f_1 = 2722.6$ MHz. Note that $L_{sys} = 6L_{mod}$.

Let us consider the results of the numerical calculation of a field generated by charged bunches in the approximation of uniform motion. A single bunch excites a multimode wake field which coincides with the field in a semibounded waveguide [7, 9] (Fig. 1a) until being reflected from the exit wall of the resonator. The rear boundary of the region of an intense wake field follows the bunch at a velocity close to the group velocity of the first resonance harmonic. The presence of a vacuum channel results in the appearance of oscillations at a group velocity equal to the velocity of light in vacuum. These oscillations advance ahead of the electron bunch and form a very weak field precursor [9] (see the inset in Fig. 1a). Excitation of the resonator by a sequence of bunches results, first, in the separation of a resonance harmonic with the frequency equal to the modulation frequency (Fig. 1b) and, second, in a linear growth of the field amplitude with time, in proportion to the number of injected electron bunches. A similar pattern takes place in the infinite system, but the rate of the wake field increase in the finite resonator is smaller than in an analogous segment of the infinite waveguide [6].

A linear increase in the field strength is observed only in the initial excitation stage, where the field amplitude is small. An important mechanism limiting the oscillation amplitude is the reverse action of the intense field on the particles in exciting bunches [10].

To simulate the self-consistent process of excitation of a dielectric resonator by a train of charged bunches and the particle acceleration in the excited wake field, we have developed a special numerical code based on the particle-in-cell algorithm [11]. The model structure geometry corresponded to the problem of bunches uniformly propagating in a resonator, considered above. The numerical experiment was performed with the same parameters of the resonator and bunches as those used in the numerical calculation. In order to provide that the nonlinear effects are manifested before the grid instability development, the charge of a bunch was increased by 20 times to –6.4 nC. The process of acceleration along the system axis was studied by injecting a probing beam. The simulation results were as follows.

After the injection of 300 bunches, the amplitude of the excited field exhibits saturation and the maximum energy of accelerated particles ceases to grow (Fig. 2a). The leading bunches lose energy on the first half of the system length and then are locked by the accelerating

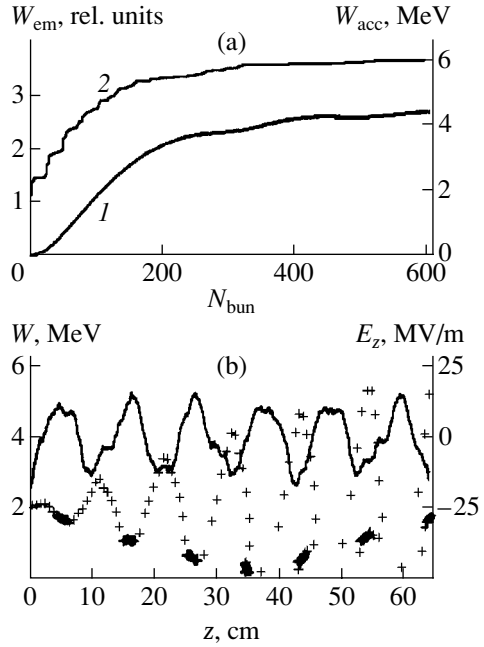

Fig. 2. (a) Plots of (*1*) the electromagnetic field energy W_{em} and (*2*) the maximum energy of accelerated particles W_{acc} versus the number N_{bun} of injected bunches; (b) the "energy W versus coordinate z" phase plane (crosses show the positions of injected macroparticles) and the longitudinal electric field profile $E_z(z)$ on the resonator axis (solid curve) after the injection of 550 bunches.

phase of the wake field and begin to gain energy (Fig. 2b). The bunch energy at the exit only slightly differs from that of the injected bunch. During the flight through the resonator, the phase of particles of the leading bunches performs half an oscillation [10]. The energy of particles injected in the accelerating phase linearly grows as these particles propagate along the system. The maximum energy gain over the resonator length (for the given system parameters) amounts to a double initial energy of the leading bunches. This gain is independent of the exciting beam current: a lower beam current would require injecting a greater number of bunches in order to reach the maximum acceleration gradient. The acceleration rate is 6.15 MeV/m and the number of bunches injected by the moment of saturation is 300, which is comparable in the order of magnitude with the experimental results reported in [8].[1]

[1] As the bunch charge is increased by a certain factor, the field saturation accelerates approximately by the same factor.

Thus, a finite longitudinal size of the dielectric slow-wave structure plays an important role in the dynamics of wake field excitation by trains of relativistic electron bunches. Using the effect of oscillation energy storage in a dielectric resonator, it is possible to significantly increase the electric field strength and reduce the length of a wake field accelerator as compared to the case of a nonreflecting waveguide structure [7]. High-gradient acceleration can be achieved using electron bunches of relatively small charge.

REFERENCES

1. O. A. Kolpakov and V. I. Kotov, Zh. Tekh. Fiz. **34**, 1387 (1964) [Sov. Phys. Tech. Phys. **9**, 1072 (1964)].
2. L. N. Kazanskiĭ, A. V. Kisletsov, and A. N. Lebedev, At. Energ. **30**, 27 (1971).
3. I. A. Grishaev, A. N. Dedik, V. V. Zakutin, *et al.*, Zh. Tekh. Fiz. **44**, 1743 (1974) [Sov. Phys. Tech. Phys. **19**, 1087 (1974)].
4. V. A. Vishnyakov, V. V. Zakutin, V. A. Kushnir, *et al.*, Zh. Tekh. Fiz. **57**, 1549 (1987) [Sov. Phys. Tech. Phys. **32**, 924 (1987)].
5. S. Y. Park and J. L. Hirshfield, Phys. Rev. E **62**, 1266 (2000).
6. T.-B. Zhang, J. L. Hirshfield, T. C. Marshall, *et al.*, Phys. Rev. E **56**, 4647 (1997).
7. V. A. Balakirev, I. N. Onishchenko, D. Yu. Sidorenko, *et al.*, Zh. Éksp. Teor. Fiz. **120**, 41 (2001) [JETP **93**, 33 (2001)].
8. V. Kiseljov, A. Linnik, V. Mirny, *et al.*, in *Proceedings of the 12th International Conference on High-Power Particle Beams, Haifa, Israel, 1998*, Vol. 2, pp. 756–759.
9. V. A. Balakirev, I. N. Onishchenko, D. Yu. Sidorenko, *et al.*, in *Proceedings of the 5th International Workshop "Strong Microwave in Plasmas," Nizhni Novgorod, Russia, 2002*, p. 39.
10. V. I. Kurilko, Zh. Éksp. Teor. Fiz. **57**, 885 (1969) [Sov. Phys. JETP **30**, 484 (1969)].
11. Yu. A. Berezin and V. A. Vshivkov, *Method of Particles in the Dynamics of Rarefied Plasma* (Nauka, Novosibirsk, 1980).

Translated by P. Pozdeev

Technical Physics Letters, Vol. 29, No. 7, 2003, pp. 592–593. Translated from Pis'ma v Zhurnal Tekhnicheskoĭ Fiziki, Vol. 29, No. 14, 2003, pp. 46–49.

Photoconverters Based on GaAs/Ge Heterostructures Grown by Low-Temperature Liquid Phase Epitaxy

V. P. Khvostikov, L. S. Lunin, V. I. Ratushnyĭ, É. V. Oliva, M. Z. Shvarts, and O. A. Khvostikova

Ioffe Physicotechnical Institute, Russian Academy of Sciences, St. Petersburg, 194021 Russia
Volgodonsk Institute (Branch of the Southern-Russia State Technical University, Novocherkassk), Volgodonsk, Russia

Received March 4, 2003

Abstract—A low-temperature liquid phase epitaxy technique involving rapid cooling of a solution melt has been developed for the growth of epitaxial GaAs films on germanium substrates. Using this method, it is possible to obtain high-quality submicron GaAs epilayers on Ge substrates for photoelectric converters. © *2003 MAIK "Nauka/Interperiodica".*

The production of photoelectric converters with limiting parameters is possible only on the basis of heterostructures with submicron epilayers. At present, reproducible synthesis of GaAs/Ge heterostructures for photoelectric converters is performed by methods of metalorganic hydride vapor phase epitaxy. The disadvantage of this process consists in the diffusion of Ga and As atoms from the gas phase into germanium substrates (up to a concentration of ~10^{21} cm^{-3}) during the epitaxial growth stage, which decreases the efficiency of photoelectric converters based on such structures [1]. On the other hand, the synthesis of epitaxial layers of $A^{III}B^{V}$ semiconductor compounds on germanium substrates by liquid phase epitaxy (LPE) encounters difficulties related to some peculiarities of the phase diagrams of Ge-based systems and to the retrograde solubility of germanium in most solution melts used for the LPE of $A^{III}B^{V}$ semiconductors [2, 3].

In order to obtain GaAs epilayers on germanium substrates, we have developed a special LPE procedure involving rapid cooling of a solution melt at a rate of about 2 K/s. It was suggested that such technological conditions provide for the possibility of starting the LPE growth at an initial oversaturation of the solution melt close to the limiting and of conducting the process under significantly nonequilibrium conditions. The germanium substrates are brought into contact with a liquid phase at a relatively low temperature (~400°C), which increases the stability of the interface and suppresses the tendency to dissolution.

The epitaxial growth was performed from a lead-based solution melt. Lead is a neutral solvent and, in addition, is characterized by a minimum solubility of germanium in comparison to other media used for LPE growth. In developing the LPE technology for GaAs, we proceeded from an experimental solubility diagram [4].

It should be noted that, despite a high cooling rate, the growth rate was relatively low ($v \approx 0.05$ μm/s), which allowed the layer thickness to be monitored with a high precision and to obtain high-quality thin (submicron) epilayers.

The GaAs layers grown by the proposed method exhibited mirror-smooth surfaces and had a sharp planar heteroboundary without signs of substrate etching. The parameters of GaAs epilayers were determined by Raman spectroscopy. Figure 1 shows a typical Raman spectrum of a GaAs epilayer grown by the proposed method on a Ge(111) substrate. The spectrum displays two bands with the frequencies corresponding to the natural phonon modes of pure GaAs. The presence of the longitudinal phonon mode is indicative of a sufficiently low content of impurities in the GaAs layer studied.

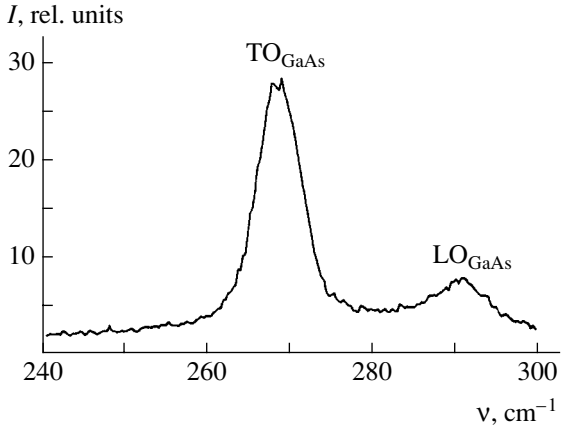

Fig. 1. Raman spectrum of GaAs/Ge(111) structure grown by the proposed method.

1063-7850/03/2907-0592$24.00 © 2003 MAIK "Nauka/Interperiodica"

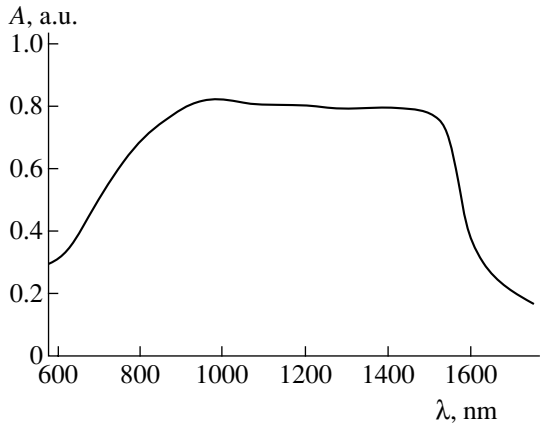

Fig. 2. External quantum yield of a photoelement based on the *p*-GaAs/*p*-Ge/*n*-Ge heterostructure grown by the proposed method.

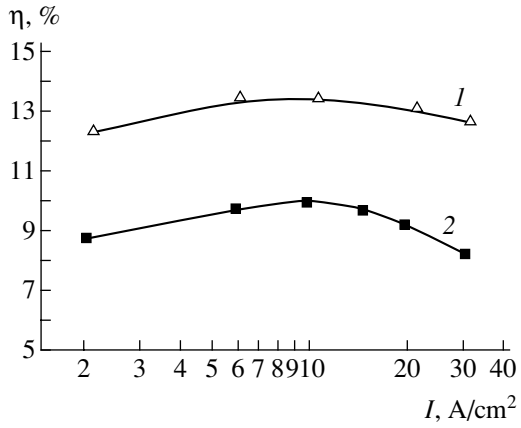

Fig. 3. Plots of the solar energy conversion efficiency (AMO) for the photoelements based on (*1*) a *p*-GaAs/*p*-Ge/*n*-Ge heterostructure and (*2*) a *p*-Ge/*n*-Ge structure.

Based on the GaAs/Ge heterostructure obtained by the proposed method, we manufactured a photoelectric converter by means of diffusion from a gas phase in a quasiclosed volume. The device had an external quantum yield of about 0.8 in the spectral interval from 900 to 1550 nm (Fig. 2), which is evidence of a low density of recombination centers at the *p*-GaAs/*p*-Ge heteroboundary. An increase in the main characteristics of the (*n*–*p*)Ge/*p*-GaAs photoelement, related to a decrease in the surface recombination rate, led to a growth in the efficiency of the solar energy conversion (AMO) from 9–10 to above 13% at a light concentration factor of 100–1000 and a photocurrent density of 3–20 A/cm^2 (Fig. 3).

Thus, the proposed method of low-temperature liquid phase epitaxy, involving rapid cooling of a solution melt, allows high-quality submicron GaAs layers to be obtained on germanium substrates. These heterostructures can be used as narrowband (bottom) elements in combination with a GaAs (top) element to obtain high-efficiency cascade solar cells.

REFERENCES

1. S. Wojtczuk, S. Tobin, M. Sanfacon, *et al.*, IEEE Electron Device Lett. **11** (8), 73 (1991).
2. V. A. Mokritskiĭ and V. S. Shobik, Elektron. Tekh., Ser. Mater., No. 8, 70 (1978).
3. V. M. Andreev, L. M. Dolginov, and D. N. Tret'yakov, *Liquid Epitaxy in the Engineering of Semiconductor Devices* (Sov. Radio, Moscow, 1975).
4. A. Immorlica and B. W. Ludington, Jr., J. Cryst. Growth **51**, 131 (1981).

Translated by P. Pozdeev

Technical Physics Letters, Vol. 29, No. 7, 2003, pp. 594–597. Translated from Pis'ma v Zhurnal Tekhnicheskoĭ Fiziki, Vol. 29, No. 14, 2003, pp. 50–56.

Tunneling Selection of Optical Vortices

T. A. Fadeeva and A. V. Volyar

Tauride National University, Simferopol, Ukraine

Received January 28, 2003

Abstract—We have studied the process of separation of the dominant mode and guided vortices in a Y-shaped directional fiber beam splitter. It is shown that, under certain conditions, the dominant mode field is completely pumped to the second channel, leaving the optical vortex field in this channel unchanged. Based on such a splitter, a vortex fiber interferometer has been created and characterized with respect to linearity and temperature sensitivity. © *2003 MAIK "Nauka/Interperiodica".*

Although optical vortices represent eigenmodes of the ideal round isotropic fiber [1], the excitation and independent propagation of a single guided vortex in a waveguide channel is among the most important problems in singular fiber optics. This situation is caused by two circumstances. The first is related to the eigenmode cutoff conditions, since the same cutoff frequency corresponds to three natural waves of a weakly guiding fiber [2]: *CV* vortex, *TE* mode, and *TM* mode; in addition, the dominant HE_{11} mode exhibits no cutoff at all. Therefore, three "parasitic" modes are excited in a fiber simultaneously with the *CV* vortex. The second circumstance is related to the fiber technology: any (even very small) deviation of the fiber cross section from circular favors the appearance of a geometric birefringence. A significant additional (or even the main) contribution is due to an induced anisotropy of the fiber material, which maintains a single-polarization regime of the dominant HE_{11} mode but breaks a guided vortex [3]. In fact, the *CV* vortex separates into four eigenmodes, with beats arising between these modes. since the propagation constants of these modes are irrational numbers, the initial field state cannot be restored in any cross section of the fiber.

Recently [4], it was demonstrated that, under certain conditions, the latter process can favor restoration of the guided vortex structure. Indeed, a twist of the fiber anisotropy axes in a fiber with large material birefringence stimulates the appearance of a topological Berry phase. If the specific topological phase is significantly greater than the polarization correction to the eigenmode propagation constant, the birefringent action of the medium is suppressed by the twist of axes and a linearly polarized optical vortex becomes an eigenmode of the fiber. By the same token, a circularly polarized optical vortex becomes an eigenmode of a fiber with a twisted elliptical core.

Generally speaking, the first process can also be suppressed or minimized by using fibers with induced absorption distributed in a narrow paraxial region [5]. Then, the losses related to the absorption of HE_{11}, *TE*, and *TM* modes will be significantly greater than those related to the *CV* vortex because of the special structure of the longitudinal and transverse electrical and magnetic fields. However, the technology of such fibers is by no means simple and requires significant correction of a well-adjusted process.

In this context, we addressed another, almost evident possibility of separating a single optical vortex in a fiber channel, not involving modification of the fiber technology. This is the well-known optical tunneling effect, which can influence the behavior of optical vortices and the HE_{11} mode in two closely spaced (coupled) fibers [2] in various ways. The optical tunneling effect is widely used in fiber splitters of the dominant HE_{11} mode but, to our knowledge, no practical applications of this effect to high-order modes have been reported so far.

Here we report the results of investigation of the process of selection of the dominant mode and optical vortices in fiber splitters.

Theory. Consider two weakly guiding fibers with equal core radii ρ and the axes spaced by a distance d (Fig. 1a). To simplify the problem, the fibers are assumed to possess a parabolic profile of the refractive index:

$$\bar{n}^2 = n_{co}^2\left[1 - 2\Delta\left\{\frac{(2x \pm d)^2}{(2\rho)^2} + \frac{y^2}{\rho^2}\right\}\right]. \qquad (1)$$

Here and below, the signs (+) and (–) refer to the first and second fiber, respectively. The excitation conditions and the waveguide parameter V are selected so as to provide that only two circularly polarized (*CV* and

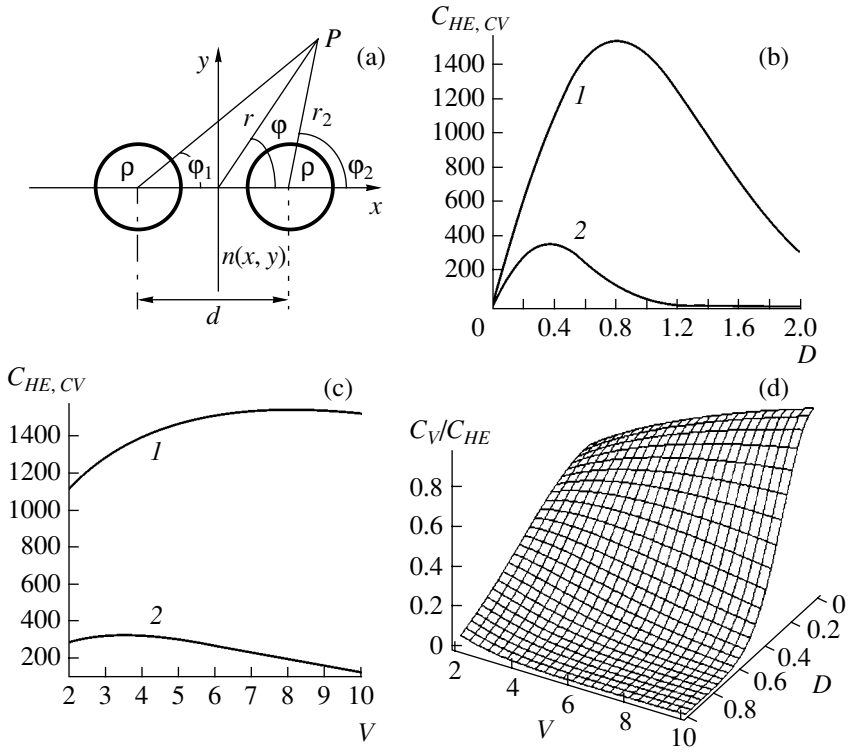

Fig. 1. (a) Coupled optical fibers; (b, c) dependences of the coupling coefficient for (*1*) HE_{11} mode and (*2*) *CV* vortex on the distance between fibers $D = d/\rho$ and the waveguide parameter *V*, respectively; (d) the general shape of the C_V/C_{HE} surface as a function of *V* and *D*.

HE_{11}) modes are excited. The corresponding wave functions can be represented in the following form:

$$\Psi_{HE} = \exp\left\{-\frac{V}{2}R_\pm^2\right\}e^{i\beta_{HE}z},$$
$$\Psi_{CV} = [X_\pm + iY]\exp\left\{-\frac{V}{2}R_\pm^2\right\}e^{i\beta_{CV}z}, \quad (2)$$

where

$$R_\pm = r_{1,2}/\rho = \sqrt{X_\pm^2 + Y^2}, \quad X_\pm = \frac{x \pm \frac{d}{2}}{\rho}, \quad Y = \frac{y}{\rho},$$
$$V = k\rho n_{co}\sqrt{2\Delta}, \quad \Delta \approx \frac{n_{co} - n_{cl}}{n_{co}},$$

n_{co} and n_{cl} are the refractive indices of the fiber core and cladding, respectively; β_{HE} and β_{CV} are the propagation constants of HE_{11} and *CV* modes, respectively.

The coefficient of coupling between the mode fields Ψ_i and Ψ_j can be written as [2]

$$C_{ij} \approx \frac{2\pi}{\lambda}\iint\limits_S (n - \bar{n})\Psi_i\Psi_j^* dS / \iint\limits_S |\Psi_i|^2 dS, \quad (3)$$

where

$$n^2 = n_{co}^2\left[1 - 2\Delta\left\{\frac{(|2x| - d)^2}{(2\rho)^2} + \frac{y^2}{\rho^2}\right\}\right],$$

and the integration is performed over infinite cross section area *S*. Expression (3) shows that the energy exchange is much weaker for modes with different indices than for like modes: $HE_{11} \Rightarrow HE_{11}$ and $CV_{01} \Rightarrow CV_{01}$. Using formulas (1)–(3), we obtain expressions for the coefficients of coupling between like fields:

$$C_{HE} = \sqrt{\frac{V\Delta}{2\pi}}\frac{d}{\rho^2}\exp\left(-\frac{V}{4}\frac{d^2}{\rho^2}\right),$$
$$C_{CV} = \frac{V}{4}\sqrt{\frac{V\Delta}{2\pi}}\frac{d}{\rho^2}\left(\frac{3}{V} - \frac{d^2}{2\rho^2}\right)\exp\left(-\frac{V}{4}\frac{d^2}{\rho^2}\right). \quad (4)$$

When $d < \rho$, the coupling coefficients are comparable ($C_{CV} \propto C_{HE}$); under the condition $Vd^2/2\rho^2 \geq 3$, the coupling between HE_{11} modes is much stronger than that between *CV* vortices ($C_{CV} \ll C_{HE}$). This process is illustrated in Fig. 1b. Initially, the energy exchange between HE_{11} modes in neighboring fibers is almost the same as that between *CV* vortices, but for $d \gg \rho$, the balance is violated and the energy is pumped only

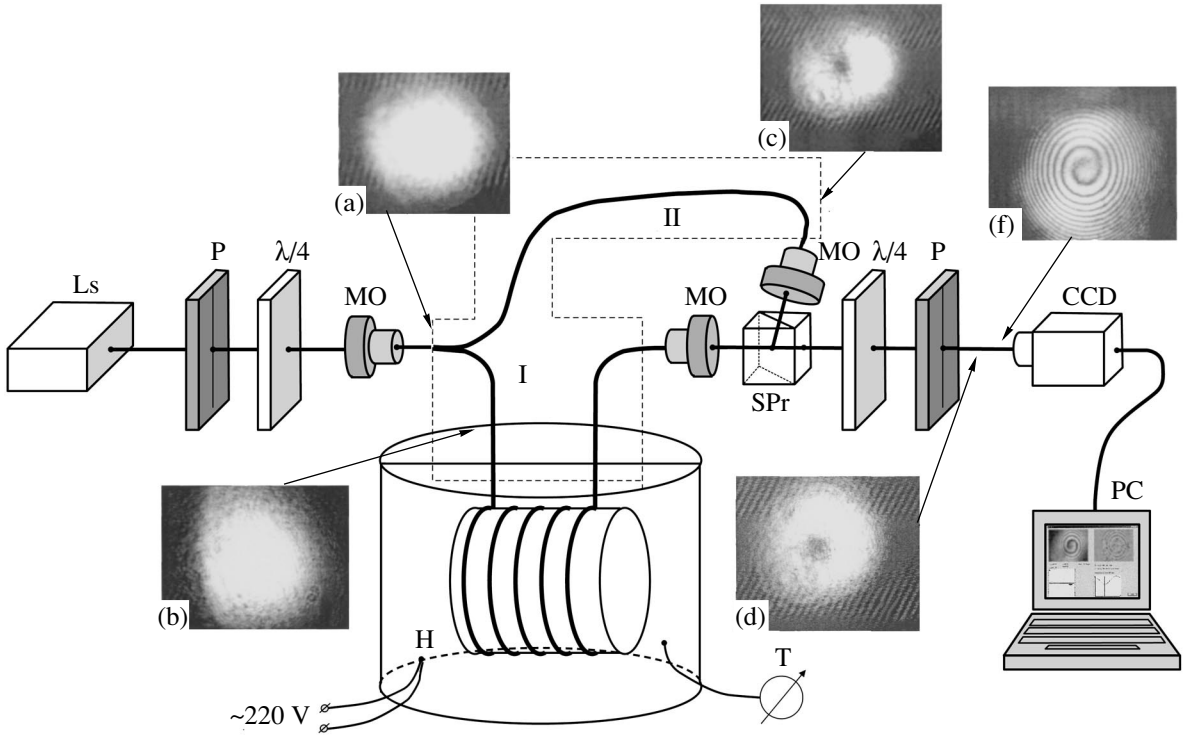

Fig. 2. A schematic diagram of the experimental setup and images showing the beam intensity distributions at various points: (Ls) He–Ne laser; (P) polarizer; (MO) microobjectives; (Spr) beam-splitting prism; (CCD) video camera; (PC) computer. See the text for explanations.

between HE_{11} modes, not involving vortices. However, this condition is not as strict, since the process significantly depends both on the waveguide parameter V and on the relation between V, fiber spacing d, and fiber radius ρ. This circumstance is illustrated in Figs. 1c and 1d. The difference between the coefficients C_{HE} and C_{CV} allows the parasitic HE_{11} mode and *CV* vortex to be separated.

Experiment. We have experimentally studied the process of selection of the dominant HE_{11} mode and *CV* vortex using a Y-shaped directional fiber beam splitter obtained by jointing two standard quartz–quartz fibers featuring the HE_{11} mode at a wavelength of $\lambda = 0.95$ μm. For $\lambda = 0.63$ μm, such fibers allow the excitation of HE_{11}, HE_{21}, *TE*, and *TM* modes by linearly polarized light, while $HE_{11}^{\pm}$, unstable *IV* and stable *CV* vortices can be excited by a circularly polarized light beam [1].

Figure 2 shows a scheme of the Mach–Zehnder fiber interferometer based on the above beam splitter. A circularly polarized light beam was obtained by passing the radiation of a He–Ne laser ($\lambda = 0.63$ μm) through polarizer P and a $\lambda/4$ plate. The beam was focused with a 20× microobjective on the input of the Y-shaped beam splitter. The output ends were connected to the object arm (I) and reference arm (II) of the interferometer. The object arm was 1.7 m long and passed via a reservoir with water. The reference arm had the same length and was arranged in a thermostat (Fig. 2, dashed contour). Using 20× microobjectives and a beam-splitting prism, the light from both fibers was collected in a single beam and passed through a system comprising a $\lambda/4$ plate and polarizer P with axes making an angle of 45° (circular polarization filter). Then the beam was detected by a CCD camera (Samsung, 720×540 working cells) and the interference image was processed by a computer.

A nonparaxial circularly polarized beam excited a mixture of modes in the first fiber, including the HE_{11} mode and *IV* and *CV* vortices with uncontrolled "weights" (Fig. 2a). Owing to the difference in the coupling coefficients for the HE_{11} mode and vortices (the *CV* vortex and *TE* and *TM* modes, whose superposition yields the *IV* vortex, possess equal coupling coefficients), the HE_{11} mode energy was almost completely pumped to the object arm I (Fig. 2b), while the energy of the *CV* and *IV* vortices in reference arm II remained virtually unchanged. This is clearly illustrated by Fig. 2c, showing the position of the field singularity (black spot). Even at a 1 : 1 ratio of the energies of the HE_{11} mode and vortices, the singularity is displaced out from the visible zone. In our case, the black spot occurs almost at the center; inhomogeneous polarization of the reference beam is evidence of the presence of the *IV* vortex with the circulation direction opposite to that of the *CV* vortex. The polarization filter was adjusted so as to

suppress the *IV* vortex field. Indeed, the filtered beam (Fig. 2d) added with the reference beam formed a spiral pattern (Fig. 2f) characteristic of the interference field of an optical vortex.

A change in the temperature of water in the reservoir led to rotation of the interference spiral. The rotating image was computer-processed on a real time scale as described in [6]. It was found that the rotation angle is directly proportional to the liquid medium temperature. The temperature sensitivity of this fiber interferometer was 189 rad/(K m) at an absolute error of determination of the rotation angle 0.015 rad. This sensitivity is comparable with that of single-mode interferometers [7], but a broad linearity range characteristic of vortex interferometers is an obvious advantage of the proposed device.

Acknowledgments. The authors are grateful to G.D. Basiladze for kindly providing the fiber beam splitter manufactured using a method developed at the DOMEN Construction Bureau (Tauride National University, Simferopol).

REFERENCES

1. A. V. Volyar and T. A. Fadeeva, Pis'ma Zh. Tekh. Fiz. **22** (8), 63 (1996) [Tech. Phys. Lett. **22**, 333 (1996)].
2. A. W. Snyder and J. D. Love, *Optical Waveguide Theory* (Chapman and Hall, London, 1983; Radio i Svyaz', Moscow, 1987).
3. K. N. Alekseev, A. V. Volyar, and T. A. Fadeeva, Opt. Spektrosk. **93**, 639 (2002) [Opt. Spectrosc. **93**, 588 (2002)].
4. C. N. Alexeyev and A. V. Volyar, Proc. SPIE **4607**, 71 (2002).
5. A. V. Volyar and T. A. Fadeeva, Pis'ma Zh. Tekh. Fiz. **28** (3), 42 (2002) [Tech. Phys. Lett. **28**, 102 (2002)].
6. T. Fadeyeva, D. Kurabtzev, A. Volyar, *et al.*, Proc. SPIE **4607**, 83 (2002).
7. J. D. C. Jones and D. A. Jackson, Anal. Proc. **22**, 207 (1985).

Translated by P. Pozdeev

Technical Physics Letters, Vol. 29, No. 7, 2003, pp. 598–601. Translated from Pis'ma v Zhurnal Tekhnicheskoĭ Fiziki, Vol. 29, No. 14, 2003, pp. 57–65.

Thermoelectric Properties of Silicon at High Pressures in the Region of the Semiconductor–Metal Transition

V. V. Shchennikov[a,*], S. Vikt. Popova[a], and A. Misiuk[b]

[a] *Institute of Metal Physics, Ural Division, Russian Academy of Sciences, Yekaterinburg, Russia*

** e-mail: vladimir.v@imp.uran.ru*

[b] *Institute of Electron Technology, Al. Lotnikow 32/46, PL-02-668 Warsaw, Poland*

Received February 20, 2003

Abstract—The thermo emf in Czochralski grown silicon single crystals annealed at 450°C was experimentally studied in a range of pressures up to 16 GPa in a chamber with synthetic diamond anvils. There is a correlation between the curves of thermo emf versus pressure, the semiconductor–metal transition pressure, and the mechanical properties (microhardness, compressibility) of samples with various oxygen content. The values of thermo emf in the high-pressure metallic phases have been determined. *© 2003 MAIK "Nauka/Interperiodica".*

Investigations into the properties of silicon at high pressures are currently of importance because this material is widely used in tensometric devices and pressure sensors and, more recently, in microelectromechanical (MEMS) and microoptoelectromechanical (MOEMS) systems [1]. Silicon single crystals for microcircuits are usually grown by the Czochralski technique. High-pressure processing of this material (Cz–Si) modifies the structure of primary defects related to residual oxygen [2–4]. In the course of thermal treatments, this oxygen (occurring mostly in the interstitials) forms electrically active clusters (thermodonors) and accumulates in electrically inactive precipitates (reaching micron dimensions) in the region of structural defects [2–4]. The state of defects and oxygen in Cz–Si determines both the mechanical properties and the electron structure of silicon crystals [4].

A highly informative method for the investigation of Cz–Si is based on the measurement of thermoelectric properties in a broad range of pressures *P*, including the region 9–16 GPa featuring pronounced changes in the structural and electronic properties [5–14]. In particular, the behavior of the thermo emf *S* characterizes the type and density of charge carriers and allows the pressure corresponding to the semiconductor–metal phase transition to be determined [11–14]. This pressure may also depend on the state of defects in a silicon crystal. The pressure-induced semiconductor–metal transition in silicon, as manifested by thermo emf, was originally reported by one of the authors [14]. It was demonstrated that silicon is characterized by $S \leq +10$ μV/K, which is close to the values reported for high-pressure metallic phases in $A^{II}B^{VI}$ and $A^{III}B^{V}$ semiconductor compounds [15, 16]. Based on these data, Weber *et al.* [17] explained the experimentally observed decrease in thermo emf on point Si contacts (experiments with such contacts are used for studying electron–phonon interactions and determining the phonon density of states). Therefore, the $S(P)$ measurements on Cz–Si samples in a broad range of pressures (up to ~16 GPa) are of considerable interest for solving various technological problems.

This study was aimed mainly at determining the possibility of characterizing the quality of Cz–Si crystals with different residual oxygen concentrations and defect structures by thermoelectric measurements at high pressures.

In recent years, investigations of the behavior of $S(P)$ under hydrostatic compression in the range where silicon features phase transitions have not been conducted. The range of pressures achieved in a chamber with a compressed capsule [18], as well as in chambers with electrical contacts ion-implanted into diamond anvils [19], does not extend above ~10 GPa. A method for the $S(P)$ measurements in a greater range reaching up to 25–40 GPa was developed in [20, 21]. According to this, a quasihydrostatic pressure in a microsample with pressed contacts is created by diamond anvils in a solid medium: a polymer film [21] or catlinite [20].

In this study, the values of thermo emf $S(P)$ and electric resistivity $\rho(P)$ of Cz–Si samples were measured at a variable hydrostatic pressure of up to ~9 and ~16 GPa using high-pressure chambers with hard alloy and synthetic diamond anvils, respectively [14, 20]. The pressure was determined to within 10% using calibration plots constructed based on the results of monitoring phase transitions in reference compounds (ZnSe, CdTe, etc.) [14, 20]. The experiments were performed in two independently calibrated chambers with an anvil diameter of ~0.8–1.0 mm. The samples with dimensions ~$0.2 \times 0.2 \times 0.1$ mm and ~$0.4 \times 0.4 \times 0.2$ mm (for the diamond and hard alloy anvils, respectively) were

placed in catlinite containers playing the role of a pressure-transmitting medium. The temperature gradient was created by heating one of the anvils; the temperature was monitored with the aid of thermocouples fastened at various points on the anvils [22, 23].

The values of $S(P)$ and $\rho(P)$ were measured as described in [14, 20] on an automated setup capable of monitoring and storing data on the pressure (force), temperature difference, sample response signals, anvil displacement (compressive strain of the sample), and some other parameters. Then, these data were transferred via interface to a computer for long-term storage and processing [22, 23]. The errors of determining ρ and S (with neglect of the sample shape variation due to compression) amounted to ~5% and 20%.

The experiments were performed with samples cut from the same Cz–Si(001) wafer. Unannealed samples (A1) were characterized by a high residual oxygen content. Samples A2–A4 were annealed for various periods of time at atmospheric pressure and a temperature of 450°C. The oxygen content was determined by Fourier transform IR spectroscopy (calibration factor, 2.45×10^{17} cm^{-2}) [3]. The properties of initial samples A1–A4 are presented in the table.

The crystal structure of Cz–Si samples A1 before and after treatment at ~9 and ~16 GPa was studied by X-ray diffraction using CuK_α radiation (λ = 1.5418 Å). All samples were characterized by the microhardness H measured on a PMT-3 instrument by indentation for 10 s at a load of 20 g (A1) and 50 g (A2–A4). Unannealed sample (A1) was subject to cleavage when indented at 50 g.

Under the action of external pressure, silicon exhibits a sequence of phase transitions converting the lattice structure from diamondlike to a body-centered tetragonal (β-Sn) phase at 9–11.5 GPa, then to an intermediate orthorhombic phase (at ~13 GPa), and eventually, at ~14–16 GPa, to a primitive hexagonal type [5–10]. The semiconductor–metal transition accompanies the first structural transformation [5, 11–14]. In our experiments, the electric resistance of Cz–Si samples exhibited jumps when the pressure was increased to $P \sim 6$–10 GPa (these data are not presented here). Similar behavior of $\rho(P)$ was previously reported in [5, 6, 24]; variations of the semiconductor–metal transition pressure and the shape of the resistance versus pressure curves depend on the plasticity of the quasihydrostatic medium transferring pressure from the anvils to sample [5, 6, 11, 24]. At the same time, even relatively low hydrostatic compression (to ~1 GPa) produces irreversible changes in silicon samples with a high density of defects [2, 3]. The $\rho(P)$ curves indicated that the semiconductor–metal transition was completed in Cz–Si samples compressed to ~16 GPa in diamond anvils while remaining incomplete upon compression to ~9 GPa in hard alloy anvils.

The initial values of thermo emf determined in diamond anvils for samples A1–A4 were $S \approx +0.60$, –0.40, –0.56, and –0.50 mV/K, respectively. As the pressure increased up to ~7–10 GPa (where the semiconductor–metal transition took place), the thermo emf decreased in absolute value and changed sign in annealed n-Si samples (Fig. 1). The values of the semiconductor–metal transition pressure P_t estimated from the $S(P)$ and $\rho(P)$ curves measured in different anvils are mutually consistent (Fig. 2). In the vicinity of $P \sim 12$ GPa, the $S(P)$ curves exhibited breaks that could be attributed to the next phase transition (Fig. 1) [7–10]. As the pressure was subsequently decreased, the behavior of thermo emf was reversible in hard alloy anvils and irreversible in diamond anvils, where the S value remained positive upon unloading (see the inset in Fig. 1). Investigation of the samples upon unloading showed the appearance of several intermediate metastable phases (e.g., Si-XII at $P \sim 9$ GPa [9, 10] and Si-III at ~ 2 GPa [7–10, 25]). The nonmonotonic variation of $S(P)$ in the course of unloading can be related to the corresponding phase transitions. Upon compression up to ~16 GPa in

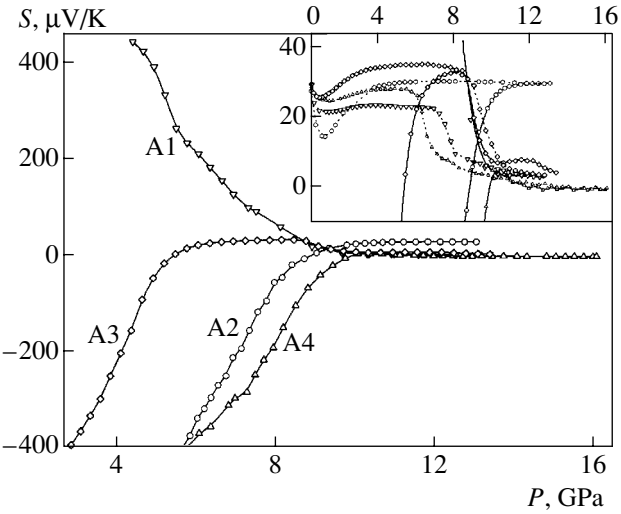

Fig. 1. Plots of the thermo emf S versus quasihydrostatic pressure P for the Cz–Si samples A1–A4 measured at T = 293 K in a chamber with diamond anvils. The inset shows on a greater scale the behavior of $S(P)$ in the vicinity of the semiconductor–metal transition measured on (solid curves) increasing and (dashed curves) decreasing the pressure.

The properties of initial Cz–Si samples at 293 K

Sample type	A1	A2	A3	A4
Annealing time t (450°C), h	0	10	20	40
Charge carrier density $N_{p,n}$, 10^{15} cm^{-3}	1.88 (p-type)	2.2 (n-type)	3.3 (n-type)	5.12 (n-type)
Oxygen content C_0, 10^{17} cm^{-3}	11–11.5	11.3	9.1	10.0

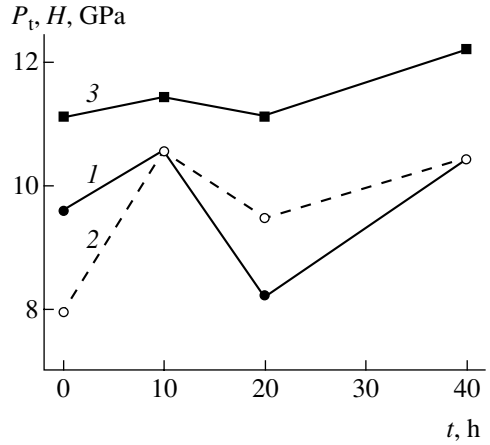

Fig. 2. Effect of the annealing time t on the (*1*, *2*) semiconductor–metal transition pressure P_t determined by a sharp change in the slope of the $S(P)$ curves measured in the diamond and hard alloy anvils, respectively, and (*3*) on the microhardness H of Cz–Si samples.

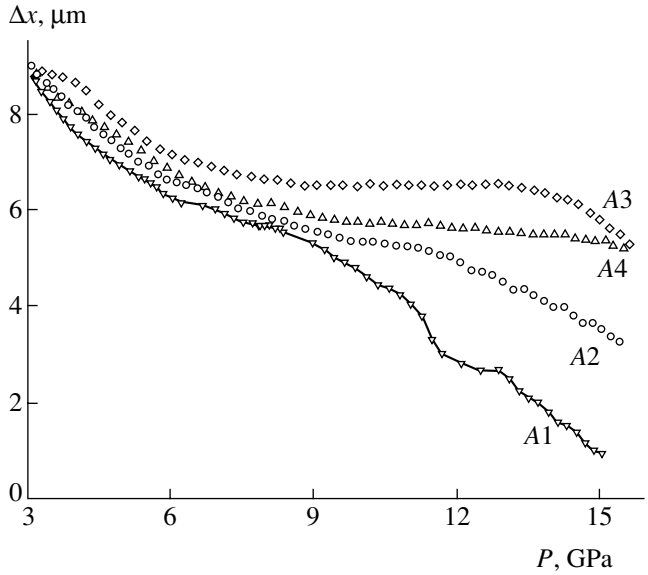

Fig. 3. Plots of the relative displacement Δx versus pressure P for the Cz–Si samples A1–A4 compressed in anvils (the values are reduced by subtracting a linear contribution of $\alpha \times P$, where coefficient α is the same for all samples).

diamond anvils, the samples separated into ~0.04-mm-thick plates parallel to the anvil surface.

The X-ray diffraction study of the samples upon high-pressure treatment showed that silicon loaded to ~9 GPa retained a strongly textured diamondlike structure. The samples loaded up to ~16 GPa exhibited a mixture of the initial phase (I) and a tetragonal phase (Si-IX) with the lattice parameters a = 5.33 Å and a = 7.50 Å, c = 3.87 Å, respectively. Close values a = 7.482 Å, c = 3.856 Å for the Si-IX phase were reported for the samples treated at 12 GPa [25].

The results of microhardness measurements showed that there is a correlation between H and P_t as functions of the thermal treatment duration (i.e., of the residual oxygen content) (Fig. 2). The room-temperature microhardness is approximately equal to the semiconductor–metal transition pressure [26–28]. During the microhardness measurements, material under the indenter really features this transition [27, 28], and it is probable that a change in the defect–oxygen structure similarly influences both H and P_t. It should be noted that no clear relationship between the microhardness and oxygen defects of various types was observed in experiments with microindentation of Cz–Si samples [29–31]. In annealed silicon samples, the decrease in the oxygen concentration in interstitials (see table) is related to the formation of thermoactivated donor centers (supplying electrons to the conduction band) and electrically inactive oxygen precipitates [29–31]. Based on the results reported in [29–31] and the data on the electron density variation with the annealing time (see table), we may conclude that oxygen precipitates have a maximum concentration in sample A3 (with the minimum concentration of interstitial oxygen). In this sample, a change in the sign of S and the semiconductor–metal transition take place earlier than in the other annealed samples (Fig. 1). The difference in the mechanical properties of silicon samples is also manifested by the plots of anvil displacement (compressive strain of the sample) versus pressure (Fig. 3). The maximum compression takes place in the initial *p*-type sample, for which the $\Delta x(P)$ curve exhibits a jump (Fig. 3); according to [5–10], a pressure-induced volume jump upon the transition to a phase with the β-Sn structure amounts to about 10%.

The above data unambiguously indicate a relationship between $S(P)$, the mechanical properties (represented by P_t and H), and the oxygen content in Cz–Si. For example, the lower P_t and H, the earlier the $S(P)$ value changes sign (Fig. 1). The behavior of thermo emf in compressed samples is more sensitive (than the behavior of mechanical characteristics such as P_t and H) to a change in the content of oxygen (and the related defects). This allows high-pressure thermoelectric measurements to be used for testing Czochralski grown silicon single crystals with different oxygen content upon annealing in various regimes, which can be important for various silicon device technologies.

Acknowledgments. The authors are grateful to N.Yu. Frolova and V. P. Sazonova for their help in conducting X-ray diffraction measurements.

This study was supported by the Russian Foundation for Basic Research, project no. 01-02-17203.

REFERENCES

1. W. P. Eaton and J. H. Smith, Smart Mater. Struct. **6**, 530 (1997).
2. I. V. Antonova, A. Misiuk, V. P. Popov, *et al.*, Physica B **225**, 251 (1996).

3. I. V. Antonova, A. Misiuk, V. P. Popov, *et al.*, Physica B **253**, 131 (1998).
4. V. V. Emtsev, G. A. Oganesyan, and K. Shmal'ts, Fiz. Tekh. Poluprovodn. (St. Petersburg) **27**, 1549 (1993) [Semiconductors **27**, 856 (1993)].
5. S. Minomura and H. D. Drickamer, J. Phys. Chem. Solids **23**, 451 (1962).
6. F. P. Bundy, J. Chem. Phys. **41**, 3809 (1964).
7. H. Olijnyk, S. K. Sikka, and W. B. Holzapfel, Phys. Lett. A **103A**, 137 (1984).
8. Zh. H. Jing, L. D. Merkle, C. S. Menoni, *et al.*, Phys. Rev. B **34**, 4679 (1986).
9. M. I. McMahon, R. J. Nelmes, N. G. Wright, *et al.*, Phys. Rev. B **50**, 739 (1994).
10. M. Hebbache, M. Mattesini, and J. Szefiel, Phys. Rev. B **63**, 205201 (2001).
11. J. M. Mignot, G. Chouteau, and G. Martinez, Physica B **135**, 235 (1985).
12. R. Biswas and M. Kertesz, Phys. Rev. B **29**, 1791 (1984).
13. S. D. Gilev and A. M. Trubachev, Phys. Status Solidi B **211**, 379 (1999).
14. V. V. Shchennikov, Fiz. Met. Metalloved. **67**, 93 (1989).
15. V. V. Shchennikov, A. Yu. Derevskov, *et al.*, in *Book of Abstracts of the 36th European High Pressure Research Group (EHPRG) Meeting* (Catania, 1998), pp. 121–122; Proc. SPIE **3213**, 261 (1997).
16. V. V. Shchennikov, Phys. Status Solidi B **223**, 561 (2001).
17. L. Weber, M. Lehr, and E. Gmelin, Phys. Rev. B **46**, 9511 (1992).
18. L. G. Khvostantsev, L. F. Vereshchagin, and N. M. Uliyanitskaya, High Temp.-High Press. **5**, 261 (1973).
19. D. A. Polvani, J. F. Meng, M. Hasegawa, *et al.*, Rev. Sci. Instrum. **70**, 3586 (1999).
20. I. M. Tsidil'kovskiĭ, V. V. Shchennikov, and N. G. Gluzman, Fiz. Tverd. Tela (Leningrad) **24**, 958 (1982) [Sov. Phys. Solid State **24**, 1507 (1982)].
21. N. Sakai, K. Takemura, and K. Tsuji, J. Phys. Soc. Jpn. **51**, 1811 (1982).
22. V. V. Shchennikov and A. V. Bazhenov, Rev. High Pressure Sci. Technol. **6**, 657 (1997).
23. V. V. Shchennikov and A. Yu. Derevskov, in *High Pressure Chemical Engineering*, Ed. by R. V. Rohr and Ch. Trepp (Elsevier, Amsterdam, 1996), pp. 667–672.
24. O. Shimomura, S. Minomura, N. Sakai, *et al.*, Philos. Mag. **29**, 547 (1974).
25. Y.-X. Zhao, F. Buehler, J. R. Sites, *et al.*, Solid State Commun. **59**, 679 (1986).
26. Yu. S. Boyarskaya, D. Z. Grabko, and M. S. Kats, *Physics of Microindentation Processes* (Shtiintsa, Kishinev, 1986).
27. V. G. Eremenko and V. I. Nikitenko, Phys. Status Solidi A **14**, 317 (1972).
28. I. V. Gridneva, Yu. V. Milman, and V. I. Trefilov, Phys. Status Solidi A **14**, 177 (1972).
29. Y. J. Lee, J. von Boehm, and R. M. Nieminen, Appl. Phys. Lett. **79**, 1453 (2001).
30. K. Jurkschat, S. Senkader, P. R. Wilshaw, *et al.*, J. Appl. Phys. **90**, 3219 (2001).
31. H. Harada and K. Sumino, J. Appl. Phys. **53**, 4838 (1982).

Translated by P. Pozdeev

Technical Physics Letters, Vol. 29, No. 7, 2003, pp. 602–605. Translated from Pis'ma v Zhurnal Tekhnicheskoĭ Fiziki, Vol. 29, No. 14, 2003, pp. 66–73.

Suppressing Pulsed Microwave Signals in a Nonlinear Spin Wave Interferometer

A. B. Ustinov and B. A. Kalinikos

St. Petersburg State Electrotechnical University, St. Petersburg, Russia

e-mail: eivt@eltech.ru

Received February 7, 2003

Abstract—The suppression of S-band microwave pulses in a nonlinear spin wave interferometer was experimentally studied for the first time. The microwave interferometer employed a nonlinear spin wave phase shifter based on an yttrium iron garnet film. A signal representing a periodic sequence of rectangular pulses with a power of up to 2.5 mW passes through the nonlinear interferometer without distortion, while an increase in the pulse power to 13.8 mW results in virtually complete suppression of the pulsed signal. © *2003 MAIK "Nauka/Interperiodica".*

In the past decade, there was a constant interest in the investigation of waveguide integral optical interferometers of the Mach–Zehnder type and the application of such devices for the processing of both analog and digital optical signals (see, e.g., [1, 2]). Such interferometers are implemented according to a two-arm scheme based on Y-shaped splitters and connectors using channel or stripe optical waveguides and the elements controlling phase shift in the interferometer arms. However, it was not until very recently that the interest of researchers was drawn to the development of microwave interferometers employing this scheme [3, 4]. Fetisov and Patton [3] described a linear spin wave interferometer employing magnetostatic spin waves, which was provided with an external feedback circuit and possessed bistable transmission characteristics. More recently, we demonstrated [4] the possibility of creating nonlinear microwave interferometers employing a magnetostatic spin wave and studied the transmission characteristics of such a device measured using a continuous microwave input signal.

The operation of a nonlinear spin wave interferometer (Fig. 1a) is based on the phenomena of interference of high-intensity spin waves and a nonlinear shift of their frequencies in response to changes in the input wave amplitude. A microwave signal entering the device is divided into two waves traveling in the corresponding arms of the nonlinear interferometer. The waves acquire different phase shifts and are added to give the interference pattern. As the input signal power increases, the phase shifts vary and the phase difference between interfering signals changes, thus determining the output signal level. The transmission characteristics of a nonlinear spin wave interferometer for a continuous microwave input signal have the shape depicted in Fig. 1b. As can be seen, the signal is completely suppressed when the power reaches a certain level P'_{in} for which the phase shift between signal traveling in the interferometer arms equals 180°.

In order to assess the possibility of processing digital microwave signals, it is interesting to study a nonlinear spin wave interferometer operating in a pulsed mode, whereby radio pulses of relatively high power are suppressed while the low-power pulses are transmitted through the interferometer without distortion. Our experiments were aimed at studying the suppression of a signal having the form of a periodic sequence of rectangular pulses in a nonlinear spin wave interferometer.

The experimental prototype of a nonlinear spin wave interferometer implemented a bridge scheme with two arms (Fig. 1a). The first arm represents a spin wave

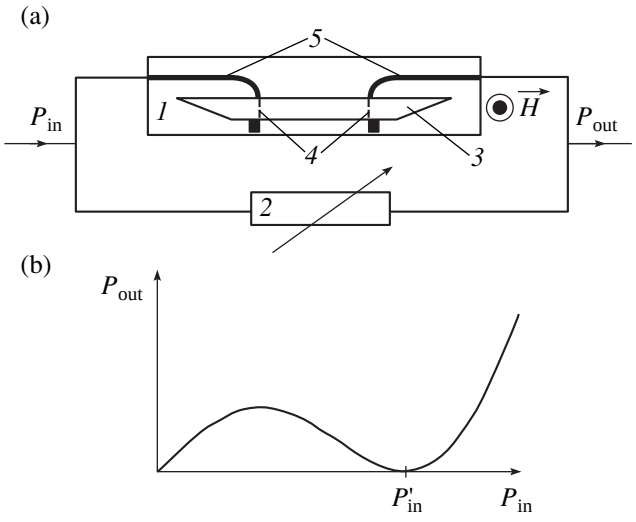

Fig. 1. A nonlinear spin wave interferometer: (a) schematic diagram; (b) transmission characteristic.

1063-7850/03/2907-0602$24.00 © 2003 MAIK "Nauka/Interperiodica"

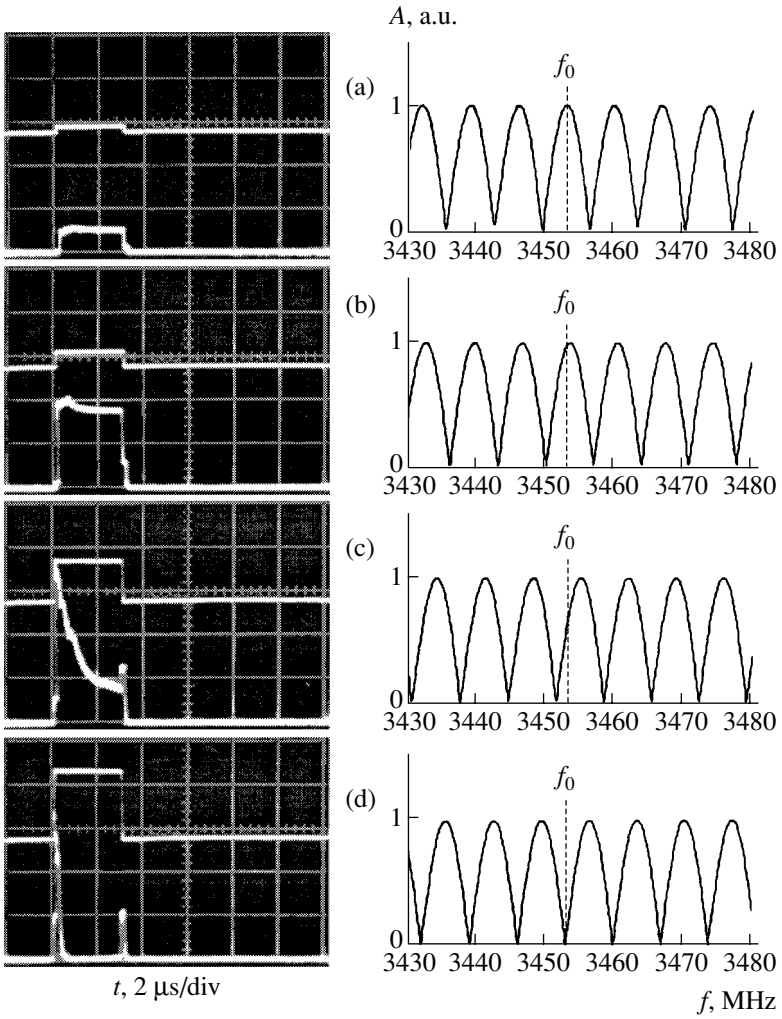

Fig. 2. Oscillograms of the microwave pulse envelopes (left-hand panels) and numerically calculated amplitude–frequency characteristics (right-hand curves) of an experimental prototype of the nonlinear spin wave interferometer for an input pulse power of (a) 0.7, (b) 2.6, (c) 8, and (d) 13.8 mW. The top and bottom oscillograms refer to the input and output microwave pulses.

phase shifter *1*, while the second (reference) arm contains a variable attenuator *2*. The nonlinear phase shifter represented an epitaxial single crystal yttrium iron garnet (YIG) film *3* with a thickness of 5.7 μm and a saturation magnetization of 1750 G, grown on a gadolinium gallium garnet substrate. The spin waves in the YIG film were excited and detected by short-circuited microstrip transducers *4* with a length of 2 mm and a width of 50 μm deposited onto an 0.5-mm-thick alumina (polycor) substrate. The transducers (spaced by 6 mm) were powered via microstrip lines *5* with a wave impedance of 50 Ω. The YIG film was placed on and fixed directly to the microstrip transducers. The phase shifter was exposed to a constant magnetic field (2963 Oe) generated by an electric magnet. The magnetic field vector was perpendicular to the film plane. This orientation corresponded to excitation of the forward volume spin waves, whose phase shift is more sensitive to the input signal as compared to that of the backward reverse volume and surface spin waves. The attenuator was adjusted so as to ensure equal amplitudes of the interfering signals.

The input signal in the form of a periodic sequence of rectangular pulses with a carrier frequency of f_0 = 3453 MHz and a pulse repetition rate of 100 μs was fed to the interferometer input. A part of the input signal power was separated by a directional splitter, attenuated by 20 dB, detected, and fed to the first channel of an oscilloscope. The second channel received a detected signal from the output of the nonlinear spin wave interferometer. The above experimental setup readily detected and displayed changes in the shape of envelopes of the output microwave pulses in response to variation of the input microwave signal power.

The oscillograms in Figs. 2a–2d (left panels) illustrate the suppression of output pulses with increasing input signal power. The top and bottom oscillograms show envelopes of the input and output pulses, respectively. The gains in the channels of the double-beam oscilloscope were different, which accounts for the

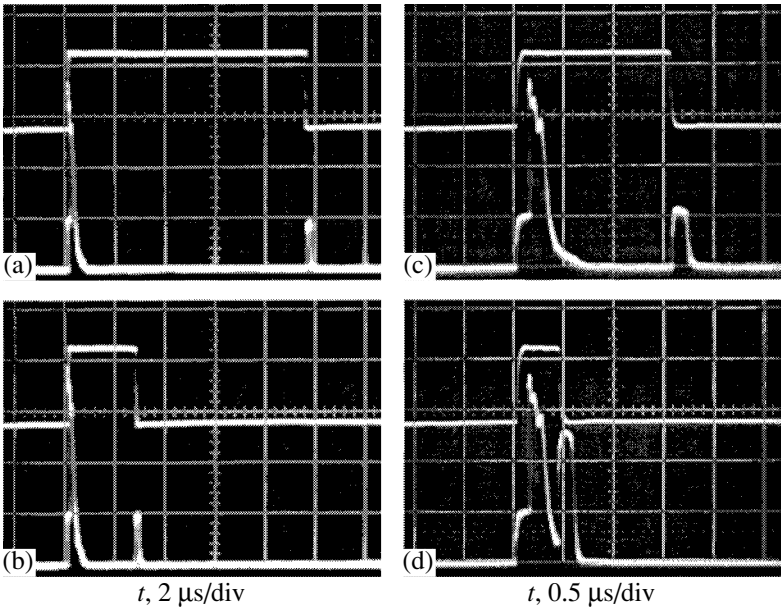

Fig. 3. Suppression of the microwave pulses of various duration in the range from (a) 10 to (d) 0.5 μs in the nonlinear spin wave interferometer.

higher amplitude of the bottom picture. As can be seen from these data, the input microwave pulses of low power (up to about 2.5 mW) reach the output virtually without shape distortions (Figs. 2a and 2b). An increase in the input power level led to a nonlinear shift in frequencies of the carrier spin waves, which resulted in partial suppression of the output signal (Fig. 2c). As the input power reached a level of 13.8 mW, the output pulses were almost completely suppressed (Fig. 2d).

The suppression of microwave pulses observed upon increase in the input signal power is readily explained based on an analysis of the amplitude–frequency characteristic of the nonlinear spin wave interferometer studied. This characteristic was numerically modeled using a formula of adding oscillations, a dispersion law of the forward volume spin waves, and an expression describing a change in the phase shift of the spin waves. The nonlinear phase shift was calculated with allowance for the decrease in the spin wave amplitude during the wave propagation in the YIG film.

The amplitude–frequency characteristics numerically calculated for various values of the input microwave signal power are presented in the right-hand part of Figs. 2a–2d. The alternating maxima and minima correspond to the frequencies of interfering signals added in phase or with opposite phases, respectively. As can be seen from the curves in Fig. 2a, the maximum of the amplitude–frequency characteristic at a low input signal power coincides with the carrier frequency f_0. An increase in the microwave pulse power shifts the characteristic toward higher frequency as a result of the nonlinear change in the spectrum $\omega(k)$ of spin waves with increasing amplitude. When the input signal power reaches a value of 13.8 mW, the amplitude–frequency characteristic shifts so that f_0 corresponds to $A = 0$ (Fig. 2d), which implies that the microwave pulses at the output are virtually completely suppressed.

An analysis of Fig. 2d leads to the following conclusion concerning the possibility of suppressing pulsed microwave signals in a nonlinear spin wave interferometer. If the width of the main lobe in the frequency spectrum of a pulsed microwave signal is smaller than the frequency difference between adjacent maxima of the amplitude–frequency characteristic of the interferometer, the signal is effectively suppressed. In the oscillograms presented in Fig. 2, the microwave pulse duration is 3 μs and, hence, the main lobe width in the signal spectrum was much smaller than the frequency difference (about 7 MHz) between adjacent maxima of the amplitude–frequency characteristic of the interferometer. For this reason, input pulses of such duration are virtually completely suppressed.

As can be seen from Fig. 2, there are short peaks corresponding to the fronts of suppressed microwave pulses. The appearance of both leading and trailing peaks is explained by the different times of signal propagation in the two arms of the interferometer. This was confirmed by numerical calculations of the signal delay time in a nonlinear spin wave phase shifter. The front peak also contains a contribution related to the spin wave nonlinearity development, which accounts for the additional intensity of this peak. The edge peaks are not influenced by the dispersion smearing of the input microwave pulses, which was confirmed by the results of experiments on the suppression of pulses of variable duration (Figs. 3a–3d). These data indicated that the shape and duration of peaks corresponding to the fronts

of suppressed microwave pulses remain unchanged when the input microwave pulse duration changes from 10 to 0.5 μs.

Figure 3d shows that the peaks corresponding to the leading and trailing fronts of suppressed pulses begin to merge when the input pulse duration is decreased to 0.5 μs. Upon further decrease in the input pulse duration, the output signal represented a sequence of two pulses spaced by a time interval equal to the signal delay in the nonlinear phase shifted. Thus, the situation in which the width of the main lobe in the input signal spectrum is greater than the frequency difference between adjacent maxima of the amplitude–frequency characteristic of the interferometer was impossible.

The results of experiments on the suppression of pulses of variable duration (Fig. 3) lead to an important conclusion that the effect of attenuation observed in the nonlinear microwave interferometer is actually related to the intrinsic nonlinearity of spin waves propagating in the YIG film rather than to the film heating as a result of the microwave power absorption. This conclusion is confirmed by the unchanged shape of the edge peaks observed when the input pulse duration is decreased from 10 μs (0.1 of the pulse repetition period) to 0.5 μs (0.005 of this period).

Thus, the results of our investigation show that a nonlinear spin wave interferometer based on the YIG film is capable of effectively suppressing microwave pulses with a duration of above 1 μs and a power on the order of ten milliwatts while transmitting pulses with the power of a few milliwatts. Therefore, devices of this type can be used, for example, in the entrance circuits of receivers for suppressing strong burst noise.

Acknowledgments. This study was supported in parts by the Russian Foundation for Basic Research (project nos. 02-02-16485 and 02-02-06771), the INTAS Foundation (grant no. 99-1812), and the Ministry of Education of the Russian Federation (project no. 304.14.52).

REFERENCES

1. A. S. Semenov, V. L. Smirnov, and A. V. Shmal'ko, *Integrated Optics for Data Transmitting and Processing Systems* (Radio i Svyaz', Moscow, 1990).
2. G. P. Agrawal, *Nonlinear Fiber Optics* (Academic, San Diego, 1995).
3. Y. K. Fetisov and C. E. Patton, IEEE Trans. Magn. **35**, 1024 (1999).
4. A. B. Ustinov and B. A. Kalinikos, Pis'ma Zh. Tekh. Fiz. **27** (10), 20 (2001) [Tech. Phys. Lett. **27**, 403 (2001)].

Translated by P. Pozdeev

Technical Physics Letters, Vol. 29, No. 7, 2003, pp. 606–609. Translated from Pis'ma v Zhurnal Tekhnicheskoĭ Fiziki, Vol. 29, No. 14, 2003, pp. 74–80.

On the Prospects of Developing High-Efficiency Piezocomposites Based on Crystals of Solid Solutions of Ferroelectric Relaxors

V. Yu. Topolov* and S. V. Glushanin

Rostov State University, Rostov-on-Don, Russia

** e-mail: topolov@phys.rsu.ru*

Received February 21, 2003

Abstract—Electromechanical properties of the 0–0–2–2 type composite based on platelike crystals of solid solutions of ferroelectric relaxors of the $Pb(A_{1/3}Nb_{2/3})O_3$–$PbTiO_3$ system (A = Zn, Mg) have been studied for the first time. Factors accounting for the record values of some effective parameters of this composite are considered. The relationship between the components of the elastic compliance tensor of the layered structures forming the composite and the positions of maxima of the effective hydrostatic parameters is established. © *2003 MAIK "Nauka/Interperiodica".*

The crystals of solid solutions of ferroelectric relaxors of the $Pb(A_{1/3}Nb_{2/3})O_3$–$PbTiO_3$ system are next-generation piezoelectric materials [1–3] possessing unique physical properties near the morphotropic boundary [4–6]. The interest in these materials is related both to their high piezoelectric activity [4, 5, 7] and to the variety of domain (twinned) structures [5, 7, 8], the existence of intermediate ferroelectric phases [3, 9], and some features of the domain orientation processes and coexisting phases [9–11]. By now, the complete sets of elastic compliances, piezoelectric coefficients, and dielectric permittivities [4, 5] have been determined for $0.955Pb(Zn_{1/3}Nb_{2/3})O_3$–$0.045PbTiO_3$ (I) and $0.67Pb(Mg_{1/3}Nb_{2/3})O_3$–$0.33PbTiO_3$ (II) polydomain crystals polarized along the [001] perovskite cell direction. However, the question as to whether such crystals can be used as components of the piezoelectric composites is still open.

The purpose of this study was to determine, within the framework of a new model of the piezoelectric composite based on crystals I and II, the concentration dependences of the effective electromechanical properties, find their maxima, and reveal the advantages of these piezoelectric composites in comparison to well-known materials.

In developing a new model of the piezoelectric composite, we took into account the platelike shape of the ferroelectric crystals [4], advantages of the layered matrix [12], and some other peculiarities of microgeometry of the system. In the proposed piezoelectric composite model possessing 0–0–2–2 connectivity in terms of the Newnham classification [13] (Fig. 1), the rods composed of the platelike (001)-oriented crystals I and II penetrate through a matrix comprising alternating layers of the polymer components, vinylidene fluoride–trifluoroethylene (VDF–TrFE, 75 : 25 mol %) (III) and elastomer (IV). The interfaces between components I–II and III–IV are parallel to the X_1OX_2 plane, and the axes of the cartesian coordinate system $X_1X_2X_3$ are parallel to the vectors of translation of the perovs-

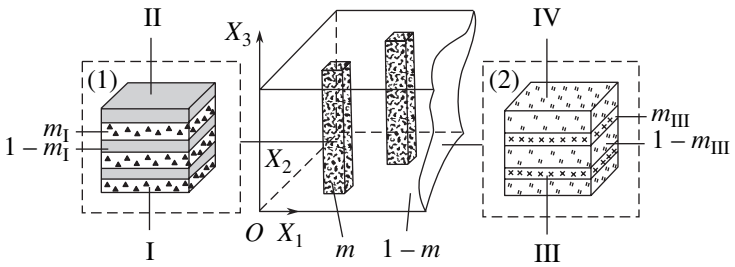

Fig. 1. A schematic diagram showing the structure of a piezoelectric composite of the 0–0–2–2 type based on $Pb(A_{1/3}Nb_{2/3})O_3$–$PbTiO_3$ crystals (I, II) in a layered III–IV matrix (m is a volume fraction of the 2–2 I–II rods surrounded by the 2–2 III–IV matrix, $1 - m$ is the "pore" volume fraction). The insets (1) and (2) show elements of the rod and matrix structures, with m_I and m_{III} being the volume fractions of component I ion the rod and component III in the matrix, respectively.

1063-7850/03/2907-0606$24.00 © 2003 MAIK "Nauka/Interperiodica"

kite cells of crystals I and II: $\mathbf{a}^{(I)} \Uparrow \mathbf{a}^{(II)} \parallel OX_1$, $\mathbf{b}^{(I)} \Uparrow \mathbf{b}^{(II)} \parallel OX_2$, and $\mathbf{c}^{(I)} \Uparrow \mathbf{c}^{(II)} \parallel OX_3$. The rods have square cross sections and their side faces are parallel to the X_1OX_3 and X_2OX_3 planes. According to these characteristics and experimental data [4, 5, 14, 15] on the room-temperature electromechanical properties of components, I–II–III–IV piezoelectric composites can be described within the framework of the point symmetry group *mm*2.

Averaging of the electromechanical parameters of components I–IV is based on a modified matrix method [16, 17] and is performed in three steps. In the first step, the elastic compliances $s_{ab}^{(n),E}$, piezoelectric coefficients $d_{ij}^{(n)}$, and dielectric permittivities $\varepsilon_{kk}^{(n),\sigma}$ are averaged for n = I and II with respect to the volume concentration m_I (Fig. 1) with allowance for the boundary conditions [16] for the electric and magnetic fields for x_3 = const. In the second step, an analogous averaging with respect to m_{III} is performed using the sets of electromechanical constants for n = III and IV. Finally, the obtained sets of electromechanical constants of the layered I–II rods and the III–IV matrix are averaged with respect to m. The latter procedure differs from that described previously [17] in that now we simultaneously take into account the boundary conditions for x_1 = const and x_2 = const, i.e., on the side faces of I–II rods (Fig. 1).

As a result of averaging, we obtain the concentration dependences of the effective elastic compliances $s_{ab}^{*E}(m, m_I, m_{III})$, piezoelectric coefficients $d_{ij}^{*}(m, m_I, m_{III})$, and dielectric permittivities $\varepsilon_{kk}^{*\sigma}(m, m_I, m_{III})$ of the proposed piezoelectric composite. Using these dependences, it is possible to calculate the parameters of practical importance [12–15, 17–20], such as piezoelectric coefficients $g_{33}^{*} = d_{33}^{*}/\varepsilon_{33}^{*\sigma}$, hydrostatic piezoelectric modulus $d_h^{*} = d_{33}^{*} + d_{32}^{*} + d_{31}^{*}$ and piezoelectric coefficient $g_h^{*} = d_h^{*}/\varepsilon_{33}^{*\sigma}$, squared figures of merit $(Q_{33}^{*})^2 = d_{33}^{*}g_{33}^{*}$ and $(Q_h^{*})^2 = d_h^{*}g_h^{*}$, and hydrostatic electromechanical coupling factor

$$k_h^{*} = d_h^{*}[\varepsilon_{33}^{*\sigma}(s_{11}^{*E} + 2(s_{12}^{*E} + s_{13}^{*E} + s_{23}^{*E}) + s_{22}^{*E} + s_{33}^{*E})]^{-1/2}. \quad (1)$$

An important feature of the proposed piezoelectric composite is the nonmonotonic character of the concentration dependences of the effective parameters of piezoelectric sensitivity (g_{33}^{*}), hydrostatic piezoelectric activity (d_h^{*}), hydrostatic piezoelectric sensitivity (g_h^{*}, $(Q_h^{*})^2$), and the electromechanical conversion efficiency k_h^{*} determined by formula (1).

Figure 2 gives examples of the surfaces of local maxima $(X^*)_m = \max X^*(m, m_I, m_{III})$ of the above parameters determined for the fixed concentrations m_I and m_{III}. The proposed I–II–III–IV piezoelectric composite of the 0–0–2–2 type exhibits the following record values of the absolute maxima of the effective electromechanical parameters: $\max(d_h^{*})_m = d_h^{*}$ (0.265, 0.01, 0.35) = 829 pC/N; $\max(g_h^{*})_m = g_h^{*}$ (0.008, 0.05, 0.25) = 805 mV m/N; $\max(Q_h^{*})_m^2 = (Q_h^{*})^2$(0.039, 0.03, 0.35) = 156×10^{-12} Pa^{-1}; and $\max(k_h^{*})_m = k_h^{*}$ (0.069, 0.03, 0.51) = 0.534. Note that $\max(d_h^{*})_m$ (Fig. 2a) exceeds the experimental values of $\max d_h^{*}$ for the 1–3 type ferroelectric piezoceramic composites (FEPCs) PZT-5A–epoxy resin type [19] and Pb(Zr,Ti)O_3–III [14] by a factor of approximately 7.5 and 5.9, respectively. The value of $\max(g_h^{*})_m$ (Fig. 2b) exceeds the experimental values of $\max g_h^{*}$ calculated for the 1–3 type FEPC PZT-5A–IV [18] and the 2–2 type FEPC Pb(Zr,Ti)O_3–polymer [20] by a factor of approximately 5 and 2.5, respectively. The value of $\max(Q_h^{*})_m^2$ (Fig. 2c) is more than three times that of $\max(Q_h^{*})^2$ calculated for the 1–2–2 type FEPC PKR-7M–IV–araldite [12]. And $\max(k_h^{*})_m$ (Fig. 2d) is about 1.4 times the value calculated for $\max k_h^{*}$ of the 1–0–1 type FEPC PKR-7M–porous araldite [17].

The reasons for such large values of $\max(X^*)_m$ are related both to the high piezoelectric activity of components of the I–II rods and to the layered structure of the III–IV matrix possessing a low piezoelectric activity. In the vicinity of $\max(d_h^{*})_m$ (Fig. 2a), the elastic compliances of I–II rods and III–IV matrix obey the relation $s_{11}^{(I–II),E}/s_{33}^{(I–II),E} = s_{11}^{(III–IV),E}/s_{33}^{(III–IV),E}$, while $\max(s_{13}^{(III–IV),E}/s_{33}^{(III–IV),E})$ and $\min(s_{11}^{(III–IV),E}/s_{33}^{(III–IV),E})$ take place at almost the same volume fraction m_{III} = 0.35. The hydrostatic piezoelectric coefficient $g_h^{(I–II)}$ at m_I = 0.05 is small as compared to the piezoelectric coefficient $g_{33}^{(I–II)}$ because of the small anisotropy of the piezoelectric moduli: $g_h^{(I–II)}$ = 2.23 mV m/N versus $g_{33}^{(I–II)}$ = 39.5 mV m/N for $d_{33}^{(I–II)} + d_{32}^{(I–II)} + d_{31}^{(I–II)} \ll d_{33}^{(I–II)}$. In I–II–III–IV piezoelectric composites, the value of $\max(g_h^{*})_m$ (Fig. 2b, surface *2*) exceeds $g_h^{(I–II)}$ by a factor of about 360 because $m \ll 1$ and $\varepsilon_{33}^{*\sigma} \ll \varepsilon_{33}^{(I–II),\sigma}$. At the same time, the maximum value of $(g_{33}^{*})_m$ corresponding to m_I = 0.03 and m_{III} = 0 (Fig. 2b,

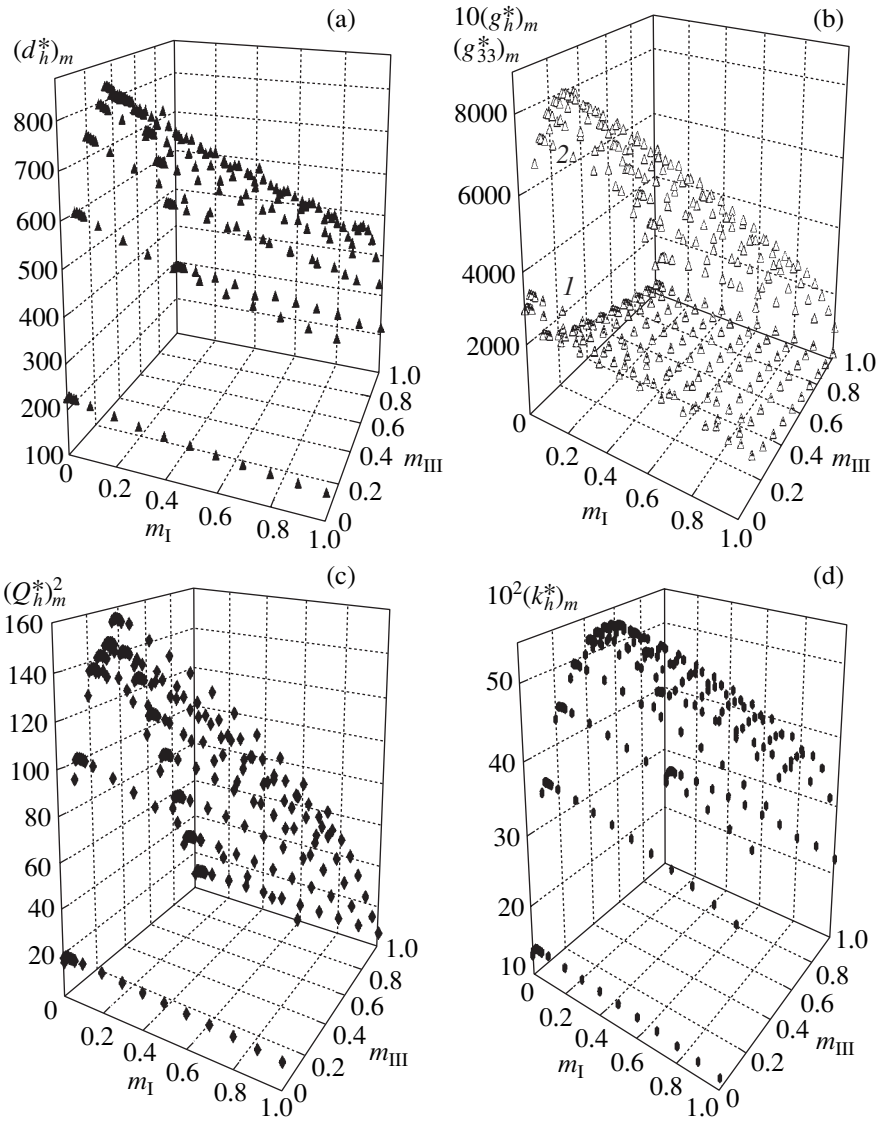

Fig. 2. Calculated concentration dependences of the local maxima of the effective electromechanical parameters of I–II–III–IV piezoelectric composites of the 0–0–2–2 type: (a) $(d_h^*)_m$ [pC/N]; (b) $(g_{33}^*)_m$ (surface *1*) and $10(g_h^*)_m$ (surface *2*) [mV m/N]; (c) $(Q_h^*)_m^2$ [Pa^{-1}]; (d) $10^2(k_h^*)_m$.

surface *1*) is 77 times that of $g_{33}^{(I–II)}$. Apparently, such large differences between $\max(g_h^*)_m$ and $\max(g_{33}^*)_m$ reflect the influence of the layered structure of the III–IV matrix on the piezoelectric sensitivity of the composite.

It is important to note that the anisotropy factor $s_{11}^{(III–IV),E}/s_{13}^{(III–IV),E}$ reaches maximum values –2.14 and –2.16 at the aforementioned bulk fractions of m_{III} = 0.25 and 0.35, respectively. This fact indicates that the elastic properties of the layered matrix play an important role in redistribution of the internal electric and mechanical fields accounting for the appearance of $\max(d_h^*)_m$, $\max(g_h^*)_m$, and $\max(Q_h^*)_m^2$. The hydrostatic electromechanical coupling factor of the I–II rods, $k_h^{(I–II)}$ = 0.163–0.166 (for $0 \le m_{III} < 0.05$), increases in the 0–0–2–2 type piezoelectric composites according to formula (1) at the expense of decreasing $\varepsilon_{33}^{*\sigma}$ (for $m < 0.1$) and changing anisotropy of the elastic compliances $s_{ab}^{(III–IV),E}$ of the III–IV matrix. The latter quantities vary so that the sum $2(s_{11}^{(III–IV),E} + s_{12}^{(III–IV),E} + 2s_{13}^{(III–IV),E}) + s_{33}^{(III–IV),E}$, which is analogous to the sum $s_{11}^{*E} + \ldots + s_{33}^{*E}$ in formula (1), approaches zero for

$m_{III} = 0.51$. This fact eventually determines the position of $\max(k_h^*)_m$ (Fig. 2d).

The results obtained within the framework of the above model of the 0–0–2–2 type piezoelectric composite show a large potential of platelike (001)-oriented crystals of ferroelectric relaxors of the $Pb(A_{1/3}Nb_{2/3})O_3$–$PbTiO_3$ system, on the one hand, and the layered structures (especially, of the III–IV type) on the other hand. The relationship established between the components of the elastic compliance tensor and the positions of maxima of the effective hydrostatic parameters has to be taken into account in the search for high-efficiency piezoelectric composites.

Acknowledgments. The authors are grateful to A.V. Turik for his interest in the subject under investigation.

This study was partly supported within the framework of the Scientific Research Program of Rostov State University (project no. 11.01.03f).

REFERENCES

1. Y. Guo, H. Luo, K. Chen, *et al.*, J. Appl. Phys. **92**, 6134 (2002).
2. H. Fu and R. Cohen, Nature (London) **403** (6767), 281 (2000).
3. B. Noheda, D. E. Cox, G. Shirane, *et al.*, Phys. Rev. Lett. **86**, 3891 (2001).
4. R. Zhang, B. Jiang, and W. Cao, J. Appl. Phys. **90**, 3471 (2001).
5. J. Jin and W. Cao, J. Appl. Phys. **92**, 444 (2002).
6. S.-F. Liu, S.-E. Park, L. E. Cross, *et al.*, J. Appl. Phys. **92**, 461 (2002).
7. S.-E. Park and T. R. Shrout, J. Appl. Phys. **82**, 1804 (1997).
8. V. Yu. Topolov, Phys. Rev. B **65**, 094207 (2002).
9. Z.-G. Ye, B. Noheda, M. Dong, *et al.*, Phys. Rev. B **64**, 184114 (2001).
10. M. K. Durbin, J. C. Hicks, S.-E. Park, *et al.*, J. Appl. Phys. **87**, 8159 (2000).
11. V. Yu. Topolov and A. V. Turik, Fiz. Tverd. Tela (St. Petersburg) **44**, 1295 (2002) [Phys. Solid State **44**, 1355 (2002)].
12. V. Yu. Topolov and A. V. Turik, Pis'ma Zh. Tekh. Fiz. **27** (2), 84 (2001) [Tech. Phys. Lett. **27**, 81 (2001)].
13. R. E. Newnham, MRS Bull. **22** (5), 20 (1997).
14. H. Taunaumang, I. L. Guy, and H. L. W. Chan, J. Appl. Phys. **76**, 484 (1994).
15. V. Yu. Topolov and A. V. Turik, Zh. Tekh. Fiz. **71** (9), 26 (2001) [Tech. Phys. **46**, 1093 (2001)].
16. E. Akcakaya and G. W. Farnell, J. Appl. Phys. **64**, 4469 (1988).
17. S. V. Glushanin and V. Yu. Topolov, J. Phys. D **34**, 2518 (2001).
18. A. A. Grekov, S. O. Kramarov, and A. A. Kuprienko, Mekh. Kompoz. Mater., No. 1, 62 (1989).
19. H. L. W. Chan and J. Unsworth, IEEE Trans. Ultrason. Ferroelectr. Freq. Control **36**, 434 (1989).
20. A. A. Grekov, S. O. Kramarov, and A. A. Kuprienko, Ferroelectrics **76** (1–4), 43 (1987).

Translated by P. Pozdeev

Technical Physics Letters, Vol. 29, No. 7, 2003, pp. 610–612. Translated from Pis'ma v Zhurnal Tekhnicheskoĭ Fiziki, Vol. 29, No. 14, 2003, pp. 81–86.

Anomalous Magnetic Hysteresis in $La_{0.6}Sr_{0.2}Mn_{1.2}O_{3-\delta}$ Manganites with a Perovskite Structure

V. T. Dovgii, A. I. Linnik*, V. P. Pashchenko, V. N. Derkachenko, V. K. Prokopenko, V. A. Turchenko, and N. V. Davydeiko**

Donetsk Physicotechnical Institute, National Academy of Sciences of Ukraine, Donetsk, Ukraine

*e-mail: * linnik@host.dipt.donetsk.ua;*

*** pashchen@pashchen.fti.ac.donetsk.ua*

Received January 14, 2003

Abstract—We have observed an anomalous magnetic hysteresis in polycrystalline (ceramic) and single crystal (film) samples of $La_{0.6}Sr_{0.2}Mn_{1.2}O_{3-\delta}$ manganites with a perovskite structure. The anomaly is explained by the coexistence and interaction of two magnetic phases (ferromagnetic and antiferromagnetic) in these lanthanum-containing manganites. © *2003 MAIK "Nauka/Interperiodica".*

Introduction. Perovskitelike rare-earth manganites of the $R_{1-x}M_xMnO_3$ type (R = La^{3+}, Pr^{3+}, Nd^{3+}, etc.; M = Sr^{2+}, Ca^{2+}, Ba^{2+}) have been extensively studied in recent years. This interest is related to the phenomenon of colossal magnetoresistance observed in these systems. The research is aimed at explaining the nature of this phenomenon and assessing the possibility of its practical application [1–4].

Explanations of the colossal magnetoresistance effect are based on various mechanisms, including the double Zener exchange and the dynamic Jahn–Teller effect [5, 6], and the notions about the state featuring two magnetic phases typical of magnetic semiconductors [3].

Here we report on the results of investigation of the magnetic state of $La_{0.6}Sr_{0.2}Mn_{1.2}O_{3-\delta}$ manganites, aimed at assessing the possibility of coexistence of various magnetic phases [7–12] and phase separation with the formation of clusters [13, 14].

Methods of sample preparation and investigation. Manganites are complex metal oxides exhibiting a unique combination and interplay of electronic, magnetic, and structural properties controlled by the chemical composition and preparation technology.

The base composition represented a nonstoichiometric lanthanum strontium manganite $La_{0.6}Sr_{0.2}Mn_{1.2}O_{3-\delta}$ with a perovskite structure, possessing a high Curie temperature (T_C > 300 K). A special feature of our samples was an increased content of manganese whose ions determine the magnetic and transport properties of manganites [13, 14].

Polycrystalline samples were prepared using a standard ceramic technology using a mixture of La_2O_3, $SrCO_3$, and Mn_3O_4 powders (all of analytical purity grade). The synthesis was performed by annealing at 900°C for 20 h, after which the pressed pellets were sintered at 1150°C for 21 h. Single crystal film samples were prepared by means of laser deposition at 730°C (without additional annealing) onto (100)-oriented $LaSrGaO_4$ single crystal substrate.

The magnetic properties were studied using a vibrating sample magnetometer and a setup for inductance–frequency measurements. The electric conductivity was determined by the conventional four-point-probe technique. The X-ray diffraction measurements were performed on a DRON-2 diffractometer.

Experimental results and discussion. According to the X-ray diffraction data, the ceramic samples contained a perovskitelike rhomohedrally distorted ($R\bar{3}c$) phase with the lattice parameters a = 0.3893 nm, α = 90.44° and a small amount of γ- Mn_2O_3. The single crystal film possessed a nearly cubic structure with the lattice parameter a = 0.3845 nm.

The results of the magnetization measurements on a vibrating sample magnetometer showed that the samples are typical magnetically soft ferromagnets exhibiting saturation in a magnetic field of $H \approx 320$ kA/m. The specific saturation magnetization of the ceramic samples measured in a magnetic field of 540 kA/m at a temperature of 77 and 290 K was 85 and 53 A m^2/kg, respectively, and the Curie temperature was T_C = 348 K. For the single crystal film, the saturation magnetization was 16 kA/m.

The temperature dependence of the electric resistance of a ceramic sample exhibited a maximum at T_{ms} = 348 K related to the semiconductor–metal transition in the region of T_C. The magnetoresistance $\Delta R/R_0 = R_0 - R_H/R_0$ of the ceramic sample was 4.5–5% (R_0 and

R_H are the sample resistance measured in the magnetic fields H = 0 and 400 kA/m, respectively). The maximum magnetoresistance in a field of H = 400 kA/m was observed 14 K below the Curie temperature. For the single crystal film, the magnetoresistance amounted to 6–6.5% and the magnetoresistance peak was observed at T_p = 255 K. The temperature dependence of the electric resistance of the film exhibited a maximum at T_{ms} = 285 K. Thus, the semiconductor–metal transition temperature in the ceramic is 63 K higher than that in the film. This discrepancy in T_{ms} values of the ceramic and film is explained by their different nonstoichiometry with respect to oxygen [15]: the oxygen content is higher in slowly cooled ceramics than in the single crystal film (not subjected to additional low-temperature annealing).

The results of inductance–frequency measurements [16], previously employed for studying the magnetic properties of garnet ferrite films, revealed anomalies on the magnetization curves of the manganite samples studied. The measurements were performed on samples placed into a coil of the measuring oscillator with a natural frequency of f = 5 MHz. Application of the external magnetic field changes the magnetic state of a ceramic or film sample and, hence, modifies the inductance of the measuring coil and the resonance frequency of the oscillator circuit.

Figures 1 and 2 present the plots of a change in the resonance frequency (Δf) of the coil with a ceramic or film sample versus the strength of an external quasistatic magnetic field applied perpendicularly ($H_\perp$) or parallel ($H_\parallel$) to the sample plane; arrows indicate the direction of variation of the magnetic field strength. The measurements were performed at room temperature (T = 290 K). Since the resonance frequency shift is proportional to the sample magnetization ($\Delta f \propto \Delta M$) or a change in the energy of a magnet in the applied magnetic field, the shape of the function $\Delta f = f(H)$ is equivalent to the behavior of the magnetization $M = f(H)$.

As can be seen in Fig. 1, the upper parts of the Δf curves of the ceramic sample exhibit a "normal" hysteresis characteristic of a magnetically soft material, whereby the magnetization branch lies below the demagnetization branch. The lower (low-field) parts of the Δf curves reveal an "anomalous" hysteresis behavior: the demagnetization branch occurs above the magnetization branch, so that the minimum energy of the magnet is attained in a field of the same sign.

Figure 2, which shows analogous curves for a single crystal film of $La_{0.6}Sr_{0.2}Mn_{1.2}O_3$ manganite, reveals a significant difference in behavior of the sample magnetization in the external field oriented parallel and perpendicularly to the film plane. When the applied field is parallel to the sample surface ($H_\parallel$), the material is saturated in a relatively small field and exhibits no hysteresis. In the magnetic field perpendicular to the sample surface ($H_\perp$), the sample magnetization is almost

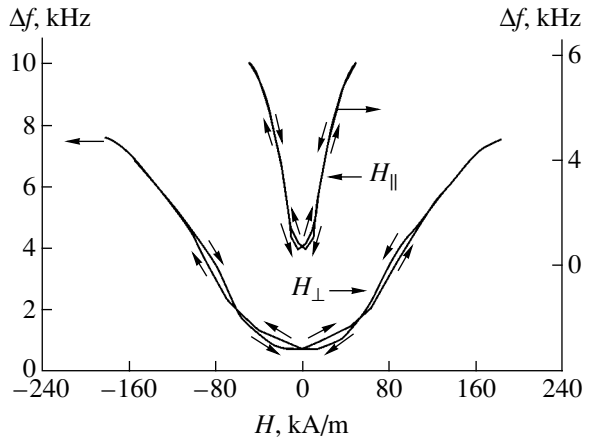

Fig. 1. Plots of a change in the resonance frequency of the measuring circuit ($\Delta f \propto \Delta M$) versus magnetic field strength H for a sample of $La_{0.6}Sr_{0.2}Mn_{1.2}O_3$ manganite ceramics magnetized in the field parallel ($H_\parallel$) and perpendicular ($H_\perp$) to the sample plane.

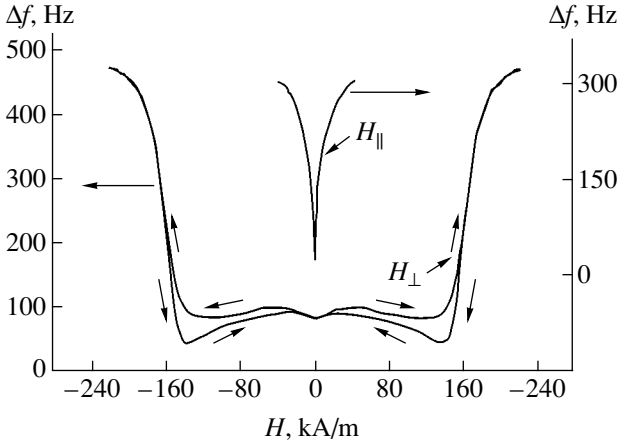

Fig. 2. Plots of a change in the resonance frequency of the measuring circuit ($\Delta f \propto \Delta M$) versus magnetic field strength H for a sample of $La_{0.6}Sr_{0.2}Mn_{1.2}O_3$ manganite single crystal film magnetized in the field parallel ($H_\parallel$) and perpendicular ($H_\perp$) to the film plane.

unchanged up to a field strength of about 144 kA/m, after which the film is rapidly magnetized to saturation. As can be seen from Fig. 2, the film sample magnetized and demagnetized at room temperature (T = 290 K) exhibits virtually no normal hysteresis component and shows only the anomalous behavior, whereby the magnetization branch passes below the demagnetization branch and the minimum energy of the magnet is attained in a field of the same sign.

An analysis of the experimental data suggests that the manganite samples may contain magnetic inhomogeneities behaving as magnetic phases with different magnetization directions, which can be responsible for the normal and anomalous hysteresis. A possible mechanism explaining this behavior is the interaction

(exchange anisotropy) between the ferromagnetic and antiferromagnetic phases. The exchange anisotropy in a boundary region between the two phases leads to a shift of the hysteresis loop during the low-temperature magnetization of such materials [9, 17].

The aforementioned interaction accounts for the anomalous hysteresis and explains the results of room-temperature observations. It should be noted that the anomalous hysteresis was maximal in the samples magnetized to saturation. Some samples of different compositions, as well as in the ceramic samples of the same composition synthesized at 900°C but not annealed at 1150°C, exhibited only the normal hysteresis, which is probably explained by the lack of ordering in the antiferromagnetic phase. The antiferromagnetic phase can be represented by clusters in ferromagnetic grains and/or grain boundaries. In addition, it should be mentioned that the film samples of manganites may contain magnetoelectrically "dead" layers [18] and may possess a block structure [19].

Conclusions. We have discovered an anomalous magnetic hysteresis in the initial parts of the magnetization curves of ceramic and film samples of nonstoichiometric $La_{0.6}Sr_{0.2}Mn_{1.2}O_{3-\delta}$ manganites. This anomalous behavior is explained by a mechanism related to the coexistence and interaction of ferromagnetic and antiferromagnetic phases and/or clusters. The effect probably represents a manifestation of different magnetic susceptibilities of the ferromagnetic and "tilted" magnetic phases under the action of an external magnetic field.

REFERENCES

1. S. Jin, T. H. Tiefel, M. Mc Cormack, *et al.*, Science **264**, 413 (1994).
2. A. Yrushibara, Y. Moritomo, T. Arima, *et al.*, Phys. Rev. B **51**, 14103 (1995).
3. É. L. Nagaev, Usp. Fiz. Nauk **166**, 833 (1996) [Phys. Usp. **39**, 781 (1996)].
4. A. P. Ramires, J. Phys.: Condens. Matter **9**, 8171 (1997).
5. A. J. Millis, P. B. Littlewood, and B. I. Shraiman, Phys. Rev. Lett. **74**, 5144 (1995).
6. A. J. Millis, B. I. Shraiman, and R. Mueller, Phys. Rev. Lett. **77**, 175 (1996).
7. L. I. Koroleva, R. V. Demin, and A. M. Balbashov, Pis'ma Zh. Éksp. Teor. Fiz. **65**, 449 (1997) [JETP Lett. **65**, 474 (1997)].
8. O. Yu. Gorbenko, R. V. Demin, A. R. Kaul', *et al.*, Fiz. Tverd. Tela (St. Petersburg) **40**, 290 (1998) [Phys. Solid State **40**, 263 (1998)].
9. R. V. Demin, L. I. Koroleva, R. Shimchak, *et al.*, Pis'ma Zh. Éksp. Teor. Fiz. **75**, 402 (2002) [JETP Lett. **75**, 331 (2002)].
10. K. N. Mikhalev, S. A. Lekomtsev, A. P. Gerashchenko, *et al.*, Pis'ma Zh. Éksp. Teor. Fiz. **72**, 867 (2000) [JETP Lett. **72**, 599 (2000)].
11. K. N. Mikhalev, S. A. Lekomtsev, A. P. Gerashchenko, *et al.*, Fiz. Met. Metalloved. **93** (4), 32 (2002).
12. T. I. Arbuzova, I. B. Smolyak, S. V. Naumov, *et al.*, Zh. Éksp. Teor. Fiz. **116**, 1664 (1999) [JETP **89**, 899 (1999)].
13. V. P. Pashchenko, S. I. Khartsev, O. P. Cherenkov, *et al.*, Neorg. Mater. **35**, 1509 (1999).
14. V. P. Pashchenko, V. K. Prokopenko, A. A. Shemyakov, *et al.*, Metallofiz. Noveishie Tekhnol. **22** (12), 18 (2000).
15. V. P. Pashchenko, S. S. Kucherenko, P. I. Polyakov, *et al.*, Low Temp. Phys. **27**, 1010 (2001).
16. J. Maartense, J. Appl. Phys. **53**, 2466 (1982).
17. W. H. Meiklejohn and C. P. Bean, Phys. Rev. **105**, 904 (1957).
18. R. P. Borges, W. Guichard, J. G. Lunney, *et al.*, J. Appl. Phys. **89**, 3868 (2001).
19. Yu. A. Boĭkov, T. Klaeson, and A. Yu. Boĭkov, Zh. Tekh. Fiz. **71** (10), 54 (2001) [Tech. Phys. **46**, 1260 (2001)].

Translated by P. Pozdeev

Technical Physics Letters, Vol. 29, No. 7, 2003, pp. 613–616. Translated from Pis'ma v Zhurnal Tekhnicheskoĭ Fiziki, Vol. 29, No. 14, 2003, pp. 87–94.

Formulation of the Boundary Conditions on Curvilinear Surfaces Streamlined by a Rarefied Gas

V. N. Popov

Pomorskiĭ State University, Arkhangelsk, Russia

e-mail: popov.vasily@pomorsu.ru

Received March 17, 2003

Abstract—The necessity of taking into account the Barnett correction to the gas distribution function in the boundary conditions on curvilinear surfaces streamlined by a rarefied gas is demonstrated for a solid sphere.

The construction of exact analytical solutions of inhomogeneous model equations in boundary-value problems of the kinetic theory of rarefied gases, related to the description of curvilinear surfaces streamlined by a rarefied gas flow with inhomogeneous temperature and mass flow velocity distributions, was considered in [1–8]. Using exact analytical methods, these investigations refined the values of some coefficients previously obtained within the framework of approximate methods [9–11]. At the same time, the question as to how the solutions obtained in [1–8] can be related to the original results of Sone and Aoki [12, 13] is still open. Below we will analyze this problem in some detail.

Consider a solid spherical surface streamlined by a steady flow of a rarefied gas. Let a boundary condition on the surface correspond to the model of diffuse reflection. Introduce a spherical coordinate system with the origin coinciding with a particle center and the polar axis directed along the mass velocity vector at a point far from the solid surface. In this coordinate system, the Boltzmann kinetic equation with a linearized collision operator in the form of the Bhatnagar–Gross–Kruck (BGK) model can be written as follows:

$$C_r\frac{\partial f}{\partial r}+\frac{1}{r}\Big[C_\theta\frac{\partial f}{\partial\theta}+\frac{C_\varphi}{\sin\theta}\frac{\partial f}{\partial\varphi}+(C_\theta^2+C_\varphi^2)\frac{\partial f}{\partial C_r}$$
$$+(C_\varphi^2\cot\theta-C_rC_\theta)\frac{\partial f}{\partial C_\theta}-(C_\varphi C_\theta\cot\theta+C_rC_\varphi)\frac{\partial f}{\partial C_\varphi}\Big]$$
$$=k^{-1}[f^0(\mathbf{r},\mathbf{C})\iiint K(\mathbf{C},\mathbf{C}')f(\mathbf{r},\mathbf{C}')d\mathbf{C}'-f(\mathbf{r},\mathbf{C})].$$

Here, $\beta^{-1/2}\mathbf{C}$ is the dimensional velocity of gas molecules; $L\mathbf{r}$ is the dimensional radius vector; L is a characteristic size of the streamlined body (for a sphere L coincides with the radius); $f^0(\mathbf{r},\mathbf{C})=(\beta/\pi)^{3/2}\exp(-C^2)$ is the absolute Maxwellian, $\beta=m/2k_BT_0$; k_B is the Boltzmann constant; m is the molecular mass of the gas; $k=2\pi^{-1/2}\mathrm{Kn}$; $\mathrm{Kn}=l/L$ is the Knudsen number; l is the mean free path of the gas molecules; $\nu=l(2kT/\pi m)^{1/2}$ is the kinematic gas viscosity; and $f(\mathbf{r},\mathbf{C})$ is the distribution function of the gas molecules with respect to coordinates and velocities, and

$$K(\mathbf{C},\mathbf{C}')=1+2\mathbf{C}\mathbf{C}'+\frac{2}{3}\Big(C^2-\frac{3}{2}\Big)\Big(C'^2-\frac{3}{2}\Big).$$

Assuming that the deviation of the state of the rarefied gas from equilibrium is small, let us linearize $f(\mathbf{r},\mathbf{C})$ relative to the absolute Maxwellian:

$$f(\mathbf{r},\mathbf{C})=f^0(\mathbf{r},\mathbf{C})[1+\Psi(\mathbf{r},\mathbf{C})].$$

Here, the function $\Psi(\mathbf{r},\mathbf{C})$ obeys the equation

$$C_r\frac{\partial\Psi}{\partial r}+\frac{1}{r}\Big[C_\theta\frac{\partial\Psi}{\partial\theta}+\frac{C_\varphi}{\sin\theta}\frac{\partial\Psi}{\partial\varphi}+(C_\theta^2+C_\varphi^2)\frac{\partial\Psi}{\partial C_r}$$
$$+(C_\varphi^2\cot\theta-C_rC_\theta)\frac{\partial\Psi}{\partial C_\theta}-(C_\varphi C_\theta\cot\theta+C_rC_\varphi)\frac{\partial\Psi}{\partial C_\varphi}\Big] \quad (1)$$
$$=k^{-1}[\pi^{-3/2}\iiint\exp(-C'^2)K(\mathbf{C},\mathbf{C}')\Psi(\mathbf{r},\mathbf{C}')d\mathbf{C}'-\Psi(\mathbf{r},\mathbf{C})].$$

Taking into account that the ratio of the right-hand part of Eq. (1) to the left-hand part of this equation is on the order of Kn^{-1}, a solution for the gas bulk can be constructed by the iterative method. Presenting $\Psi(\mathbf{r},\mathbf{C})$ in the form

$$\Psi(\mathbf{r},\mathbf{C})=1+2C_rU_r^{(0)}+2C_\theta U_\theta^{(0)}$$
$$+\Big(C^2-\frac{5}{2}\Big)\tau^{(0)}+k\psi_{Ch}(\mathbf{r},\mathbf{C})+k^2\psi_B(\mathbf{r},\mathbf{C})+\ldots, \quad (2)$$

substituting this expression into Eq. (1), and equating the coefficients at the same powers of k, we obtain the

following relations:

$$\psi_{Ch}(\mathbf{r}, \mathbf{C}) = p^{(1)} + 2C_r U_r^{(1)} + 2C_\theta U_\theta^{(1)} - 2C_r^2 \frac{\partial U_r^{(0)}}{\partial r}$$
$$- \frac{2C_\theta^2}{r}\frac{\partial U_\theta^{(0)}}{\partial \theta} - 2C_r C_\theta S_{r\theta}^{(0)} - \frac{2}{r}(C_\theta^2 + C_\varphi^2)U_r^{(0)} - \frac{2C_\varphi^2 \cot\theta}{r}U_\theta^{(0)}$$
$$+ \left(C^2 - \frac{5}{2}\right)\left[\tau^{(1)} - C_r\frac{\partial \tau^{(0)}}{\partial r} - \frac{C_\theta}{r}\frac{\partial \tau^{(0)}}{\partial \theta}\right], \quad (3)$$

$$\psi_B(\mathbf{r}, \mathbf{C}) = p^{(2)} + 2C_r U_r^{(2)} + 2C_\theta U_\theta^{(2)} - C_r\frac{\partial p^{(1)}}{\partial r}$$
$$- 2C_r^2\frac{\partial U_r^{(1)}}{\partial r} - 2C_r C_\theta\frac{\partial U_\theta^{(1)}}{\partial r} + 2C_r^3\frac{\partial^2 U_r^{(0)}}{\partial r^2} + \frac{2C_r C_\theta^2}{r}\frac{\partial^2 U_\theta^{(0)}}{\partial r \partial \theta}$$
$$+ 2C_r^2 C_\theta\frac{\partial S_{r\theta}^{(0)}}{\partial r} + \frac{6C_r}{r}(C_\theta^2 + C_\varphi^2)\frac{\partial U_r^{(0)}}{\partial r} - \frac{2C_r}{r^2}(C_\theta^2 + C_\varphi^2)U_r^{(0)}$$
$$- \frac{C_\theta}{r}\frac{\partial p^{(1)}}{\partial \theta} + \frac{2C_r C_\varphi^2 \cot\theta}{r}\left(\frac{\partial U_\theta^{(0)}}{\partial r} - \frac{U_\theta^{(0)}}{r}\right)$$
$$- \frac{2C_r C_\theta}{r}\frac{\partial U_r^{(1)}}{\partial \theta} + \frac{2C_\theta}{r^2}(C_\theta^2 + C_\varphi^2)\frac{\partial U_r^{(0)}}{\partial \theta}$$
$$- \frac{2C_\theta^2}{r}\frac{\partial U_\theta^{(1)}}{\partial \theta} + \frac{2C_r^2 C_\theta}{r}\frac{\partial^2 U_r^{(0)}}{\partial r \partial \theta} + \frac{2C_\theta^3}{r^2}\frac{\partial^2 U_\theta^{(0)}}{\partial \theta^2}$$
$$+ \frac{2C_r C_\theta^2}{r}\frac{\partial S_{r\theta}^{(0)}}{\partial \theta} + \frac{6C_\theta}{r^2}(C_\varphi^2 \cot\theta - C_r C_\theta)\frac{\partial U_\theta^{(0)}}{\partial \theta} \quad (4)$$
$$- \frac{2}{r}\left[(C_\theta^2 + C_\varphi^2)[U_r^{(1)} - C_\theta S_{r\theta}^{(0)}] + (C_\varphi^2 \cot\theta - C_r C_\theta)\right.$$
$$\times\left[U_\theta^{(1)} - C_r S_{r\theta}^{(0)} - \frac{2C_\theta}{r}U_r^{(0)}\right] + \frac{2C_\varphi}{r}(C_\varphi C_\theta \cot\theta + C_r C_\varphi)$$
$$\left.\times[U_r^{(0)} + U_\theta^{(0)}\cot\theta]\right] - \left(C^2 - \frac{5}{2}\right)\left[C_r\frac{\partial \tau^{(1)}}{\partial r} + \frac{C_\theta}{r}\frac{\partial \tau^{(1)}}{\partial \theta}\right.$$
$$- C_r^2\frac{\partial^2 \tau^{(0)}}{\partial r^2} - 2C_r C_\theta\frac{\partial^2 \tau^{(0)}}{\partial r \partial \theta} - \frac{C_\theta^2}{r^2}\frac{\partial^2 \tau^{(0)}}{\partial \theta^2}$$
$$\left. + \frac{2C_r C_\theta}{r^2}\frac{\partial \tau^{(0)}}{\partial \theta} - \frac{1}{r}(C_\theta^2 + C_\varphi^2)\frac{\partial \tau^{(0)}}{\partial r} - \frac{C_\varphi^2 \cot\theta}{r^2}\frac{\partial \tau^{(0)}}{\partial \theta}\right].$$

Relations (2)–(4) determine a solution to Eq. (1) in the Barnett approximation:

$$S_{r\theta}^{(i)} = \frac{1}{r}\frac{\partial U_r^{(i)}}{\partial \theta} + \frac{\partial U_\theta^{(i)}}{\partial r} - \frac{U_\theta^{(i)}}{r}.$$

The obtained distribution function satisfies Eq. (1), but it does not obey the boundary condition on the spherical surface. In order to meet this condition, let us represent the distribution function as

$$f = f^0[1 + \Psi(\mathbf{r}, \mathbf{C}) + Y(\mathbf{r}, \mathbf{C})].$$

where $Y(\mathbf{r}, \mathbf{C})$ describes deviation of the distribution function in the Knudsen layer (a thin boundary layer of the gas immediately adjacent to the streamlined surface, with a thickness equal to the mean free path of the gas molecules) from the distribution function in the gas bulk. In order to determine the deviation function, let us pass to a new gage in the configuration space and introduce a dimensionless coordinate so that the dimensional radius vector is $(2/\sqrt{\pi})l\mathbf{r}$, where l is the mean free path of the gas molecules (the new dimensionless coordinate is denoted again by $\mathbf{r}$). In these notations, the inverse dimensionless radius of the sphere is $R^{-1} = 2\pi^{-1/2}\mathrm{Kn} = k$ and the function $Y(\mathbf{r}, \mathbf{C})$ obeys the equation

$$C_r\frac{\partial Y}{\partial r} + k\left[C_\theta\frac{\partial Y}{\partial \theta} + \frac{C_\varphi}{\sin\theta}\frac{\partial Y}{\partial \varphi} + (C_\theta^2 + C_\varphi^2)\frac{\partial Y}{\partial C_r}\right.$$
$$\left. + (C_\varphi^2 \cot\theta - C_r C_\theta)\frac{\partial Y}{\partial C_\theta} - (C_\varphi C_\theta \cot\theta + C_r C_\varphi)\frac{\partial Y}{\partial C_\varphi}\right]$$
$$= \pi^{-3/2}\iiint \exp(-C'^2)K(\mathbf{C}, \mathbf{C}')Y(\mathbf{r}, \mathbf{C}')d\mathbf{C}' - Y(\mathbf{r}, \mathbf{C}).$$

Expanding $Y(\mathbf{r}, \mathbf{C})$ into series with respect to k,

$$Y(\mathbf{r}, \mathbf{C}) = kY_1(\mathbf{r}, \mathbf{C}) + k^2 Y_2(\mathbf{r}, \mathbf{C}) + \ldots,$$

and taking into account the diffuse character of the gas–surface interaction, we obtain

$$Y_1(\mathbf{R}, \mathbf{C}) = -\psi_{Ch}(\mathbf{R}, \mathbf{C}), \quad Y_2(\mathbf{R}, \mathbf{C}) = -\psi_B(\mathbf{R}, \mathbf{C}),$$
$$\mu > 0.$$
$$Y_1(\infty, \mathbf{C}) = Y_2(\infty, \mathbf{C}) = 0.$$

In the sliding problems ($\mu = C_r$) [2]:

$$Y_1(\mathbf{r}, \mathbf{C}) = C_\theta(C_\theta^2 + C_\varphi^2 - 2)Z_0(r, \mu) + C_\theta Z_1(r, \mu),$$

$$Y_2(\mathbf{r}, \mathbf{C}) = C_\theta Z_2(r, \mu) + \sum_{j=0}^{\infty} g_j(C_\theta, C_\varphi)\omega_j(r, \mu),$$

where $g_j(C_\theta, C_\varphi)$ forms together with C_θ a complete set of orthogonal polynomials (in terms of the scalar product).

Using the results obtained in [2, 5], the calculation of the velocity of rarefied gas sliding on the spherical

surface can be reduced to solving the system of equations

$$\mu\frac{\partial Z_0}{\partial r} + Z_0(r,\mu) = 0,$$

$$\mu\frac{\partial Z_1}{\partial r} + Z_1(r,\mu) = \frac{1}{\sqrt{\pi}}\int_{-\infty}^{\infty} Z_1(r,\tau)\exp(-\tau^2)d\tau,$$

$$\mu\frac{\partial Z_2}{\partial r} + Z_2(r,\mu) = \frac{1}{\sqrt{\pi}}\int_{-\infty}^{\infty} Z_2(r,\tau)\exp(-\tau^2)d\tau + \mu Z_1(r,\mu) - 2\frac{\partial Z_1}{\partial\mu} + 4\mu Z_0(r,\mu) - 2\frac{\partial Z_0}{\partial\mu}$$

with the boundary conditions

$$Z_1(R,\mu) = -2U_\theta^{(1)} + 2\mu S_{r\theta}^{(0)} + \left(\mu^2 - \frac{1}{2}\right)\frac{\partial\tau^{(0)}}{\partial\theta}, \quad \mu > 0,$$

$$Z_2(R,\mu) = -2U_\theta^{(2)} + 2\mu S_{r\theta}^{(1)} + 2\left(\mu^2 - \frac{1}{2}\right)\left[S_{r\theta}^{(0)} - \frac{\partial S_{r\theta}^{(0)}}{\partial r} - \mu\frac{\partial^2\tau^{(0)}}{\partial r\partial\theta} + \mu\frac{\partial\tau^{(0)}}{\partial\theta} + \frac{1}{2}\frac{\partial\tau^{(1)}}{\partial\theta}\right], \quad \mu > 0,$$

$$Z_0(R,\mu) = 0, \quad \mu > 0;$$

$$Z_0(\infty,\mu) = Z_1(\infty,\mu) = Z_2(\infty,\mu) = 0.$$

Taking into account the results obtained in [2, 5, 6], the expressions for $U_\theta^{(1)}$ and $U_\theta^{(2)}$ are obtained from the conditions

$$\int_0^\infty \frac{X^-(\mu)}{\lambda^-(\mu)} Z_1(R,\mu)\mu\exp(-\mu^2)d\mu = 0, \tag{5}$$

$$\int_0^\infty \frac{X^-(\mu)}{\lambda^-(\mu)}\left[\left[Z_2(R,\mu) + \left[(2\mu - C_T)\left(\mu^2 - \frac{1}{2}\right) + C_n\right]\frac{\partial^2\tau^{(0)}}{\partial r\partial\theta} - 2\mu(\mu^2 + Q_2)\frac{\partial\tau^{(0)}}{\partial\theta}\right]\mu\exp(-\mu^2) - 2[\mu a(\mu)]'\right]d\mu = 0. \tag{6}$$

The last three terms in Eq. (6) were obtained in descriptions of the second-order slip [6] and the effect of the surface curvature on the thermal [2] and isothermal [5] slippage coefficients; $a(\mu)$ are the coefficients in the expansion of a solution to the problem of isothermal slip along the flat solid surface with respect to the vectors of continuous spectrum [5]; Q_n are the Loyalka integrals [14]; $C_T = 1.30272$ is the temperature jump coefficient; $C_n = -0.55844$ is the coefficient determined in the description of the temperature jump, based on the condition that the interface is impermeable for the gas molecules.

Calculating the integrals in relations (5) and (6) and accomplishing the necessary transformations, we obtain

$$\begin{aligned} U_\theta^{(1)} &= -Q_1 S_{r\theta}^{(0)} - \frac{1}{2}\left(Q_2 + \frac{1}{2}\right)\frac{\partial\tau^{(0)}}{\partial\theta} \\ &= 1.01619 S_{r\theta}^{(0)} + 0.38316\frac{\partial\tau^{(0)}}{\partial\theta}, \end{aligned}$$

$$\begin{aligned} U_\theta^{(2)} &= -Q_1 S_{r\theta}^{(1)} + \left(Q_2 + \frac{1}{2}\right)\frac{\partial S_{r\theta}^{(0)}}{\partial r} - \left(Q_2 + \frac{3}{2}\right)S_{r\theta}^{(0)} + \frac{1}{2}C_n\frac{\partial^2\tau^{(0)}}{\partial r\partial\theta} + Q_1\left(Q_2 + \frac{1}{2}\right)\frac{\partial\tau^{(0)}}{\partial\theta} \\ &= 1.01619 S_{r\theta}^{(1)} - 0.76632\frac{\partial S_{r\theta}^{(0)}}{\partial r} - 0.2337 S_{r\theta}^{(0)} - 0.27922\frac{\partial^2\tau^{(0)}}{\partial r\partial\theta} + 0.77872\frac{\partial\tau^{(0)}}{\partial\theta}, \end{aligned} \tag{7}$$

where it was taken into account that [5, 14]

$$\frac{2}{\sqrt{\pi}}\int_0^\infty \frac{X^-(\mu)}{\lambda^-(\mu)}[\mu a(\mu)]'d\mu = -2S_{r\theta}^{(0)},$$

$$Q_1 = -1.01619, \quad Q_2 = -1.26632.$$

Analogous expressions in [13] were written as follows:

$$U_\theta^{(1)} = k_0 S_{r\theta}^{(0)} + K_1\frac{\partial\tau^{(0)}}{\partial\theta},$$

$$U_\theta^{(2)} = k_0 S_{r\theta}^{(1)} + a\frac{\partial S_{r\theta}^{(0)}}{\partial r} + (b+c)S_{r\theta}^{(0)} + (e-f-g)\frac{\partial\tau^{(0)}}{\partial\theta} - e\frac{\partial^2\tau^{(0)}}{\partial r\partial\theta},$$

$$k_0 = 1.01619, \quad K_1 = 0.38316, \quad a = -0.76632, \quad b = 0.50000,$$

$$c = 0.26632, \quad e = 0.27922, \quad f = 0.26693, \quad g = -0.76644.$$

Thus, the results obtained in this study fully coincide with the analogous results of Sone and Aoki [12, 13]. If the linearization of the distribution function $f(\mathbf{r}, \mathbf{C})$ is restricted to the Chapman–Enskog approximation with

neglect of the term $\psi_B(\mathbf{r}, \mathbf{C})$ in Eq. (2) (as was done in [9–11]), the expression for $U_\theta^{(2)}$ takes the form

$$U_\theta^{(2)} = -\beta_R' \frac{\partial \tau^{(0)}}{\partial \theta} + [\beta_R - \beta_B] \frac{\partial^2 \tau^{(0)}}{\partial r \partial \theta}$$

$$= -0.5338 \frac{\partial \tau^{(0)}}{\partial \theta} - 0.7745 \frac{\partial^2 \tau^{(0)}}{\partial r \partial \theta},$$

$$\beta_R = 0.5380503, \quad \beta_R' = 0.5338,$$

$$\beta_B = 1.3126.$$

Thus, the expression for $U_\theta^{(2)}$ obtained in this approach to linearization of the distribution function significantly differs from the result obtained in [12, 13].

Conclusions. An analysis of the description of a solid spherical surface streamlined by a rarefied gas shows that the results obtained in [1–8] with allowance of the Barnett correction to the gas distribution function coincide with the results obtained in [12, 13]. All coefficients describing the influence of the surface curvature on the velocity of gas sliding, except the coefficient at the mixed second-order derivative of the temperature perturbation, are expressed through the first two Loyalka integrals.

REFERENCES

1. A. V. Latyshev, V. N. Popov, and A. A. Yushkanov, Pis'ma Zh. Tekh. Fiz. **28** (5), 70 (2002) [Tech. Phys. Lett. **28**, 204 (2002)].
2. A. V. Latyshev, V. N. Popov, and A. A. Yushkanov, Sib. Zh. Industr. Mat. **5** (3), 103 (2002).
3. A. V. Latyshev, V. N. Popov, and A. A. Yushkanov, Inzh.-Fiz. Zh. **75** (3), 104 (2002).
4. V. N. Popov, Zh. Tekh. Fiz. **72** (10), 15 (2002) [Tech. Phys. **47**, 1219 (2002)].
5. V. N. Popov, Inzh.-Fiz. Zh. **75** (3), 107 (2002).
6. V. N. Popov, Pis'ma Zh. Tekh. Fiz. **28** (19), 10 (2002) [Tech. Phys. Lett. **28**, 800 (2002)].
7. V. N. Popov, Prikl. Mekh. Tekh. Fiz., No. 5, 105 (2002).
8. V. N. Popov, Pis'ma Zh. Tekh. Fiz. **29** (3), 33 (2003) [Tech. Phys. Lett. **29**, 99 (2003)].
9. Yu. I. Yalamov, A. B. Poddoskin, and A. A. Yushkanov, Dokl. Akad. Nauk SSSR **254**, 343 (1980) [Sov. Phys. Dokl. **25**, 734 (1980)].
10. A. B. Poddoskin, A. A. Yushkanov, and Yu. I. Yalamov, Zh. Tekh. Fiz. **50** (1), 158 (1980) [Sov. Phys. Tech. Phys. **25**, 92 (1980)].
11. A. B. Poddoskin, A. A. Yushkanov, and Yu. I. Yalamov, Zh. Tekh. Fiz. **52**, 2253 (1982) [Sov. Phys. Tech. Phys. **27**, 1383 (1982)].
12. Y. Sone, *Rarefied Gas Dynamics* (Academic, New York, 1969), Vol. 1, pp. 243–253.
13. Y. Sone and K. Aoki, in *Rarefied Gas Dynamics*, Vol. 51 of *AIAA Progress in Astronautics and Aeronautics*, Ed. by J. L. Potter (American Institute of Aeronautics and Astronautics, New York, 1977), Part 1, pp. 417–433.
14. S. K. Loyalka, Transp. Theory Stat. Phys. **4**, 55 (1975).

Translated by P. Pozdeev